The Role of Acidity in Tumour Development

Kieran Smallbone

Mathematical Institute

University of Oxford

Thesis submitted for the degree

of Doctor of Philosophy

New College

Trinity Term, 2006

For Pete

The Role of Acidity in Tumour Development

Kieran Smallbone
New College – University of Oxford
Trinity Term, 2006
Abstract of thesis submitted for the degree of Doctor of Philosophy

Abstract

Acidic pH is a common characteristic of human tumours. It has a significant impact on tumour progression and response to therapies. In this thesis, we utilise mathematical modelling to examine the role of acidosis in the interaction between normal and tumour cell populations.

In the first section we investigate the cell–microenvironmental interactions that mediate somatic evolution of cancer cells. The model predicts that selective forces in premalignant lesions act to favour cells whose metabolism is best suited to respond to local changes in oxygen, glucose and pH levels. In particular the emergent cellular phenotype, displaying increased acid production and resistance to acid-induced toxicity, has a significant proliferative advantage because it will consistently acidify the local environment in a way that is toxic to its competitors but harmless to itself.

In the second section we analyse the role of acidity in tumour growth. Both vascular and avascular tumour dynamics are investigated, and a number of different behaviours are observed. Whilst an avascular tumour always proceeds to a benign steady state, a vascular tumour may display either benign or invasive dynamics, depending on the value of a critical parameter. Extensions of the model show that cellular quiescence, or non-proliferation, may provide an explanation for experimentally observed cycles of acidity within tumour tissue. Analysis of both models allows assessment of novel therapies directed towards changing the level of acidity within the tumour.

Finally we undertake a comparison between experimental tumour pH images and the models of acid dynamics set out in previous chapters. This analysis will allow us to assess and verify the previous modelling work, giving the mathematics a firm biological foundation. Moreover, it provides a methodology of calculating important diagnostic parameters from pH images.

Acknowledgements

My thanks go to the Engineering and Physical Sciences Research Council whose funding, through the Life Sciences Interface Doctoral Training Centre, has made this research possible. To my supervisors Mike Brady, Dave Gavaghan and Philip Maini. Mike for his limitless enthusiasm, Dave for his unwavering confidence in me, and Philip for keeping the other two in check and never missing a typo. To Bob Gatenby at the University of Arizona for his unending stream of new ideas. To my housemates Rob Freeman and Lucy Helme. Rob for keeping me company whilst I burnt the midnight oil, and Lucy for doing the same at more sensible times of the day. To my girlfriend Larry for proof-reading well beyond the call of duty. And finally my thanks go to my Grandad, for teaching me to calculate the volumes of tin cans and wardrobes when I was barely out of nappies.

Contents

Chapter 1

Introduction

1.1 Motivation

Cancer is a group of more than 100 distinct diseases characterised by the uncontrolled growth of abnormal cells in the body. It is a major cause of sickness and death throughout the world. In 1996 there were 10 million new cancer cases worldwide, and six million deaths attributed to cancer. In 2020 there are predicted to be 20 million new cases and 12 million deaths [4]. The reason for this increase is two-fold. Firstly, infection as a major cause of serious ill-health is in decline, giving way to noncommunicable diseases common in an ageing population, such as cardiovascular disease and cancer. Secondly, and perhaps more significantly, a globalisation of unhealthy lifestyles, such as smoking and poor diet, will increase cancer incidence.

Cancer arises through changes at the genetic level that allow the cells to escape from the cooperative behaviour associated with normal tissue. One factor that makes cancer research so difficult is that, at the microscopic level, these cells are extremely heterogeneous. No single set of genetic changes is found in every transformed cell population [21], and even within a single tumour varying subpopulations often coexist. Despite these microscopic differences, at the macroscopic level cancers maintain the common lethal traits of invasion (movement into adjacent normal tissue) and metastasis (formation of secondary tumours in distant organs).

The commonality of aggressive cancer cell behaviour despite widespread genotypic diversity has led researchers to believe that several of the lethal phenotypic traits of cancer may not be the direct result of genetic changes, but rather may arise from the unique physiological environments of tumours. The tumour microenvironment is significantly different from that of normal tissue; its chaotic vasculature leads to a significant decrease in supply of essential nutrients and a decrease in the removal of waste products. One biomarker that has received much attention recently is tumour hypoxia (poor oxygenation). Fig. 1.1 shows that near-zero oxygen levels are observed at distances of only 150 μm from a feeding blood vessel. As such, areas of hypoxia are commonplace within tumours. Identifying the regions of hypoxia within tumours has been a focus of recent research, as cells residing within such regions are known to be resistant to various radio- and chemo-therapeutic strategies. Moreover, cells subjected to chronic hypoxia are found to be more aggressive, displaying increased metastasis, invasion and mutation (see Table 1.1).

Returning to Fig. 1.1 and Table 1.1, we see that acidity also plays a key role in tumour development. Like hypoxia, regions of low pH are commonplace within tumours. Moreover, the effects of acidosis are similar to those of hypoxia, with acidosis promoting metastasis, invasion and mutation. However, unlike hypoxia, there has been relatively little research into acidity as a factor for promoting tumour development. The reasons for this are unclear; it may be that many researchers assume that the acidity is simply a byproduct of

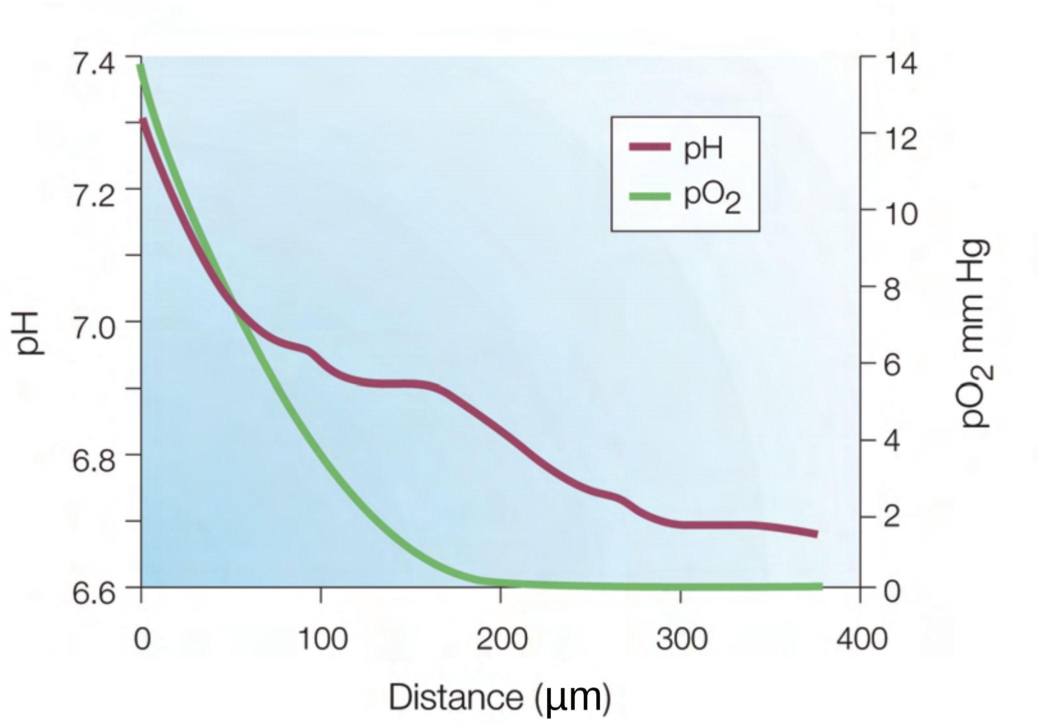

Figure 1.1: Tumour extracellular pH and partial pressure of oxygen (pO_2) as a function of distance from a vessel wall, as measured *in vivo* in MCF-7 breast cancer cells. Reproduced with permission from Nature Reviews Cancer [45] © 2004 Macmillan Magazines Ltd.

Hypoxia	Acidosis
Radioresistance	Radioresistance
Drug resistance	Resistance to anthracyclines
Metastasis and invasion	Metastasis and invasion
Increased mutation rate	Mutagenesis/clastogenesis
Apoptosis	Apoptosis
Gene expression induced by HIF	–

Table 1.1: Consequences of tumour hypoxia and acidosis [45]. As tumours become hypoxic and acidic, their progression is accelerated and resistance to various therapeutic strategies occurs. For definitions the terms, see Appendix A.

low oxygen levels. Cells respond to periods of hypoxia by converting to anaerobic respiration, or glycolysis, which in turn produces lactic acid and brings about lower tissue pH. However, the work of Warburg in the 1920s [119] showed that the increased reliance on glycolysis to produce energy in many aggressive tumours occurs even in the presence of sufficient oxygen. As such, tumour acidification is an intrinsic property of both poor vasculature and altered tumour cell metabolism, and occurs independently of hypoxia.

Acidosis plays a critical role in tumour development, yet has received very little attention by researchers. Within the thesis, we aim to address this problem. Specifically, a number of questions need to be answered. Firstly, it is not known why tumour cells evolve to rely on glycolysis as a means of energy production, even in the presence of sufficient oxygen. Anaerobic respiration is more than an order of magnitude less efficient than its aerobic counterpart, producing only 2 ATP per glucose in comparison to approximately 36 ATP. Moreover, the hydrogen ions produced as a result of glycolysis cause a consistent acidification of the extracellular space that is potentially toxic. Intuitively, one would expect evolutionary forces to select against this inefficient and toxic phenotype, in favour of more optimal metabolic regimes. Secondly, it is not known how this increased acid production will affect tumour cells, or more specifically why the resultant low pH correlates with increased growth and invasion, as set out in Table 1.1. Through addressing these questions, we aim to develop novel therapeutic strategies directed towards manipulating tumour pH and slowing tumour development.

We approach the understanding of tumour acidosis from a mathematical perspective. Mathematical models were once thought of as too simplistic to describe complex tumour phenomena. However, it is becoming clear that intuitive approaches are insufficient to describe the non-linear interactions between tumour cells and their environment. The use of mathematics will grant us a new, quantitative, perspective on the role of acidity in tumour development, and allow us to determine critical parameters that cause the change from benign to invasive growth. The various directions from which we attack the problem are set out in the next section.

1.2 Thesis outline

Before moving to the main thrust of the thesis, we first introduce the field and outline the previous research that has a bearing on our work. In Chapter 2, we introduce the reader to the complex subject of cancer from a biological perspective. As mentioned above, cancer cells are extremely heterogeneous at the genetic level. Nonetheless, many cancers follow a similar well-defined ‘life-cycle’: progression from a single abnormal cell, through precancerous growth, to invasion and metastasis. We discuss the typical genetic changes that occur at each stage of development, and the evolutionary pressures that lead to these changes being adopted within a cancer cell population. Also discussed is the tumour microenvironment, specifically the changes leading to the acidification of tumours, and the effects this acidity will have, on both the tumoural and peritumoural normal tissue.

In Chapter 3, we move on to discuss previous mathematical models of cancer development. Whilst theoretical models contribute to only a tiny proportion of the research articles written on cancer, this still equates to over 50 000 papers [103]. An array of comprehensive review papers have been written detailing modelling approaches to specific aspects of

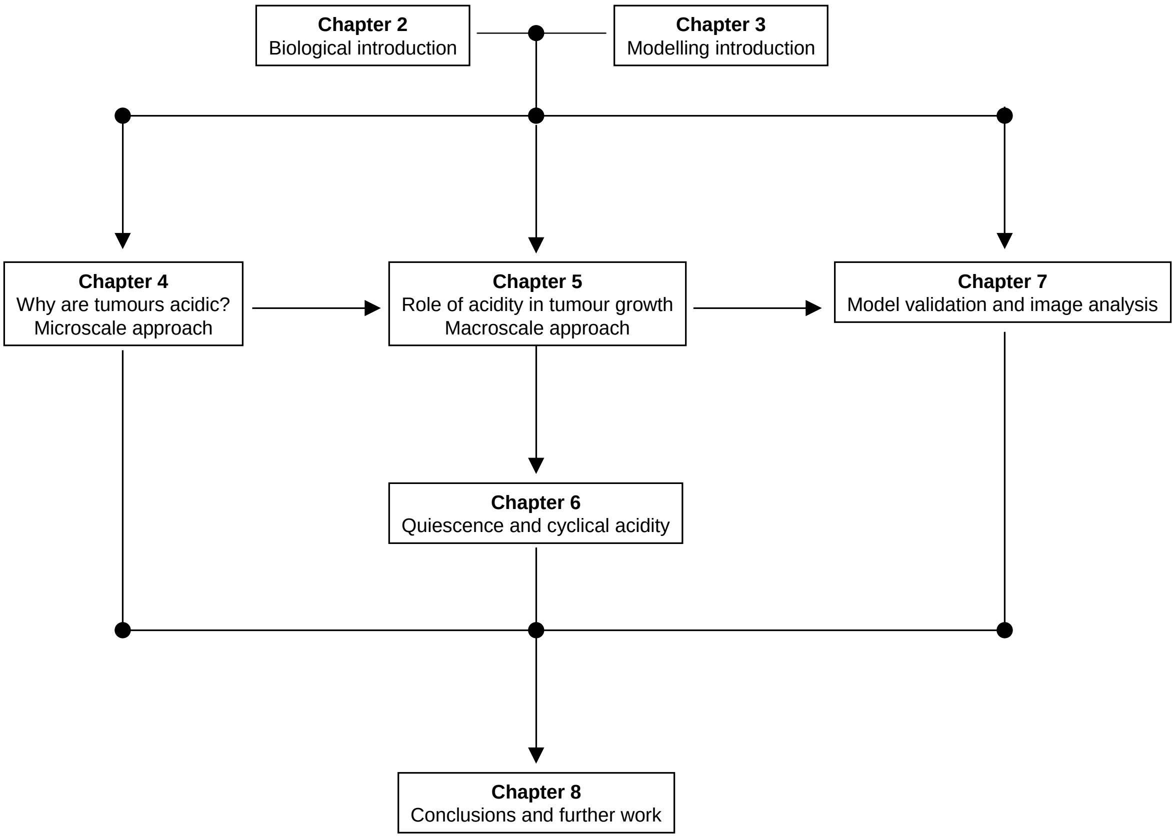

Figure 1.2: Schematic representation of thesis layout.

cancer. Rather than reproducing such a review here, the chapter subjects a small selection of representative models to in-depth review and analysis. The major benefit of this approach is that the advantages and shortfalls of each model may be clearly identified, guiding our model development in later chapters.

Chapters 4–7 present the main results of the thesis, linking together as is shown diagrammatically in Fig. 1.2. In Chapter 4, we address the question of why evolutionary pressures drive tumour cells to rely on highly inefficient anaerobic respiration as a means of energy production. Note that during the first steps in carcinogenesis, premalignant cells remain physically separated from their blood supply by a membrane, and hence nutrient supply and waste removal are limited. This observation is incorporated into a microscale cellular automaton model of the cell–cell and cell–microenvironment interactions. Cells in the model evolve in response to the local levels of the critical nutrients, oxygen and glucose, and hydrogen ion concentration. One major insight from the model is that, over the length scales of early carcinogenesis, glucose supply is not a limiting factor. As such, inefficient glucose metabolism is not important; rather, upregulation of glycolysis, coupled with resistance to the acid produced as a result of this process, is found to give cells a significant selective advantage, allowing proliferation in hypoxic regions.

We move on, in Chapter 5, to consider the role of acidity at the macroscopic level. Assuming that a mass of tumour cells displays increased acid production coupled with a resistance to low pH, we question what effect this has on its growth. Using a partial differential equation model, we predict that the hydrogen ions produced by the tumour will diffuse into the surrounding normal tissue, inducing cellular death. Thus we see that acidity provides a simple mechanism for cancer invasion. The model also predicts an acellular gap separating the advancing tumour and receding normal tissue fronts, a prediction observed experimentally [41]. A bifurcation parameter is found that determines the change, within our modelling framework, from a benign to invasive growth pattern. From this parameter an unexpected therapeutic strategy emerges; we show that further increasing the acidity within a tumour beyond a critical threshold may induce auto-toxicity and stop tumour growth.

Towards the end of Chapter 5, we extend the model to include quiescent, non-proliferating tumour cells. Such cells are known to produce significantly less acid than their active counterparts. Inclusion of quiescent cells provides a more physiologically accurate description of the tumour and of the acid profile extending into the normal tissue. For the case of an avascular tumour, the behaviour observed through consideration of quiescent tissue is very similar to the basic model. However, in Chapter 6, we consider quiescence in a vascularised tumour, and quite different behaviour is observed. We find that cellular quiescence may induce cycles of acidity to occur within the tumour tissue. Whilst metabolite cycles within tumour tissue are a well-known phenomenon, these cycles had previously been assumed to occur due to fluctuations in blood supply. Our modelling work suggests that alternative mechanisms may also be responsible.

In Chapter 7, we undertake a comparison between the predicted pH profiles derived in Chapter 5 to experimental pH images. An excellent fit is found between the experimental and predicted profiles, which goes some way to justifying the previous modelling work undertaken. However, this chapter aims to achieve much more than model validation. Recent technological advances have led to the emergence of pH imaging as an alternative to existing techniques for functional tumour imaging in a clinical setting. The technique for comparing experimental and model pH profiles set out in the chapter leads to estimates for the model parameter values, one of which, cellular acid production rate, is known to correlate with tumour aggressiveness. This parameter may be used as a quantitative diagnostic tool, and knowledge of it for specific tumours could prove invaluable to the clinician.

Within this thesis, we answer a number of crucial questions about the role of acidity in tumour development. In Chapter 8, we draw the work together, comparing and contrasting current oncological beliefs with the results of our work. However, a number of questions remain unanswered, and our work has revealed further gaps in the understanding of the role of acidity in tumour development. We define those questions whose answers would be most fruitful in furthering our understanding and therefore our search for new and effective therapies. We also set out the mathematical techniques that we feel could be used to attack these new and unanswered problems.

Chapter 2

The biological basis of cancer

2.1 Introduction

Cancer has been recognised since antiquity, being first named by Hippocrates as ‘carcinos’, meaning crab, to describe the hard central tumour with blood vessels irradiating from it [87]. It is this borrowed observation which gives us the Latin word we now use: cancer. However, the first major steps in cancer research were not made until the mid-nineteenth century with increased understanding of cellular biology. Cancer was viewed as a cellular disease, arising through inappropriate cellular proliferation. This led to the interpretation of tumour growth as a Darwinian competition between normal and tumour cells. The vision of cancer as cells that have escaped the control of the organism and act egoistically is still very much present in current conceptions of cancer.

The modern view of cancer is as a molecular disease, focusing on the role of two families of genes – oncogene (growth promoter) activation and tumour suppressor gene (TSG, growth inhibitor) inactivation – in mediating tumour formation. Since the discovery of these genes in the 1970s, the molecular description of cancer has become increasingly complex. For most tumours the specific genes involved in cellular transformation are not known. Moreover, no general rules have emerged from the vast amount of data we have to hand. This is merely molecular confirmation of previous observations that cancer cell populations are extremely heterogeneous, displaying a wide range of characteristics due to the stochastic nature of their development.

During the intervening period, the first half of the twentieth century, the origin and mechanisms of cancer were sought in a variety of disciplines that were developed at that time – microbiology, biochemistry, genetics, etc. The models that emerged from this era have since been integrated into the current molecular descriptions. The various approaches to cancer research seen during the past 150 years are perceptively captured by Cairns [17]: "At each stage, the characteristics of the cancer cell have been ascribed to some defect in whatever branch of biology happens at the time to be fashionable and exciting."

In this chapter, the complex subject of cancer is introduced from a biological perspective, drawing together both historical and modern observations. Particular emphasis is placed on outlining the cancer 'life-cycle': progression from a single abnormal cell, through pre-cancerous and noninvasive growth, to invasion and metastasis. We discuss the genetic changes that occur at each stage of development, and the microevolutionary pressures that lead to these changes being adopted within the cell population. We also discuss the evolutionary pressures and genetic changes leading to the acidification of tumours, and the effects this acidity will have, both on the tumoural and peritumoural normal tissue.

2.2 Cancer as somatic evolution

The human body operates as a society whose individual members are cells, reproducing through mitosis (normal cell division) and organised into collaborative assemblies known as tissues. The cells communicate through elaborate cell–cell signalling mechanisms, to ensure each cell behaves in a socially responsible manner – dividing, differentiating, quiescing (ceasing division) or dying as is appropriate for the good of the organism. From an ecological perspective, there is no natural selection occurring within a healthy human body – self-sacrifice rather than survival of the fittest is the overriding rule.

The basic ingredient of cancer involves escaping from this cooperative behaviour. Cancer begins with a single cell mutating to give it a selective advantage over its neighbours, allowing it to proliferate more quickly and become the founder member of a growing mutant clone, known as a tumour. Successive rounds of mutation, competition and selection lead to progressively less collaborative and more dangerous cells. Thus cancer development can be viewed as somatic (of the body) evolution [12]. Whilst this process occurs on a time-scale of months or years in a population of cells within the body, it depends on those same principles of mutation and natural selection that govern the long-term evolution of living organisms.

Cancer cells are defined by two clear heritable properties. They are:

- hyperplastic: they reproduce in defiance of the normal restraints on cell division.
- invasive and metastatic: they invade and colonise territories usually occupied by other cell types.

It is the combination of these two properties that makes cancers particularly lethal. An isolated cell that does not proliferate in excess of its counterparts can cause no significant damage to the host, regardless of its other disagreeable characteristics. A cell that escapes normal growth control will give rise to a tumour – an abnormal mass of tissue serving no useful function to the host. Whilst this tumour remains as a solid mass, it is known as benign, and surgical removal will usually be curative. A tumour is referred to as cancerous if it is malignant – if the cells have acquired the ability to break away from the tumour mass and invade the adjacent tissue. These cells may also enter blood vessels or lymph channels and form secondary tumours, or metastases, at other sites in the body. The more widely a cancer spreads, the harder it is to eradicate.

2.3 Multistage carcinogenesis

Most tumours take many years to grow and form to the point where they produce clinical manifestations. The cells have defects in many aspects of their behaviour as a result of multiple heritable changes, acquired through successive rounds of natural selection. Many mutations are needed because cellular processes are controlled in complex and interconnected ways; cells employ redundant regulatory mechanisms to help maintain control over their behaviour. In order to act malignantly, a cell must disrupt many regulatory systems to throw off its normal restraints.

Not all cancers require the same pattern of mutations to evade the body's regulations: a cancer of the colon may need mutations in six or seven specific oncogenes and TSGs, whilst a childhood leukaemia may require only one [4]. However, many types of cancers are diagnosed with an age-dependent incidence implicating between four and seven rate-limiting, stochastic events [101]. The similar pattern of development observed by most tumours has crystallised into the multistage theory of carcinogenesis, explaining the genetic changes involved in each stage of clonal expansion. We outline this theory below.

2.3.1 Initiation and *in situ* growth

There is much controversy over exactly how cancer starts. It is generally accepted that most cancers derive from genetic mutation in a single cell [3]. However, the specific factor that triggers this mutation is difficult to identify. Carcinogens (cancer-causing agents) may be present in food, water, air, chemicals or radiation to which people are exposed. Moreover, cancers may be induced by viruses.

Over 90% of cancers are of epithelial origin [4], and as such we shall focus here on the development of carcinomas (malignant epithelial tumours). Epithelial cells cover the internal and external surfaces of the body (including skin) and line the respiratory and alimentary tracts. Importantly, epithelial cells metabolise ingested carcinogens, which goes some way to explain the statistic above.

Epithelium consists of cells joined by small amounts of cementing substances. It is attached to a thin ‘basement membrane’ that separates the epithelial cells from the stroma (external connective tissue). As such, epithelial tissue is typically avascular – the cells are physically separated from the blood supply by the basement membrane. Epithelia are classified into types on the basis of the number of cellular layers (e.g. simple, meaning monolayer) and the shape of the superficial cells (e.g. squamous, meaning flattened).

Epithelial tissue has a number of important functions, including the formation of glands (secretory organs) through infolding of an epithelial sheet.

Many of the genetic changes required to form cancer occur early during carcinogenesis, before the onset of malignant growth. The specific sequence of changes required to transform normal colonic epithelial cells through adenoma (benign epithelial growth) to colorectal cancer were first detailed by Fearon and Vogelstein in 1990 [33] (see Fig. 2.1). As mentioned above, the heritable changes accumulated vary according to the specific cancer type under consideration. However, analysis of the adaptations undergone during colorectal tumorigenesis will give insight as to the typical changes needed to escape normal regulatory mechanisms.

Two of the genetic changes – in Ras and TGFβ (tumour growth factor β) – allow the tumour cells to undergo mitosis more regularly than their normal counterparts. Normal cells require positive mitotic growth signals before they may move from a quiescent (resting) state into an active state. These signals may come from diffusive growth factors, extracellular matrix (ECM) components or cell-cell adhesion molecules (CAMs), and are tightly regulated by the Ras protein. The structurally altered form of Ras within colorectal cancer cells releases a constant flux of mitotic signals into the cell, without need for stimulation from these upstream growth signals.

Multiple anti-growth signals also operate within normal tissue to maintain quiescence and homeostasis (system stability). TGFβ is one such anti-growth signal, blocking cellular advance to mitosis. In colorectal cancer, as with many other human cancers, response to this anti-growth signal is negated. This disruption occurs through a variety of mechanisms, including down-regulation of TGFβ receptors, or elimination of their downstream targets.

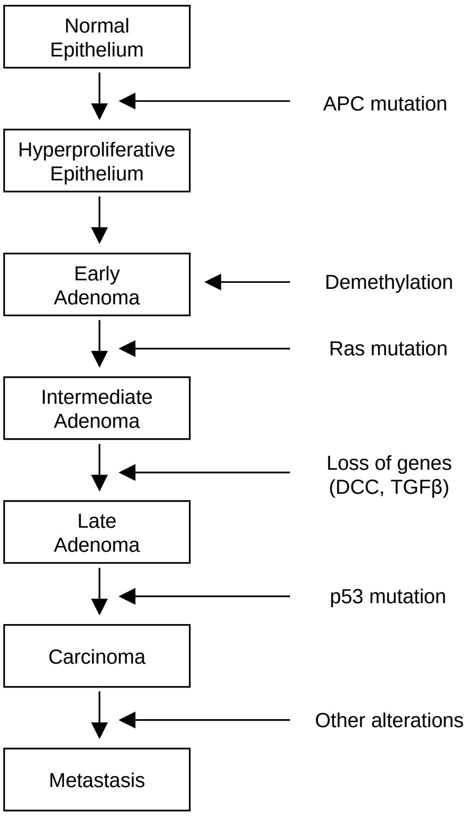

Figure 2.1: Fearon-Vogelstein diagram ('Vogelgram') depicting the genetic changes that occur in the transformation from normal colonic epithelial cells to colorectal cancer. Adapted from [33].

A completely different cellular change is elicited by inactivation of the p53 tumour suppressor protein. Signals evoked by abnormalities such as DNA damage, hypoxia and oncogene overexpression are funnelled via p53, triggering a precisely choreographed series of events, ultimately leading to cell death. This programmed, suicidal cell death, known as apoptosis, is intrinsic to virtually all cells of the body, acting to destroy cells that represent a threat to the organism. Cells undergoing apoptosis shrink and break into small, membrane-wrapped fragments, before being engulfed by phagocytic cells such as macrophages. This mechanism ensures cell contents are not released into the surrounding tissue. In contrast, necrosis – non-programmed, progressive, degradative death – often brings about an inflammatory response from the host.

Resistance to apoptosis through p53 inactivation, combined with growth signal autonomy and insensitivity to anti-growth signals, leads to an uncoupling of a cancer cell's proliferation from signals in its environment. In principle, these changes should be sufficient for tumour growth. However, cancers in fact display genetic and epigenetic (non-genomic) changes in a wide variety of cellular systems. For example, the Fearon-Vogelstein diagram depicts a period of demethylation. In normal cells methyl groups attach to DNA, preventing gene transcription; methylation patterns are passed on to daughter cells at mitosis. Widespread loss of methyl groups during colorectal tumorigenesis allows more genes to be transcribed, thus allowing greater phenotypic diversity during somatic evolution.

The intensive research carried out over the past twenty-five years has led to an understanding of the proteins involved in cellular growth signalling, and how these proteins interact. Through analysis of this signalling pathway and the ways in which it is modified in cancer cells (Fig. 2.2), therapeutic strategies directed towards halting cell proliferation

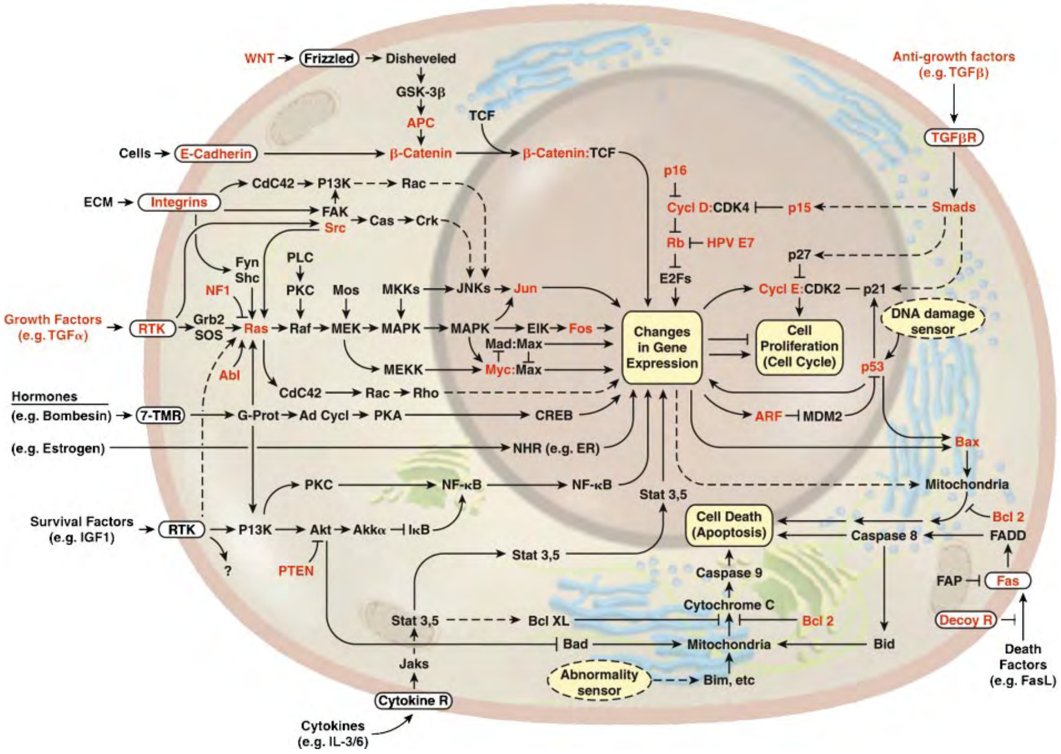

Figure 2.2: The growth signalling circuitry of a mammalian cell. Arrows denote promotion and bars denote inhibition. The genes known to be functionally altered in cancer cells are highlighted in red. Reprinted from [55] © 2000 with permission from Elsevier.

may be suggested. However, much of the pathway is still poorly understood; as further layers of complexity are added to the picture, mathematical techniques will be needed to understand the dynamics of cellular growth.

2.3.2 Tissue invasion and metastasis

The variety of heritable changes outlined in Section 2.3.1 occur early during carcinogenesis. During this stage, transformed epithelial cells remain encapsulated from the surrounding tissue by the basement membrane. The blood vessels also remain outside the basement membrane, so the tumour has only a limited nutrient supply available. These noninvasive, or *in situ*, growths are usually asymptomatic – unfortunate as *in situ* tumours may be cured through removal.

In the next stage of tumour progression, a tumour breaches the basement membrane. Once tumours have broken through this membrane, cancerous cells may invade the adjacent tissue. They can also enter the bloodstream; this often occurs via lymph vessels – vessels whose function is to drain tissues of the fluid (lymph) that filters across vessel walls from blood. However, throughout the lymphatic system there exist lymph nodes that can trap cancer cells and bacteria travelling through the body in lymph. Should a cancer cell successfully enter the circulatory system, either through lymph vessels or breaching of a blood vessel's lining, it will be transported throughout the body and may eventually lodge in the capillaries of another distant organ. Here the cells will begin to multiply, forming a secondary tumour known as a metastasis.

Metastases are the cause of around 90% of deaths from cancer [110]. Whilst the primary (original) tumour can be controlled by many available therapies, widespread metastatic disease is very difficult to treat.

Invasion and metastasis are extremely complex multifactorial processes, whose genetic and biochemical bases are poorly understood. From a mechanistic perspective, both processes are closely related, utilising changes in the physical coupling of cells to the microenvironment and activation of extracellular proteases. Cells possessing invasive or metastatic capabilities are known to have alterations in cell-cell adhesion molecules, which mediate cell-to-cell interactions, and integrins, which link cells to extracellular matrix substrates. Degradative proteolytic enzymes, such as urokinase-type plasminogen activator (uPA) and matrix metalloproteinase (MMP), are used to breach the basement membrane, clear a path through adjacent tissue, and subsequently pass through vessel walls. Many of these proteases (such as uPA [62]) are produced not by the epithelial cancer cells, but rather by conscripted stromal and inflammatory cells, before being wielded by the carcinoma cells [125]. These layers of complexity go some way to explaining the elusiveness of invasion and metastasis.

2.3.3 Angiogenesis

The nutrient supply and waste removal provided by blood vessels is crucial for cell survival and proliferation. As such, avascular tumours lacking their own network of blood vessels cannot grow beyond a size of $2 - 3$ mm^3. Angiogenesis (the formation of new capillaries), along with invasion and metastasis, is an important step in the transition from a small, abnormal mass of cells to life-threatening malignant growth.

Initially, tumour cells lack the ability to stimulate capillary development. At some point in their development, they begin to synthesise proteins capable of stimulating angiogenesis. One such protein of particular importance is known as vascular endothelial growth factor (VEGF). VEGF binds to the receptors of endothelial cells (the building blocks of capillaries), inducing them to penetrate the tumour nodule and begin the process of constructing a network of vessels. As the endothelial cells proliferate, they secrete growth factors that stimulate the growth and motility of tumour cells. Cancer cells also produce proteins that inhibit the growth of blood vessels. As such, initial capillary development relies on a balance between the levels of pro-angiogenic and anti-angiogenic molecules.

In addition to apoptotic response, p53 plays an important role in mediating angiogenesis. Under hypoxic conditions, the mediator hypoxia inducible factor 1 (HIF-1) is rapidly induced, activating transcription in many oxygen-sensitive genes including VEGF. The role of p53 here is to counterbalance VEGF expression through upregulating expression of the anti-angiogenic agent thrombospondin-1 (TSP-1) [27], ensuring inappropriate angiogenesis does not occur. In cells bearing mutant p53 (the most common genetic defect in solid tumours), hypoxia induced VEGF is not so readily controlled by anti-angiogenic molecules such as TSP-1, hence neovascularisation may occur.

The point of development at which cancer cells acquire the 'angiogenic phenotype' varies widely. The failure of tumour cells to stimulate angiogenesis may be responsible for the long-term dormancy of many primary and metastatic tumours. However, the periods of hypoxia experienced by carcinoma *in situ* may induce sustained production of angiogenic factors. Whilst capillaries cannot pass through the intact basement membrane during this early phase of development, the transformed cells can immediately induce capillary growth once the membrane is breached.

Perhaps the most promising therapeutic strategies being developed now involve targeting tumour vasculature. Within normal tissue, angiogenesis is primarily a developmental process, used for example during organ formation, and thus anti-angiogenic therapy will have minimal side effects. Moreover, this therapy is targeted at host endothelial cells, rather than cancer cells, hence the emergence of drug-resistant clones is not possible. Further research in this area will be of considerable interest.

In Fig. 2.3, the various stages of development of malignant growth are summarised.

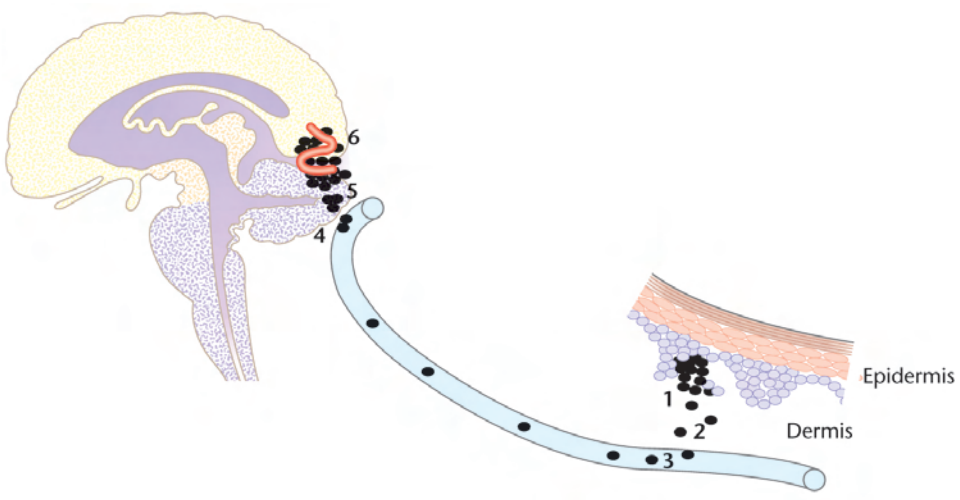

Figure 2.3: Malignant cells (1) invade surrounding normal tissue, (2) detach from the primary tumour mass and (3) enter the circulatory system. To successfully metastasise these cells must (4) attach to suitable endothelium and exit the circulation, (5) invade local tissue and (6) induce angiogenesis. Reproduced with permission from [4].

2.3.4 Why cancer kills

Having described the process by which cancer grows and disseminates throughout the body, we now move on to describe briefly the effects of tumours on an individual. Most tumours take many years to form and grow to the point where they produce clinical manifestations. Both primary and secondary metastatic tumours may affect an individual locally, through compression, invasion and destruction of normal tissues. In addition, these tumours may produce systemic effects known as paraneoplastic syndromes, through release of substances into the bloodstream. The symptoms of a tumour will vary widely depending on the location of the tumour, the tumour's functional activity and any acute events that occur as the tumour mass grows and evolves.

From a local perspective, the expansive growth of benign tumours and the more destructive growth of malignant tumours may erode normal tissue surfaces. This leads to the development of ulcers and bleeding and creates conditions that favour infection. Tumours growing near an organ may often interfere with the organ's function. For example, benign tumours of the parathyroid gland over-secrete parathormone, causing systemic calcium levels to rise, leading to muscle fatigue and nausea. However, organ systems are tremendously robust; for example, an animal can survive after removal of two-thirds of its liver, and regenerate the lost tissue within a week [32]. Unless the organs are stretched, causing pain, tumours of solid organs will remain silent until the tumour is far-advanced. This explains why metastases are often present at the time of diagnosis, and why people seldom die of organ failure.

Tumours may also develop inside hollow organs such as the gastrointestinal tract or ducts carrying secretions from one organ to another. The carcinoma developing here will invade and grow circumferentially around the wall of the organ or duct, in a 'napkin ring' shape [84]. This ring will thicken with time, and ultimately the lumen (cavity of the tube) will become obstructed. Whilst these blockages can cause death, they will present themselves symptomatically, and may be relieved though surgery. As such, hollow organ obstruction is usually not a cause of death.

By far the most common cause of death from cancer occurs at the systemic, rather than local, level. Cachexia [18], or body wasting, is particularly common at the advanced stages of malignant growth. Cancer starves and debilitates the patient, leaving them unable to mount adequate anti-inflammatory responses. Such debilitation leads to infection; the saprophytic organisms (organisms growing on dead matter) that live in the mouth or nose invade the patient, causing pneumonia, septicemia and death. It is likely that one of the molecules contributing to cachexia is tumour necrosis factor α (TNFα) – a molecule normally synthesised by immune cells, but somehow activated by malignant tumour cells [11].

The wasting and incapacitation is what makes cancer so terrifying, as much as the pain associated with tumour growth and metastasis. Ultimately, via infection, it is this wasting which leads to death.

2.4 Why are tumours acidic?

The tumour microenvironment is significantly different from that of normal tissue. Marked fluctuations can be seen in glucose, lactate, acidic pH and oxygen tensions. These variations have their roots in poor perfusion and metabolic changes. The chaotic vasculature of tumours creates an unbalanced blood supply and significant perfusion heterogeneities. As a consequence, many regions within tumours are found to be transiently or chronically hypoxic. Cells respond to periods of hypoxia by converting to anaerobic respiration, or glycolysis, which in turn produces lactic acid and brings about lower tissue pH. However, the pioneering work of Warburg [119, 120, 124] showed that tumour acidification can occur independently of hypoxia. The increased reliance on glycolysis to produce energy in many aggressive tumours occurs even in the presence of sufficient oxygen [117, 119]. Thus acidification is an intrinsic property of both poor vasculature and altered tumour cell metabolism.

The constitutive adoption of increased aerobic glycolysis is known as the glycolytic phenotype. The inefficiency of this anaerobic metabolism is compensated for through a

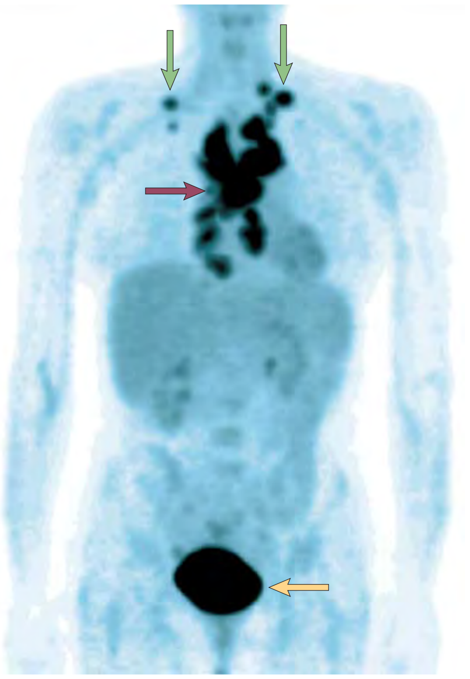

Figure 2.4: Tumour imaging with ^{18}fluorodeoxyglucose positron emission tomography (FDG-PET). The tumours (purple and green arrows) show high levels of FDG uptake, indicative of increased glucose uptake. The bladder (yellow arrow) also has high activity, due to excretion of FDG. Reproduced with permission from Nature Reviews Cancer [45] © 2004 Macmillan Magazines Ltd.

several-fold increase in cellular glucose consumption. This phenomenon is now routinely exploited for tumour imaging through ^{18}fluorodeoxyglucose positron emission tomography (FDG-PET) [26, 38] (see Fig. 2.4). PET has confirmed that the vast majority ($> 90\%$) of human primary and metastatic tumours demonstrate increased glucose uptake indicating abnormal metabolism. Furthermore, PET has been used to show a direct correlation between tumour aggressiveness and the rate of glucose consumption [30].

The presence of the glycolytic phenotype in the malignant phenotype of such a wide range of cancers arising in multiple different sites seems inconsistent with the evolutionary model of carcinogenesis described in Section 2.1. Due to the Darwinian dynamics at play, it is reasonable to assume the common appearance of a specific phenotype within a large number of different cancer populations is evidence that it must confer a significant growth advantage. However, the proliferative advantages gained from altered glucose metabolism are far from clear. Firstly, anaerobic respiration is more than an order of magnitude less efficient than its aerobic counterpart, producing only 2 ATP per glucose in comparison to approximately 36 ATP (see Fig. 2.5). Secondly, the hydrogen ions produced as a result of glycolysis cause a consistent acidification of the extracellular space that is potentially toxic [104]. In particular, an acidic microenvironment results in tissue damage due to cell death and degradation of the extracellular matrix [102]. Intuitively, one would expect the Darwinian forces prevailing during carcinogenesis to select against this inefficient and environmentally toxic phenotype, in favour of more optimal metabolic regimes.

Gatenby and Gillies [45] proposed that evolution of aerobic glycolysis is the result of environmental constraints imposed by the morphology of the ducts in which premalignant lesions evolve (see Fig. 2.6). Initially, normal epithelial cells grow along the basement membrane, with the epithelial layer at most a few cells thick. Homeostasis mechanisms do not normally allow growth of these cells away from the basement membrane. However, following initial genetic events in the carcinogenesis pathways such as those depicted by the Fearon-Vogelstein model [33], the cells become hyperplastic, leading to a thickening of the epithelial layer, pushing cells into the lumen and away from the basement membrane. Since the blood vessels remain outside the basement membrane, nutrients and waste must diffuse over longer and longer distances. As a result, it is likely that hyperplastic cells beyond the Thomlinson–Gray limit of 100–150 μm [113] from the basement membrane will experience profound hypoxia, which will initiate a sequence of critical cellular adaptations and environmental changes. Specifically, it is proposed that hypoxia leads to constitutive upregulation of glycolysis which, in turn, results in increased H^+

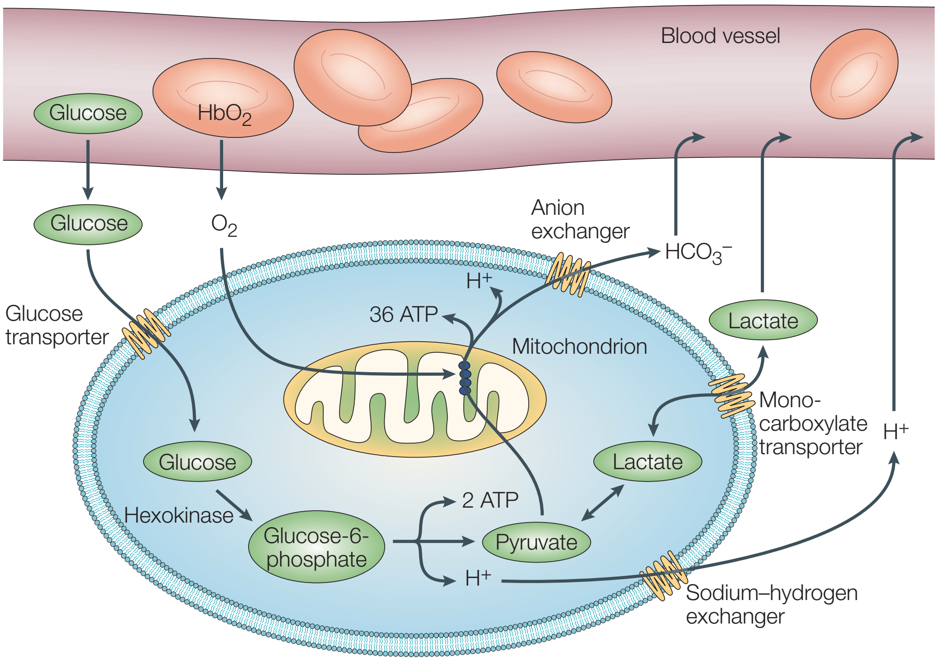

Figure 2.5: Glucose metabolism in a mammalian cell. Glucose and oxygen are delivered via the blood to tissues, reaching the cell by diffusion. Glucose molecules are taken up through specific transporters, before being converted to pyruvate via glycolysis, generating 2 ATP molecules per glucose molecule. In the absence of oxygen, pyruvate is reduced to lactate and exported from the cell. Under oxygenated conditions, this reduction is inhibited in normal cells (the Pasteur effect [95]); pyruvate instead enters the mitochondrion, generating approximately a further 34 ATP. Reproduced with permission from Nature Reviews Cancer [45] © 2004 Macmillan Magazines Ltd.

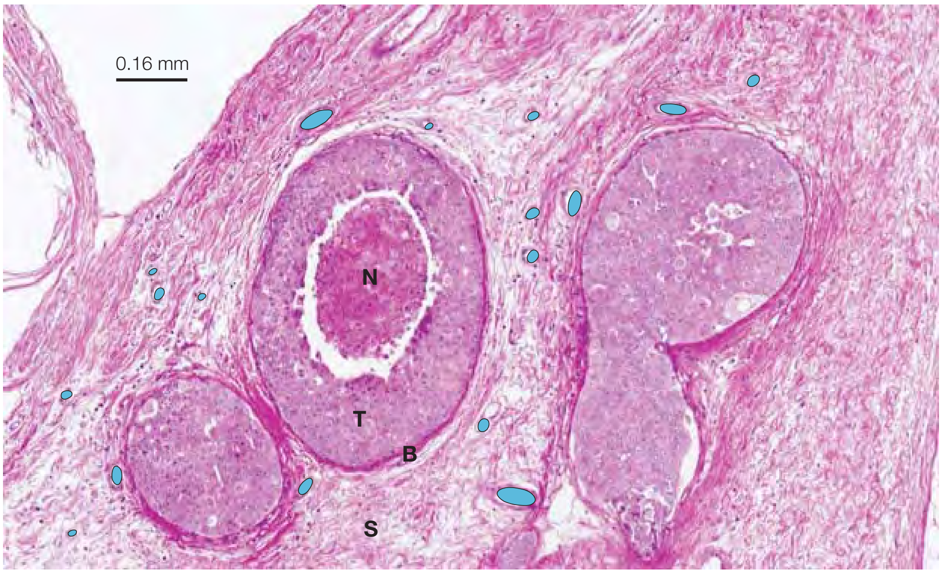

Figure 2.6: A late-stage ductal carcinoma *in situ* (DCIS). Blood vessels (blue) are seen in the stroma (S) surrounding the tumour (T), but are prevented from entering the tumour itself by the intact basement membrane (B). The tumour centre is necrotic (N). Reproduced with permission from Nature Reviews Cancer [45] © 2004 Macmillan Magazines Ltd.

production and acidification of the microenvironment. This decreased extracellular pH (pH_X) is toxic to the local populations because it induces p53-dependent apoptosis due to increased caspase activity. This selects for cells that are resistant to acid-induced toxicity resulting in further evolution of new phenotypic properties that, for example, increase the number and activity of Na^+/H^+ antiporters on the cell surface, or possess mutations in p53, caspase or other components of the acid-induced apoptosis pathways. Acidosis also selects for motile cells that eventually breach the basement membrane, gaining access to existing and newly formed blood and lymphatic routes for metastasis.

This model is supported by experimental observations of upregulation of cellular responses to hypoxia in regions of premalignant DCIS (ductal carcinoma *in situ*) and PIN (intraepithelial neoplasia) most distant from the basement membrane. This includes upregulation of HIF (hypoxia-inducible factor) and related proteins such as carbonic anhydrase IX and GLUT-1 (glucose transporter 1) [73, 127] (see Fig. 2.7).

Gatenby and Gawlinski [41, 42] point out that the tumour phenotype that emerges from the sequence above, constitutively increasing acid production and becoming resistant to acid-induced toxicity, has a powerful growth advantage over its normal counterparts. They propose that acidity may play a key role in mediating tumour invasion. The key idea is that the transformed tumour metabolism with increased use of glycolysis and acid secretion alters the microenvironment by substantially reducing tumour extracellular pH, usually by more than 0.5 pH units. The H^+ ions produced by the tumour then diffuse along concentration gradients into the adjacent normal tissue. This acidification leads to death of normal cells due to activation of p53-dependent apoptosis pathways, as well as loss of function of critical pH-sensitive genes. Tumour cells, however, are relatively resistant to acidic pH_X, due to mutant p53 genes. Whilst normal cells die in environments with a persistent pH below about 7, tumour cells typically exhibit a maximum proliferation rate in a relatively acidic medium (pH 6.8) [20]. As a result, the tumour edge can be seen as forming a travelling wave progressing into normal tissue, preceded by another travelling wave of increased microenvironmental acidity.

Cancer cell populations are extremely heterogeneous, displaying a wide range of genotypic and phenotypic differences [34]. For example, studies of clinical breast cancers have shown that every cell line exhibited a novel genotype [66]. As a result, no prototypic cancer cell can be defined. It is likely that several of the lethal phenotypic traits of cancer, such as invasion and metastasis, are not the direct result of genetic changes, but rather arise from the unique physiological environments of tumours. Tumour hypoxia and acidity, for

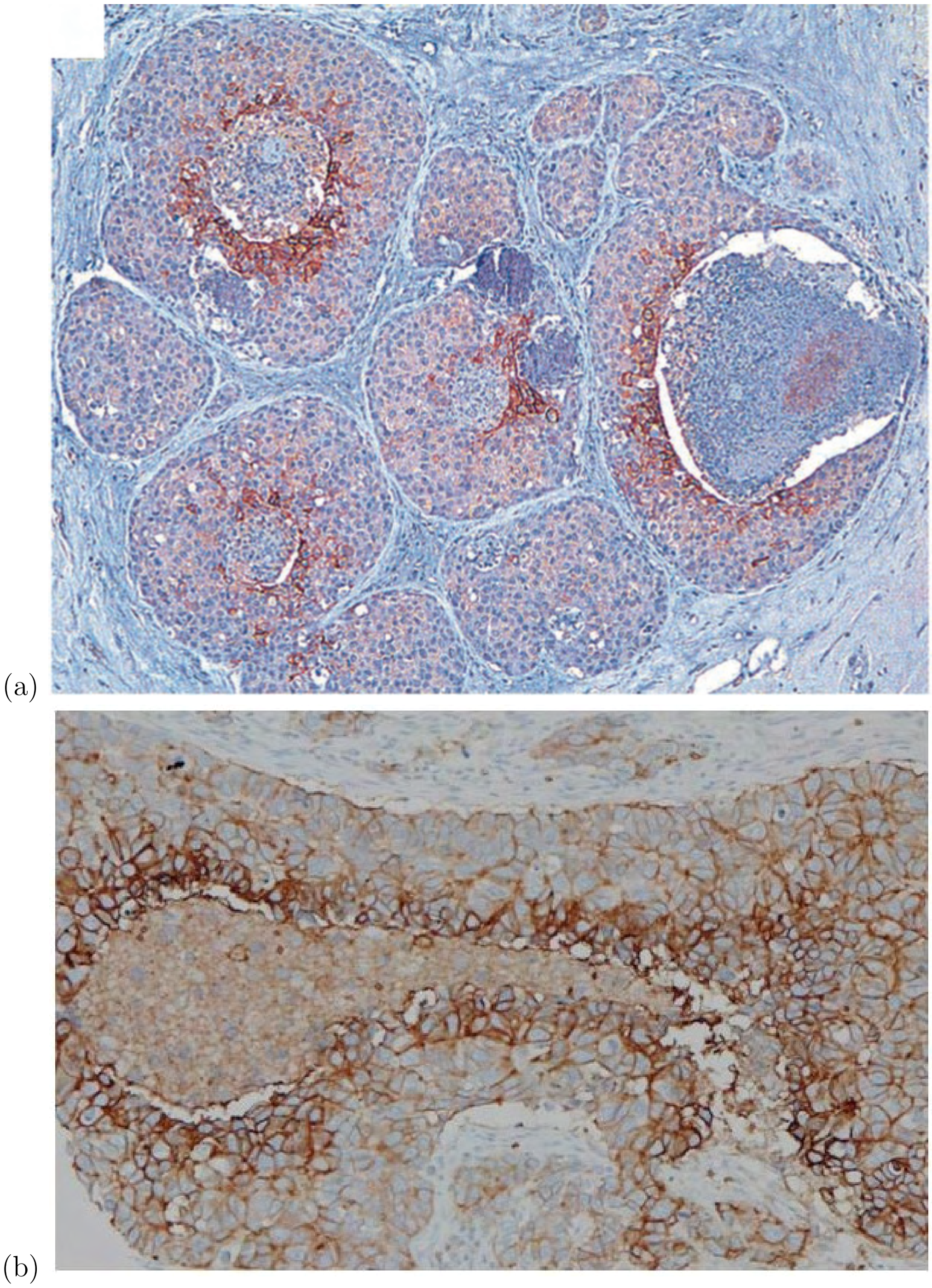

Figure 2.7: (a) DCIS, stained for expression of the hypoxia-inducible protein carbonic anhydrase IX. The image shows an increase in hypoxic response with distance from the basement membrane. Reprinted from [127] with permission from the American Society for Investigative Pathology. (b) DCIS, stained for the glucose transporter 1 protein. Again the image shows a marked increase in expression in cells furthest from the membrane, indicating they are adapting to hypoxia by increasing glucose transport. Figure courtesy of R. Gatenby.

example, significantly affect the treatment and progression of cancer. These effects can either be directly mediated by low pH or low pO_2, or they can result from selective pressure that these parameters place upon cells in hostile environments. Hypoxia and acidity are not simply phenomena of cancer growth, but may in fact be essential intermediates in the progression from benign to metastatic growth. Acidity, in particular, has been shown to have three clear effects on tumour phenotype: resistance to chemotherapy [98], increased mutation rate [88] and increased invasion [81].

2.5 Summary

In this chapter we have introduced the complex subject of cancer development from a biological perspective. Cancer may be seen as a somatic evolution process, whereby cancer cells escape from the cooperative behaviour associated with normal tissue, allowing them to have a selective advantage over their normal counterparts. Successive rounds of adaptation, competition and selection lead to progressively less collaborative and more lethal cells. In addition to proliferating in excess of their competitors, cancer cells may invade surrounding tissue, metastasise to form distant colonies within the body and acquire their own vasculature.

Since the pioneering work of Fearon and Vogelstein, much effort has gone into determining the specific genetic and epigenetic changes that occur during cancer development. Whilst a picture of the growth signalling circuitry in the cell is coming into focus, much of the pathway is still poorly understood. Moreover, the wide range of genotypic and phenotypic differences between each cancer cell population means it is not possible to define a prototypic cancer cell. The genotypic variation between cancer populations is surprising when one considers their common phenotypic traits of invasion, metastasis and angiogenesis. This leads us to consider the possibility that these lethal phenotypes may not be directly caused by genetic differences, but rather may be mediated by the harsh physiological environment associated with tumours [108].

One such environmental difference is tumour acidification, resulting in part from a constitutive change in tumour glucose metabolism. At first sight, this metabolic change seems at odds with an evolutionary model of cancer development, as it is both inefficient and toxic. However, altered glucose metabolism and acidification is near-universally observed in human primary and metastatic tumours, suggesting that these changes are essential in the progression from benign to metastatic growth. Throughout this thesis, we shall examine the evolutionary pressures that lead to tumour acidification, and the effects this has on tumour growth. The understanding gained from this will allow assessment of novel therapies directed towards manipulation of tumour pH.

Chapter 3

Modelling tumour development

3.1 Introduction

Non-linear processes dominate the way in which tumour cells interact with their microenvironment. It is clear that the intuitive, verbal reasoning approaches employed by many oncologists are insufficient to describe the resulting complex system dynamics. Nor can such approaches keep pace with the vast amounts of oncological data being published each year in response to the rapid technological advances in molecular biology. Rather, experience from other areas of science has taught us that quantitative methods are needed to develop comprehensive theoretical models for interpretation, organisation and integration of this data [46, 70]. Once thought of as too simplistic to describe complex tumour phenomena, we now see that mathematical models, continuously revised by new information, can be used to guide experimental design and interpretation.

Whilst there is a clear need for a more formal approach to biology [76], there is also a need for mathematical biologists to avoid *post hoc* explanations of observations, such as data fitting. To make experimental biologists take serious note, mathematical biologists must create models that generate *predictions* to be tested empirically. Alternatively, these models should address questions of a higher level, identifying all possible classes of biological phenomena that could arise from a given modelling premise [75]. One example of the former approach is the series of articles written by Hodgkin and Huxley in 1952, the final paper [59] combining both experimental data analysis and mathematical modelling. The authors derive a system of equations for describing the generation of an action potential in a squid giant axon and numerically determine a travelling wave solution, whose shape and speed agreed with their own experimental measurements. This work led to a Nobel Prize in 1963, and moreover drove research that resulted in the discovery of membrane ion channels [78]. An example of the latter approach is Turing's 1952 article [114], whose development of the idea that reaction-diffusion equations could provide spatially inhomogeneous patterns of chemical concentrations to trigger morphogenetic events, provided the theoretical framework for a number of biological applications.

Whilst theoretical modelling only contributes to around 5% of the research articles written on cancer, this figure still equates to over 50 000 papers [103]. Within this chapter, we clearly cannot describe every model of tumour development; for this, the reader is referred to various review articles focusing on tumour modelling history [7], avascular growth [103], colorectal cancer [116], angiogenesis [79], interactions with the immune system [1] and modelling drug delivery [61]. Here, instead, we subject a small selection of representative models to in-depth analysis. These models have been chosen both because of their impact on scientific research into cancer, and their relevance to this thesis. The benefit of this highly selective approach is that it enables us to fully identify each model's assumptions, defining equations and conclusions. Moreover, through outlining the papers that led to, and from, each of the models, the chapter will maintain the semblance of a standard review.

3.2 Greenspan (1972)

Many of the recent mathematical models found in the literature focus on the growth of multicellular spheroids (MCSs): clusters of cancer cells grown *in vitro* to mimic the early stages of *in vivo* avascular tumour growth and to test the applicability of new cancer treatment strategies [111]. MCSs have a well-defined structure, possessing a central core of necrotic cells, with proliferating cells restricted to the outer rim of the tumour. Existing models of MCS and avascular tumour development, essentially extensions of the early models of Burton [14] and Greenspan [51], describe the evolution of the tumour outer boundary in response to vital nutrients (in particular oxygen) and growth factors. Using the assumption of spherical or cylindrical symmetry, these models give good qualitative agreement with experimental results, reproducing both the growth patterns and macroscopic heterogeneities typical of MCSs and avascular tumours.

Greenspan's 1972 paper [51] describes a simple mathematical model of tumour growth. The tumour is assumed to act as an incompressible fluid; as such, local changes in the cell population, caused by the birth or death of cells, give rise to internal pressure gradients that induce cellular motion and the expansion or contraction of the tumour colony. The work extends previous models [14] by introducing cell–cell adhesion forces at the tumour periphery that maintain the tumour as a compact, solid mass. Subsequent tumour growth is determined by the interaction between these expansive and restraining forces.

The tumour is modelled as a sphere consisting of a central necrotic core ($r \leq R_D$), an intermediate layer of quiescent (non-proliferating) cells ($R_D \leq r \leq R_Q$) and an outer layer of proliferating cells ($R_Q \leq r \leq R_M$ – see Fig. 5.5). Necrotic cellular debris is assumed to continually disintegrate into simpler chemical compounds that are freely permeable through cell membranes. The cell volume lost in this way is replaced by cells pushed inward through adhesion or surface tension. Assuming that the rates of cell proliferation and necrotic disintegration are constant per unit volume (s and 3λ respectively), we find

$$R_M^2 \frac{dR_M}{dt} = \frac{s}{3}\left[R_M^3 - \max(R_D^3, R_Q^3)\right] - \lambda R_D^3. \tag{3.1}$$

Cancer cells are assumed to die when the concentration σ of a crucial nutrient falls below a critical level σ_l. Thus the necrotic radius R_D is defined by the relationship $\sigma(R_D) = \sigma_l$, whilst if $\sigma > \sigma_l$ everywhere, then we take $R_D = 0$. Note that the nutrient diffusion time-scale ($\sim$ minutes) is much shorter than the tumour growth time-scale ($\sim$ days), and hence as the tumour grows, the nutrient quickly redistributes and reaches equilibrium. Thus we may assume that σ is in diffusive equilibrium at all times. If the nutrient has constant diffusion rate k and is consumed by living cells at constant rate A per unit volume, then

$$\nabla^2 \sigma = \frac{A}{k} H(R_M - r) H(r - R_D), \tag{3.2}$$

where H denotes the Heaviside (or unit step) function, subject to the condition that $\sigma(R_M) = \sigma_\infty$ is constant at the tumour boundary.

Noting the finding that the mitotic index of proliferating cells tends to decrease with distance from the spheroid surface [112], Greenspan assumes that a chemical β must be produced within the tumour that inhibits mitosis once the concentration of the chemical reaches a critical level β_l; thus the quiescent radius is defined by $\beta(R_Q) = \beta_l$, whilst $R_Q = 0$ if $\beta < \beta_l$ everywhere.

Two different possibilities are then considered separately. The first model assumes that the chemical inhibitor is a result of inadequate nutrient supply, and a product of the necrotic material. Then we find

$$\nabla^2 \beta = -\frac{P}{\kappa} H(R_D - r), \tag{3.3}$$

where κ is the diffusion rate and P the production rate of β per unit volume, subject to the boundary condition $\beta(R_M) = 0$.

The second model assumes that the inhibitor is produced purely by the metabolic processes of living cells, in which case Eq. (3.3) becomes

$$\nabla^2 \beta = -\frac{P}{\kappa} H(R_M - r) H(r - R_D). \tag{3.4}$$

Using the non-dimensionalisation

$$\begin{aligned} \xi = \frac{R_M}{R_c}, \quad \zeta = \frac{R_Q}{R_c}, \quad \eta = \frac{R_D}{R_c}, \quad \tau = st, \\ Q^2 = \frac{\beta_l \kappa A}{(\sigma_\infty - \sigma_l) k P}, \quad \gamma = \frac{\lambda}{s}, \quad R_c = \left[\frac{6k}{A} (\sigma_\infty - \sigma_l) \right]^{1/2}, \end{aligned} \tag{3.5}$$

Greenspan provides solutions for both models. Qualitatively, both predict some overall similarities in the development of the spheroid, showing three distinct growth phases: initial exponential growth, followed by a degree of retardation, culminating in a final phase where both mitotic inhibition and cell death give rise to dormancy. However, each of the two models predicts a distinctly different growth pattern prior to arriving at the steady state. These results are reproduced in Figs. 3.1 and 3.2.

Details are given of a prototype experiment that could determine, from examination of the steady-state cell population, which of the two possibilities was the primary source

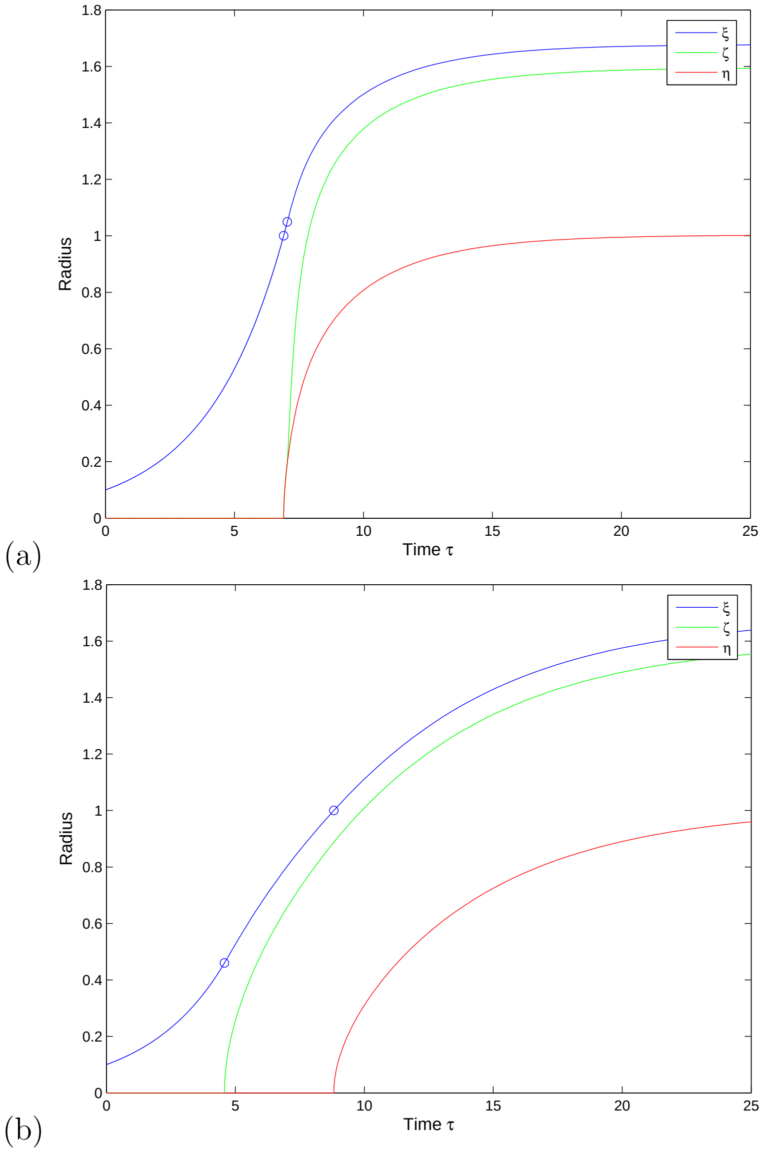

Figure 3.1: (From Eqs. (3.1)–(3.4).) Predicted growth patterns from Greenspan's models when inhibition is due to (a) dead material and (b) the metabolic wastes of live cells. Parameter values used are $\xi(0) = 0.1$, $\gamma = 0.22$, $Q = 0.25$ for the first model and $Q = 0.46$ for the second model. The three growth phases are separated by circles.

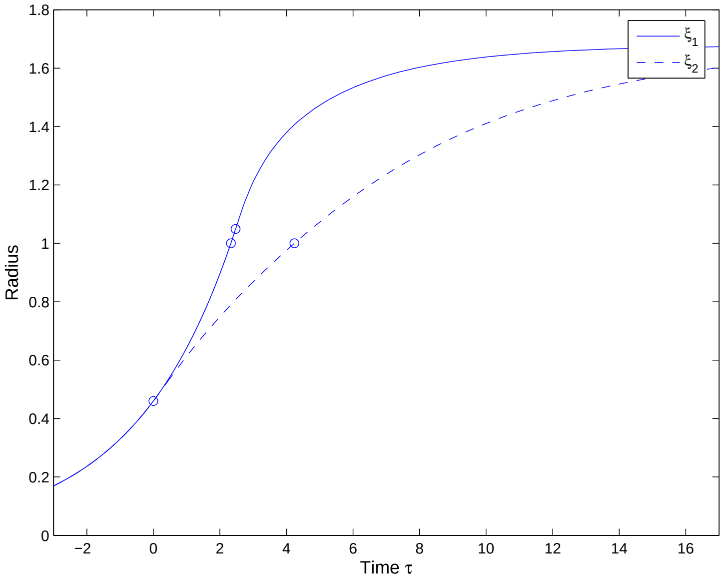

Figure 3.2: A comparison of the predicted outer tumour radius of the two models presented in Fig. 3.1. The models show differing growth patterns before arriving at a common steady state. Time is measured from the point of bifurcation.

of growth inhibition. This point is reiterated in a later paper [52]; regrettably, no such experimental work appears to have been undertaken.

As mentioned at the start of this section, the model of Greenspan is an antecedent to much of the subsequent mathematical literature relating to tumour development. McElwain and co-workers investigated the effects of non-uniform oxygen consumption on the model, and apoptosis as a cell loss mechanism [82, 83]. Greenspan himself extended his own modelling framework to consider the stability of equilibrium-sized tumours to asymmetric perturbations [53], work continued by Byrne and co-workers [15, 16]. Many recent models have incorporated differing degrees of cell movement, such as considering cells to move in a convective manner [37, 121]. The recent work of Franks *et al.* [37] is representative of a modern approach to the topic, drawing together many previous approaches to model the early growth of a ductal carcinoma *in situ* in a cylindrically-symmetric breast duct. Tumour growth is again largely determined by nutrient availability. However, the work goes much further, describing the live and dead tumour cell concentrations, the concentration of fluid within the duct, nutrient concentration, local velocity and pressure. This modelling framework is then used to study the effects of the tissue viscosity on the shape of the tumour boundary, including the extent to which the cells adhere to the duct wall.

One of the first to tackle the problem, Greenspan's model of tumour growth has stood the test of time. A reformulation of his approach forms the basis of our model of acid-mediated growth described in Chapter 5.

3.3 Gatenby and Gawlinski (1996)

Population ecology methods provide a means for examining tumours, not as an isolated collection of transformed cells, but rather as an invading species in a previously stable multicellular population. Gatenby [39, 40] models the tumour-host interface as a network of interacting normal and malignant cell populations, using coupled, non-linear differential equations. The interactions are then explored to define the crucial parameters that control tumourigenesis and to demonstrate the limitations of traditional therapeutic strategies.

Tumour cell populations, as with any invading population in biology, must directly perturb their environment in such a way as to facilitate their own growth while inhibiting the growth of the original community. The commonality of altered tumour metabolism, in particular the adoption of the glycolytic phenotype in most cancers, led Gatenby and Gawlinski to propose the acid-mediated tumour invasion hypothesis [41, 42], as discussed in Section 2.4. The authors propose that tumour cells' increased acid secretion, coupled with their resistance to low extracellular pH, may provide a simple but complete mechanism for cancer invasion.

The hypothesis is modelled as a system of three coupled partial differential equations (PDEs), determining the spatio-temporal distribution of three fields: the normal tissue density N_1, the tumour tissue density N_2, and the concentration of excess hydrogen ions L. The model includes: (1) logistic cellular growth; (2) normal cell death due to exposure to acid; (3) acid production by tumour cells; (4) acid reabsorption and buffering; and (5) spatial diffusion of acid and cells. It takes the form

$$\frac{\partial N_1}{\partial t} = r_1 N_1\left(1 - \frac{N_1}{K_1}\right) - d_1 L N_1, \tag{3.6}$$

$$\frac{\partial N_2}{\partial t} = r_2 N_2\left(1 - \frac{N_2}{K_2}\right) + D_2 \nabla \cdot \left[\left(1 - \frac{N_1}{K_1}\right)\nabla N_2\right], \tag{3.7}$$

$$\frac{\partial L}{\partial t} = r_3 N_2 - d_3 L + D_3 \nabla^2 L, \tag{3.8}$$

where r_1 and r_2 are the growth rates of the normal and tumour cell populations, respectively, K_1 and K_2 their carrying capacities, D_2 the diffusion coefficient for tumour cells, d_1 the normal cell susceptibility to acid, r_3 the rate of hydrogen ion production by tumour cells, d_3 the combined rate of acid removal by blood vessels and buffering, and D_3 the diffusion coefficient for hydrogen ions in tissue. Notice that there is no normal cell diffusion within the model, in recognition of the fact that healthy tissue is well-regulated and participating normally in an organ. Notice also that the tumour diffusion coefficient is constructed such that when normal tissue is at its carrying capacity, the diffusion coefficient for tumour tissue is zero and the tumour is confined. This final assumption is at the heart of the model: tumour tissue is unable to spread without first diminishing the surrounding healthy tissue from its carrying capacity.

In non-dimensional form, Eqns. (3.6)–(3.8) become

$$\frac{\partial \eta_1}{\partial \tau} = \eta_1(1-\eta_1) - \delta_1 \Lambda \eta_1, \tag{3.9}$$

$$\frac{\partial \eta_2}{\partial \tau} = \rho_2 \eta_2(1-\eta_2) + \Delta_2 \nabla_\xi \cdot [(1-\eta_1)\nabla_\xi \eta_2], \tag{3.10}$$

$$\frac{\partial \Lambda}{\partial \tau} = \delta_3(\eta_2 - \Lambda) + \nabla_\xi^2 \Lambda. \tag{3.11}$$

The system has four spatially-homogeneous steady states:

- $\eta_1 = 0$, $\eta_2 = 0$: the trivial solution.
- $\eta_1 = 1$, $\eta_2 = 0$: corresponding to normal healthy tissue with no tumour cells present.
- $\eta_1 = 1 - \delta_1$, $\eta_2 = 1$: corresponding to tissue consisting of both normal and tumour cells at an intermediate level, which may be interpreted as a benign or non-invasive tumour.
- $\eta_1 = 0$, $\eta_2 = 1$: corresponding to total tumour invasion.

Linear stability analysis [89] shows us that the trivial state and the state corresponding to normal cells alone are unconditionally unstable. Both the invasive state and the coexisting state are conditionally, but mutually exclusively, stable. The critical parameter is found to be $\delta_1 = d_1 r_3 K_2 / d_3 r_1$. Depending on the value of this dimensionless parameter, either the steady state for total destruction of normal tissue ($\delta_1 > 1$) or the steady state with the tumour and normal cells coexisting ($\delta_1 < 1$) is stable. Thus as the value of δ_1 passes through the critical value of 1, the entire system will change from a benign pattern of growth to a malignant one. For example, increased tumour vascularity will increase K_2

and push the system to an unstable steady state. This is consistent with data [35] showing that the acquisition of the angiogenic phenotype radically and abruptly alters the tumour growth pattern from non-invasive, slow growth to rapidly expanding, invasive growth.

Late-time travelling wave solutions [89] to Eqs. (3.9)–(3.11) are computed in Fig. 3.3. The first point of note is that the model predicts a smooth pH gradient extending from the tumour edge into the peritumoural tissue. The authors reanalyse data presented by Martin and Jain [80] relating to *in vivo* interstitial pH profiles for the VX2 rabbit carcinoma and its surrounding normal tissue, demonstrating that the data are consistent with the presence and approximate range of the pH gradient predicted by the model. Most significantly, however, the model predicts that (when $\delta_1 > 1$) there exists a previously unrecognised acellular gap separating the advancing tumour and receding host tissue fronts. In subsequent *in vitro* experiments, the authors found that, of 21 specimens of human squamous cell carcinoma of the head and neck, 14 were judged to show such a gap (see Fig. 3.4). Naked nuclei and morphologically disrupted cells were frequently observed scattered within the gap, or at its edge, as predicted by the model.

One problem with the model, generally ignored by reviewers, regards the ‘benign’ growth pattern observed when $\delta_1 < 1$, as presented in Fig. 3.3 (b). Whilst the tumour tissue does not have the capacity to destroy all the host tissue here, nor is there any mechanism to halt the tumour’s growth. As such, this growth pattern does not accurately represent benign growth. We return to this point in Chapter 5.

Despite the apparent success of Gatenby and Gawlinski’s model in examining large, clinically apparent tumours, its relevance to early tumour growth is not clear. Continuous partial differential equation models are well suited to modelling large populations, but

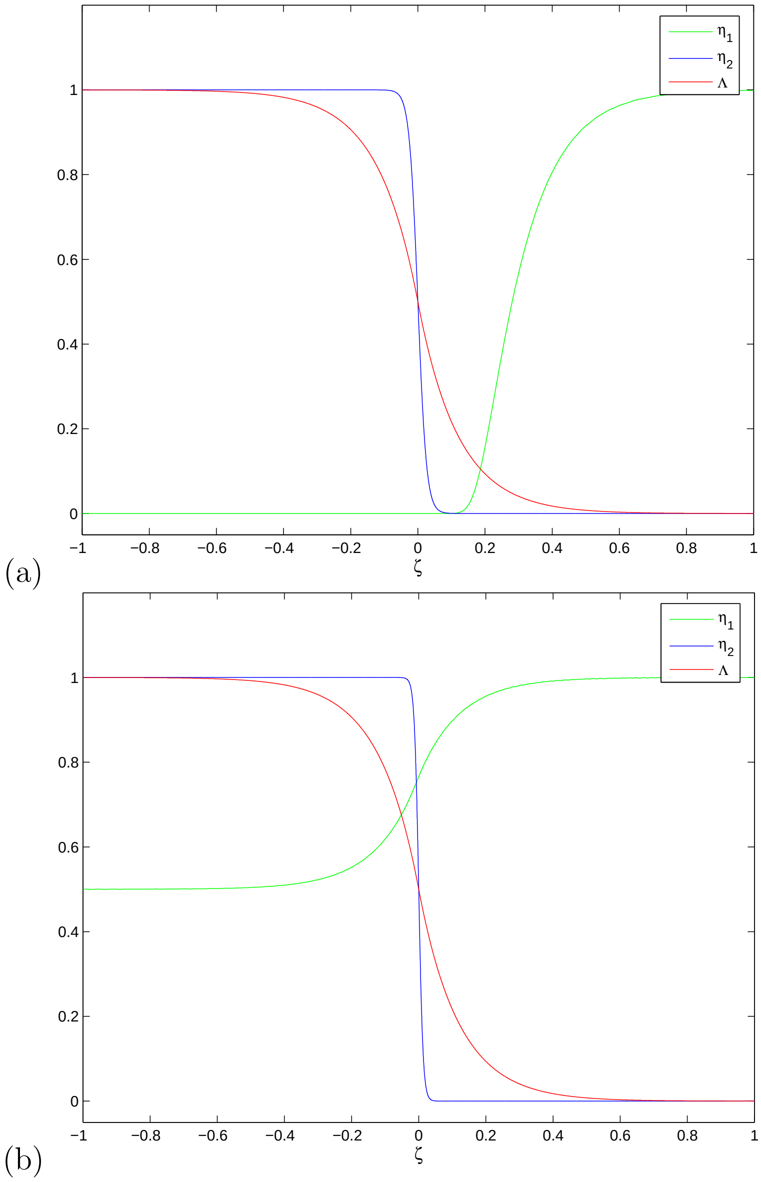

Figure 3.3: (From Eqs. (3.9)–(3.11).) Late-time travelling wave solutions to Gatenby and Gawlinski's model, with respect to the moving coordinate $\zeta = \xi - c\tau$. Waves are propagating from left to right and parameter values used are $\rho_2 = 1$, $\Delta_2 = 4 \times 10^{-5}$ and $\delta_3 = 70$. (a) The invasive case with $\delta_1 = 12.5 > 1$. Notice the formation of an acellular gap separating the advancing tumour (η_2) and receding host tissue (η_1) fronts. (b) The benign case with $\delta_1 = 0.5 < 1$. Notice the coexistence of tumour and host tissue behind the wave front. In both cases there is a smooth pH gradient (Λ) extending from the tumour edge into the surrounding normal tissue.

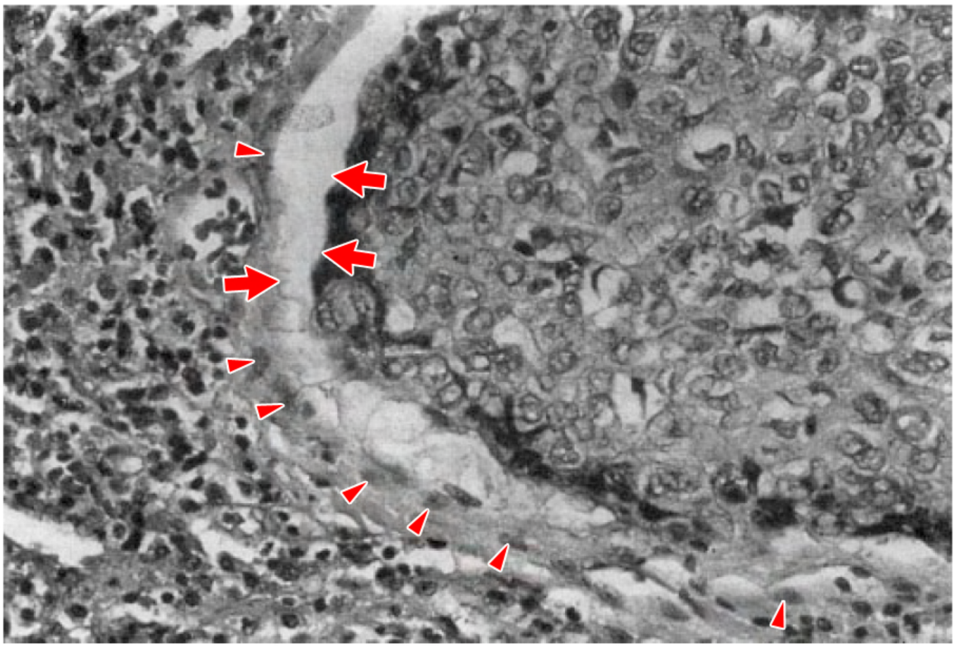

Figure 3.4: Formalin-fixed micrograph of the tumour-host interface (arrows) from human squamous cell carcinoma of the head and neck. A hypocellular gap at the interface associated with disrupted normal cells (arrowheads) is identified. The gap size ranges from 10–100 μm. Reproduced with permission from [96].

individual-based models such as cellular automata (CA) are more appropriate when the activity of individual cells must be considered. Traditional CA methods lack the ability to deal with continuously varying elements such as substrate diffusion and utilisation. Thus Patel *et al.* [92] developed a hybrid CA (see also [2, 5]) to evaluate the acid-mediated invasion hypothesis. The model incorporates normal cells, tumour cells, empty space and native microvessels as the automaton elements. Diffusion of glucose and H^+ ions to and from the microvessels, and their utilisation or production by cells are modelled through the solution of differential equations. Individual cells are then updated according to the local glucose and H^+ concentration.

The model predicts that even a small tumour nodule of 21 cells (in a 200×200 automaton) is able to generate sufficient changes in the local microenvironment to degrade the normal tissue and allow tumour growth. Early tumour growth is shown to be critically dependent on H^+ production by transformed cells and the level of vasculature. A variety of tumour morphologies are observed through varying these factors. This includes tumours growing to large volumes with declining growth rates or highly necrotic growth with the development of tumour chords. Some tumours even demonstrate initial growth followed by a decrease in tumour volume representing spontaneous regression.

The model of Gatenby and Gawlinski is the first to consider acidity as a mechanism mediating tumour growth. The prediction of a previously unobserved acellular gap separating the normal and tumour tissue goes a long way to validating their hypothesis. However, neither the PDE nor the CA formulation are capable of reproducing a benign growth pattern. We return to this point in Chapter 5.

3.4 Casciari *et al.* (1992)

A wide range of mathematical and computational models have been used to study the various mechanisms underlying nutrient consumption and metabolism [60, 71]. The computational model of Banaji *et al.* [8] is a typical example; the authors describe a model of the human brain circulation, one of its constituent parts being "a basic model of brain metabolic biochemistry". The Banaji *et al.* model is, in fact, anything but basic, describing in detail each of the many reactions taking place during cellular glucose metabolism. The main drawback to this approach is that there are over 100 parameters, many of which are unknown and difficult to estimate experimentally.

At the other end of the complexity scale is an interesting paper by Webb *et al.* [123], examining the dynamics that lead to tumour cells maintaining their intracellular pH at physiological levels, despite an acidic extracellular pH. Acknowledging the difficulties in parameterising their model, the authors adopt a purely qualitative approach, investigating how general functional shapes affect the steady-state pH levels. In a subsequent paper [122], the authors extend this work to examine the effect of pH on the secretion and activity of two classes of proteinases known to promote invasion through extracellular matrix degradation.

Casciari *et al.* [19] is one of few experimentally validated models of cellular nutrient dynamics. Their model considers the interaction of tumour cells with oxygen a, glucose b, lactate ions c, carbon dioxide d, bicarbonate ions e, chloride ions f, hydrogen ions g and sodium ions h. The work provides a model of tumour cell glucose metabolism, which is used to determine metabolite profiles within the tumour. It goes on to incorporate these profiles in a model of tumour growth; however, we shall focus on the early part of the paper here.

The oxygen and glucose consumption rates were based on previous experimental work [20];

$$P_a = -\rho_c\Big(A_a + \frac{B_a}{C_b C_g^m}\Big)\Big(\frac{C_a}{C_a + k_{ma}}\Big), \tag{3.12}$$

$$P_b = -\rho_c\Big(A_b + \frac{B_b}{C_a}\Big)\Big(\frac{1}{C_g^n}\Big)\Big(\frac{C_b}{C_b + k_{mb}}\Big), \tag{3.13}$$

where P_i denotes the net production rate of metabolite i, C_i its extracellular concentration and ρ_c is the number of cells per unit volume. Note that the functional forms for these rates arise from empirical considerations, rather than biochemistry. Assuming the forms of Eqs. (3.12) and (3.13) to be correct, the authors measured changes in EMT6/Ro breast carcinoma oxygen and glucose consumption with varying levels of oxygen, glucose and pH to find the parameters therein. These parameter values may be found in Table 3.1.

A schematic representation of the simple model of glucose metabolism proposed by Casciari *et al.* is given in Fig. 3.5. The authors make a number of reasonable assumptions, in particular that the intracellular and extracellular concentrations of carbon dioxide are equal, and that lactic acid fully disassociates into lactate and hydrogen ions in the extracellular space. They also appear to assume that the chloride/bicarbonate antiport plays a negligible role, though this is not mentioned explicitly. Then, through stoichiometric analysis (conservation of reactants) and the assumption of no net current flow, production rates $P_c, \ldots, P_h$ are obtained for the remaining metabolites.

$$P_c = -(2P_b - P_a/3), \tag{3.14}$$

$$P_d = -k_f C_d + k_r C_e C_g, \tag{3.15}$$

$$P_e = k_f C_d - k_r C_e C_g - P_a, \tag{3.16}$$

Parameter	Value	Units	Reference
ρ_c	2.01×10^{8}	$\mathrm{cell/cm^3}$	[19]
A_a	7.16×10^{-17}	$\mathrm{mol/cell \cdot s}$	[20]
B_a	2.02×10^{-21}	$\mathrm{mol \cdot mM^{1.921}/cell \cdot s}$	[20]
m	0.921	1	[20]
k_{ma}	4.64×10^{-3}	mM	[20]
A_b	1.93×10^{-21}	$\mathrm{mol \cdot mM^{2.21}/cell \cdot s}$	[20]
B_b	1.94×10^{-23}	$\mathrm{mol \cdot mM^{2.21}/cell \cdot s}$	[20]
n	1.21	1	[20]
k_{mb}	4×10^{-2}	mM	[77]
k_f	5.88×10^{-2}	1/s	[8]
k_r	74.5	1/s	[8]
C_{ao}	5×10^{-2}	mM	[8]
C_{bo}	2.09	mM	[8]
C_{co}	1.90	mM	[8]
C_{do}	1.78	mM	[8]
C_{eo}	25.1	mM	[8]
C_{go}	5.62×10^{-5}	mM	[8]
C_{ho}	1.38×10^{2}	mM	[8]

Table 3.1: Parameter values used in Casciari *et al.* [19] model.

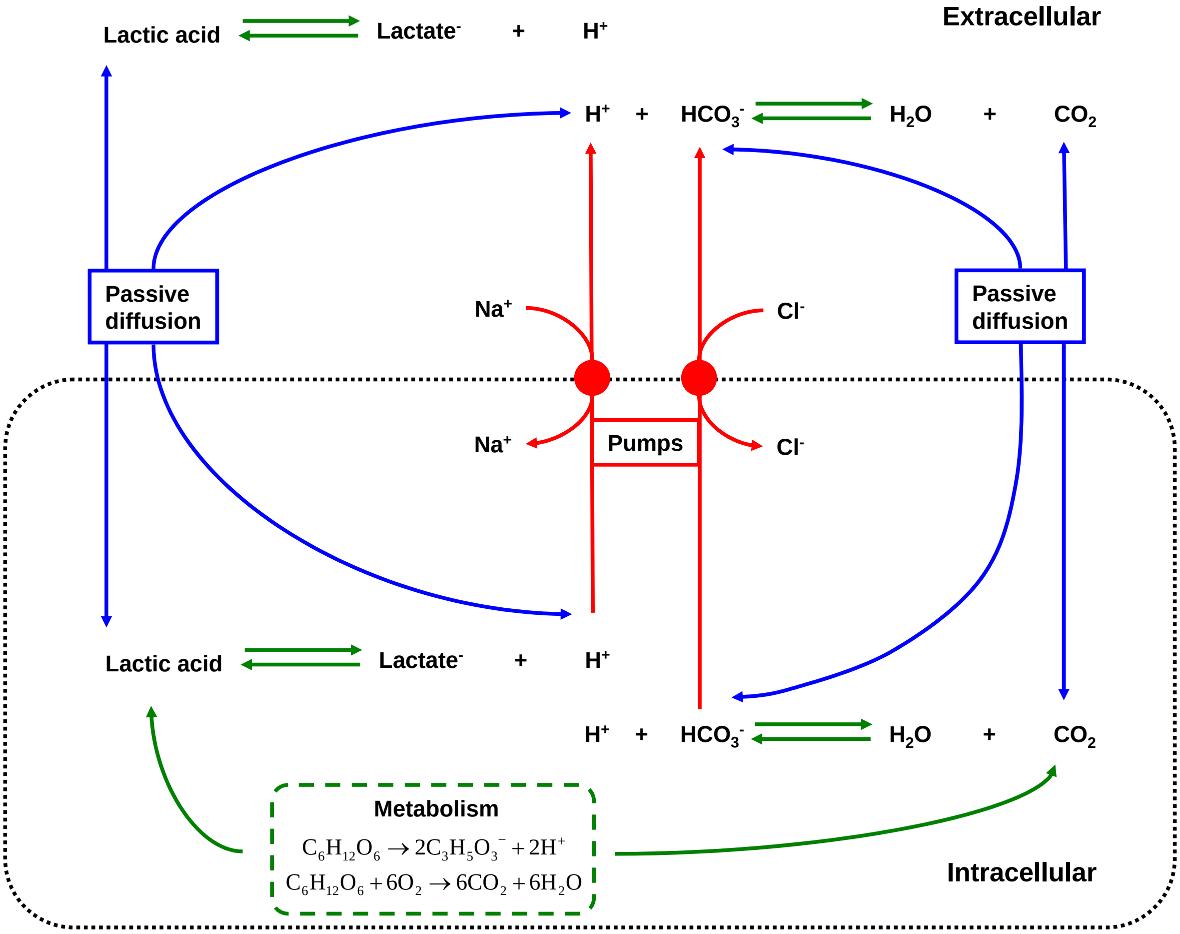

Figure 3.5: A model of oxygen, glucose and pH regulation, waste product transport and buffering for a tumour cell and its surroundings. Adapted from [20].

$$P_f = 0, \tag{3.17}$$

$$P_g = k_f C_d - k_r C_e C_g - P_a + P_c, \tag{3.18}$$

where k_f and k_d are the forward and reverse rates, respectively, of dissociation of carbon dioxide into bicarbonate.

Normal extracellular metabolite concentrations C_{io} (except for chloride, $i = f$) are given in Table 3.1. The chloride level is then calculated by the assumption of zero net charge at each point. Using these concentrations as base values, typical solutions to the metabolic model are given in Fig. 3.6. The consumption/production rates Π_i are given by normalising the rates P_i by their base values ($P_a = -1.46 \times 10^{-2}$ mM/s, $P_b = -6.35 \times 10^{-2}$ mM/s, $P_g = 0.122$ mM/s). In (a) we see that as the oxygen level increases, oxygen uptake (Π_a) follows typical Michaelis-Menten kinetics, increasing to a steady-state. Contrastingly, as oxygen increases, glucose uptake (Π_b) and hydrogen ion production (Π_g) fall, due to reduced reliance on glycolysis as a means of energy production (the Pasteur effect [95]). However, this effect is severely reduced compared to normal cells; in well-oxygenated conditions, normal tissue relies only on aerobic respiration to produce energy, so by conservation of reactants $P_b/P_a \approx 1/6$. For EMT6/Ro cells, however, $P_b/P_a \approx 4$ – a 24-fold increase in glucose uptake. In (b), we see that glucose consumption also follows Michaelis-Menten kinetics. The figure also shows that as glucose concentration increases, oxygen consumption decreases, a property of tumour cells known as the Crabtree effect [23]. Notice that, as C_b drops below 7×10^{-2} mM, we see an unexpected sharp rise in hydrogen ion production. This is due to an inconsistency in the model – for very low glucose levels, $P_b/P_a < 1/6$, and there is insufficient glucose consumed to react with the amount of oxygen consumed by the cell.

This model of cellular respiration is then used to answer quantitative questions about the expected pH inside tumours. This aspect of the work is not reproduced here. We do note, however, that one of the major problems with the paper is not specifying many of the parameter values used.

Notwithstanding the problems outlined above, Casciari *et al.* is one of very few experimentally-grounded models of cellular metabolism, focusing on the metabolic dynamics of tumour growth. Of particular interest would be construction and analysis of

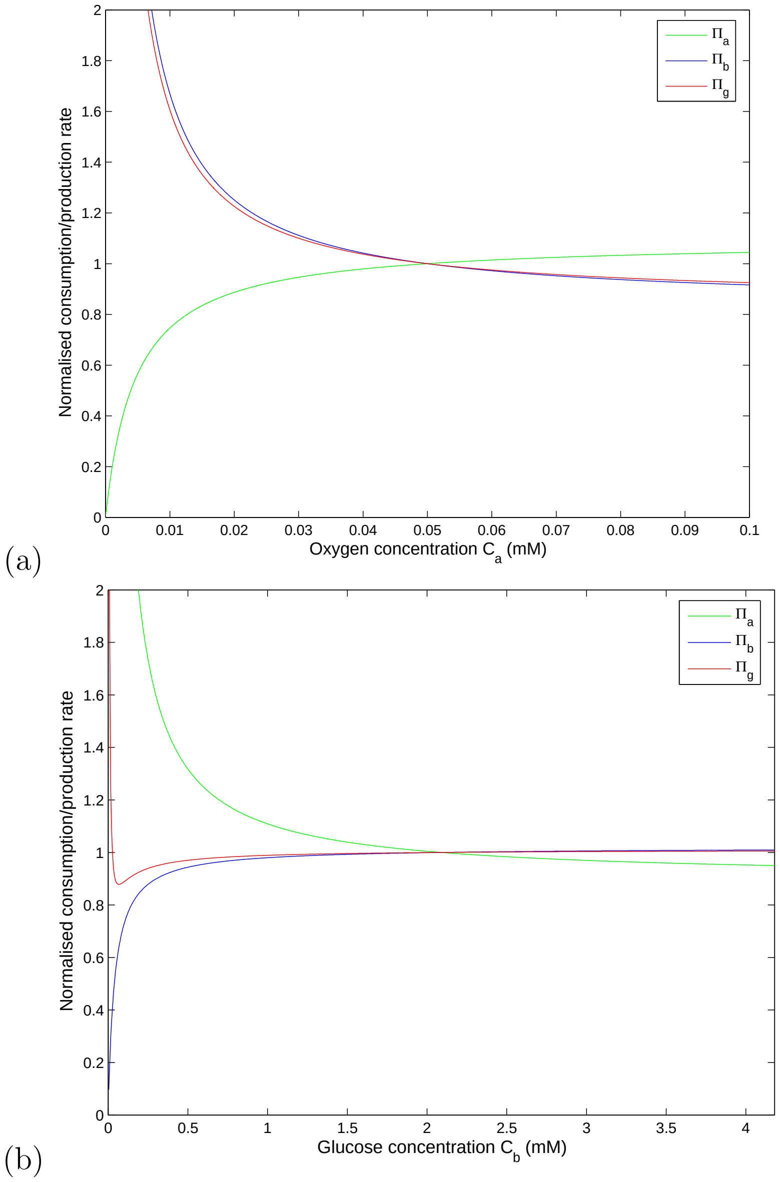

Figure 3.6: (From Eqs. (3.12)–(3.18).) Changes in oxygen consumption (Π_a), glucose consumption (Π_b) and hydrogen ion production (Π_g) as predicted by the Casciari *at al.* [19] model. (a) The Pasteur effect – glucose consumption falls as oxygen levels rise. (b) The Crabtree effect – oxygen consumption falls as glucose levels rise. Note that the model is invalid for very low glucose levels ($C_b < 7 \times 10^{-2}$ mM). Parameter values are as in Table 3.1.

a similar, experimentally-grounded model of normal cellular metabolism, to investigate which parameter changes are necessary to produce the constitutive upregulation of glycolysis commonly seen in tumours. This point is discussed further in Section 8.2.1.

3.5 Ramanujan *et al.* (2000)

Mathematical modelling of angiogenesis has received much attention over the past two decades (see [79] for a recent review). Many of these models (e.g. [6]) have focused on the dynamics of blood vessel sprouting and branching; whilst these models produce vascular structures that qualitatively resemble those seen *in vivo*, it is difficult to quantitatively compare the results with experimental data and hence verify the models.

One of the few simple, continuous models of angiogenesis was put forward by Ramanujan *et al.* [100]. Noting that solid tumours produce both stimulators and inhibitors of angiogenesis, they propose that many of the properties of tumour vasculature, including a lack of blood vessels in the central tumour region, may be explained by the intrinsic differences in the physicochemical properties of these regulators. Whilst the authors stumble during the mathematical analysis of their model, their hypothesis is still of interest. For this reason, we reanalyse their modelling framework below.

The tumour is modelled as a sphere of radius R, residing in a medium of host tissue. These different tissues produce multiple angiogenic regulators that work in concert to stimulate or inhibit angiogenesis. Let c denote the concentration of such an angiogenic factor, and for simplicity suppose that its rate of production or activation is constant. Suppose further that its rate of deactivation or degradation follows first-order kinetics.

Then, assuming the angiogenic factor is at equilibrium, we find

$$D_e \nabla^2 c - k_e c + g_e = 0, \tag{3.19}$$

where D_e is the diffusion rate (assumed constant), k_e the degradation rate and g_e the production rate. The subscript e represents environment (tumour (t) or host (h) tissue) – the factor may diffuse, degrade and be produced at different rates in the tumour and host tissue.

At this point the paper provides an incorrect solution to Eq. (3.19), which we rectify here. Let $c_\infty = \lim_{r\to\infty} c(r)$ denote the concentration of the factor in tumour-free, host tissue, which we assume to be non-zero. Then, in non-dimensional form, Eq. (3.19) becomes

$$\begin{aligned} \nabla_\eta^2 \theta - \kappa_t^2 \theta + \gamma = 0 \qquad & 0 < \eta \leq 1, \\ \nabla_\eta^2 \theta - \kappa_h^2 (\theta - 1) = 0 \qquad & 1 \leq \eta, \end{aligned} \tag{3.20}$$

where

$$\eta = \frac{r}{R}, \quad \theta = \frac{c}{c_\infty}, \quad \kappa_t = R\sqrt{\frac{k_t}{D_t}}, \quad \kappa_h = R\sqrt{\frac{k_h}{D_h}}, \quad \gamma = \frac{g_t R^2}{c_\infty D_t}. \tag{3.21}$$

Assuming that θ and its derivative are continuous at $\eta = 1$, Eq. (3.20) has solution

$$\theta(\eta) = \begin{cases} A\eta^{-1}\sinh(\kappa_t \eta) + \gamma/\kappa_t^2 & 0 < \eta \leq 1, \\ B\eta^{-1} e^{-k_h \eta} + 1 & 1 \leq \eta. \end{cases} \tag{3.22}$$

where

$$A = \frac{(\kappa_t^2 - \gamma)(1 + \kappa_h)}{\kappa_t^2(\kappa_h \sinh\kappa_t + \kappa_t \cosh\kappa_t)}, \quad B = \frac{e^{\kappa_h}(\kappa_t^2 - \gamma)(\sinh\kappa_t - \kappa_t\cosh\kappa_t)}{\kappa_t^2(\kappa_h \sinh\kappa_t + \kappa_t\cosh\kappa_t)}. \tag{3.23}$$

Consider now the interaction between two angiogenic factors, one pro-angiogenic θ^+ and one anti-angiogenic θ^-. The ratio θ^+/θ^- represents the local balance between these factors, and thus the local angiogenic tendency. The key point is that their limit, $(\theta^+/\theta^-)\mid_\infty = 1$, defines the reference condition for stable vascularisation expected in tumour-free host tissue. Whenever $\theta^+/\theta^- > 1$, angiogenesis is stimulated; elsewhere, angiogenesis is suppressed. Through this, we can circumvent the difficulty in assigning effectiveness parameters to the factors.

It remains to define the six dimensionless parameters $\kappa_t^\pm$, $\gamma^\pm$ and $\kappa_h^\pm$. Parameter estimates are based on those given in Ramanujan *et al.*, but it should be noted with caution that, in that paper, the dimensionless values do not tally with the corresponding dimensional estimates given. Typical concentration profiles for the angiogenesis stimulators and inhibitors are presented in Fig. 3.7 (a). In (b), we see that central regions of the tumour experience an anti-angiogenic effect ($\theta^+ < \theta^-$). Ultimately, this area will become under-perfused leading, in turn, to central necrosis. Towards the tumour periphery, this behaviour reverses ($\theta^+ > \theta^-$), with stimulation of angiogenesis continuing well into the host tissue. Thus angiogenic factors produced in the tumour will directly influence the adjacent host tissue.

The parameter values within the model are difficult to quantify and, moreover, are likely to vary widely amongst tumour types. Hence, in Fig. 3.8 we examine how parameter changes affect system dynamics. Angiogenesis stimulation within the tumour may be classified as (a) full suppression of angiogenesis (corresponding to dormancy); (b) full stimulation of angiogenesis (progression); or (c) central suppression of angiogenesis (as in Fig. 3.7). In Fig. 3.8 (a) and (b) we see that central suppression requires a careful balance between the parameters, or one factor will dominate within the tumour. By contrast, Fig. 3.8 (c) demonstrates that small changes in κ_h^+ or κ_h^- are insufficient to induce full

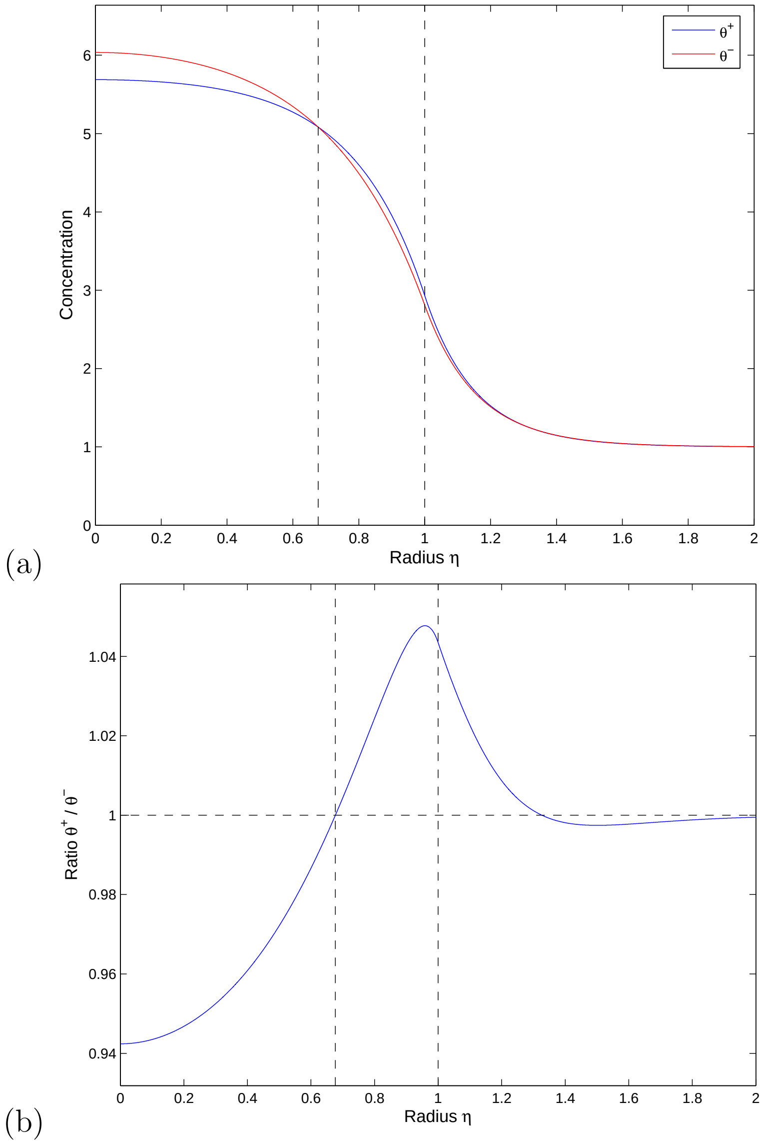

Figure 3.7: (From Eq. (3.22).) (a) Normalised concentration profiles for angiogenesis promoters (θ^+) and inhibitors (θ^-) in tumour ($\eta \leq 1$) and surrounding host ($\eta \geq 1$) tissue. (b) Concentration ratio profile with a crossover from net angiogenesis inhibition to stimulation at $\eta = 0.68$. Parameter values used are $\kappa_t^+ = 5.4$, $\kappa_t^- = 4.1$, $\gamma^+ = 170$, $\gamma^- = 110$, $\kappa_h^+ = 5.6$ and $\kappa_h^- = 5.4$.

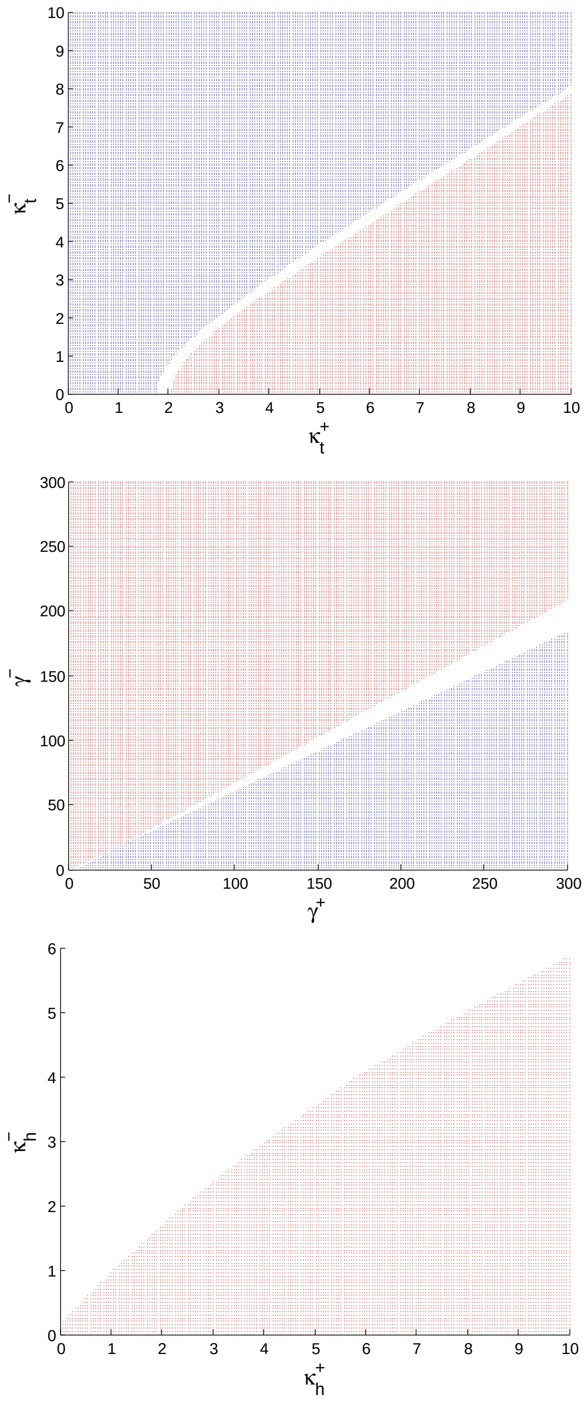

(a)

(b)

(c)

Figure 3.8: The effects of changing (a) degradation rate in tumour tissue κ_t, (b) production rate γ and (c) degradation rate in host tissue κ_h on the extent of angiogenesis stimulation. The tumour may experience ● full suppression, ○ central suppression, or ● full angiogenesis. Base parameter values used are as in Fig. 3.7.

stimulation of angiogenesis in the system.

Whilst slightly flawed, the paper by Ramanujan *et al.* provides a novel approach to theoretical angiogenesis modelling.

3.6 Summary

Mathematical approaches to the study of tumour development have a long history, dating back to the early work of diffusion in tissues [57, 72, 113]. The majority of mathematical models have appeared in the literature since 1990, though many of these have extended the basic frameworks developed by investigators such as Greenspan in previous decades. The astonishing variety of theoretical approaches used attests to the complexity of the biological and physiological processes underlying tumour development. It has become clear that gaps in our understanding of these processes may only be filled through continued close collaborations between theoreticians and experimentalists. In this way, the pathway from model hypothesis and parameterisation to testing of model predictions will become more structured and rigorous.

In this chapter, we have reviewed a small selection of diverse models. Each of the models presented here has been chosen for its simplistic nature; whilst such simple models cannot hope to fully capture the diverse behaviour observed in tumour development, they benefit from relying on a relatively small parameter space. In contrast to more detailed approaches, most of the parameters are readily obtained from the literature.

The models presented and implemented here may also be considered as distinct ‘modules’, each describing a different aspect of tumour growth. These well-parameterised models may then be brought together to produce a more detailed model, describing multiple factors. For example, it is simple to imagine modifying Greenspan's tumour growth framework to include Gatenby and Gawlinski's acid-mediated invasion. A more realistic (non-constant) acid production rate could then be included through incorporating a model of tumour metabolism, such as that described in Casciari *et al.* Finally, the model could be modified to include vasculature for nutrient supply and waste removal. This vasculature could adapt to the balance of pro-angiogenic and anti-angiogenic factors as in Ramanujan *et al.* We shall address some of these approaches in the forthcoming chapters.

Chapter 4

Metabolic changes during carcinogenesis

4.1 Introduction

The phenotypic traits of malignant cancers arise as a result of environmental selection pressures during carcinogenesis [10]. Hence it is important to understand the physical environment of early pre-malignant lesions. Carcinomas *in situ* are often characterised as highly vascularised. This is misleading, however, as whilst they may have a vascular stroma (external connective tissue), the tumour cells are actually physically separated from their blood supply by a thin basement membrane until this membrane is breached by an invasive cell. Therefore, carcinogenesis and the development of the malignant phenotype actually occur in an avascular environment, whereby substrates must diffuse across the basement membrane and through layers of tumour cells to be metabolised. This anatomy places consistent and significant boundary conditions on the biology of carcinogenesis.

A model for the key cell–environment interactions that we propose occur during carcinogenesis is shown in Fig. 4.1. This model, first proposed by Gatenby and Gillies [45], was discussed in Section 2.4, but we reiterate the main points here. Initial proliferation in premalignant lesions carries cells into the lumen, away from the basement membrane, and, therefore, away from their blood supply. This steadily increases the distance that substrate must diffuse between the vessels and the intraluminal tumour cells and results in regions of hypoxia but near normal glucose concentrations. This initiates an evolutionary sequence consisting of adaptation to hypoxia by upregulation of glycolysis, acidification of the environment due to anaerobic respiration of glucose, and then cellular adaptation to acid-induced cellular toxicity. The phenotype that emerges from this sequence has a powerful adaptive advantage because it creates an environment (due to increased glycolysis) that is toxic to its competitors but relatively harmless to itself. This adaptive advantage may be sufficient to allow unconstrained proliferation and, thus, be a critical component in the transition from a premalignant tumour to an invasive cancer.

In vivo experimental verification of the hypothesis that the final stages of carcinogenesis are driven by cellular adaptation to hypoxia and acidosis is difficult, as measurement of the evolutionary pressures acting on cells is not possible. To test the feasibility of the theoretical model of Gatenby and Gillies, we frame the hypothesis using mathematical methods that examine somatic evolution of premalignant cells within the constraints of ductal anatomy. This allows us to test the proposed sequence of environmental changes and cellular adaptations *in silico*. We use evolutionary models of carcinogenesis that explicitly include spatial parameters to accommodate the geometry of early tumour development, requiring the application of a hybrid cellular automaton approach [5, 92]. The key advantage of this technique is that it allows cells to be treated as discrete individ-

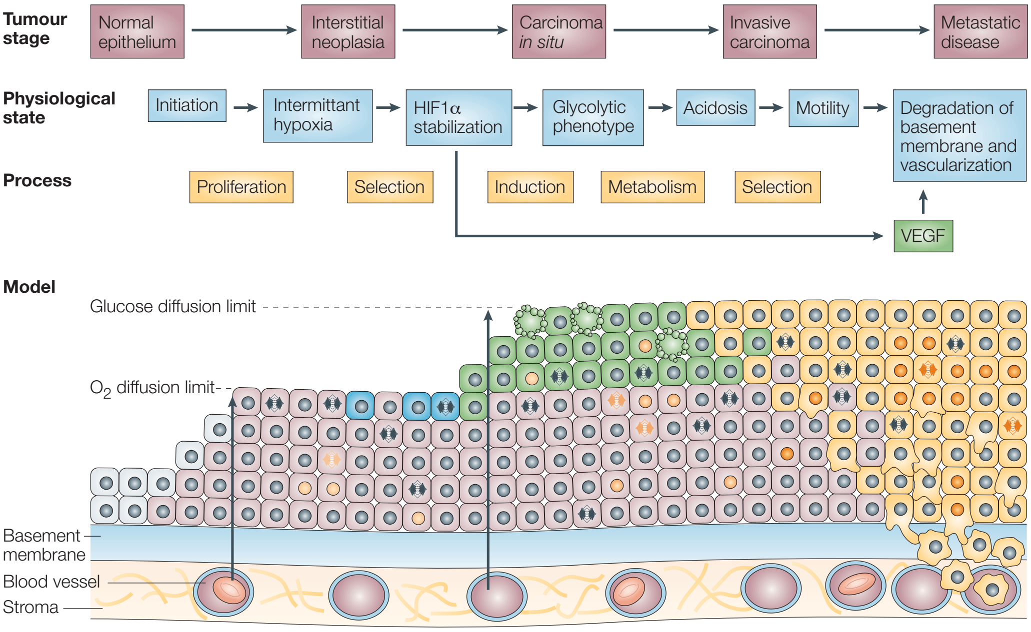

Figure 4.1: Model for cell-environment interactions during carcinogenesis, giving the stages of tumour growth and their associated physiological states. Shown are normal epithelial (grey), hyperplastic (pink), hypoxic (blue), glycolytic (green) and motile (yellow) cells. Reproduced with permission from Nature Reviews Cancer [45] © 2004 Macmillan Magazines Ltd.

uals, enabling cellular processes such as proliferation, death, adaptation and metabolite consumption/production to be modelled at the individual cell level. However, the automaton is described as hybrid because the metabolite distributions, specifically the oxygen, glucose and H^+ concentrations, are allowed to form a continuous field across the cells.

4.2 Model development

A hybrid cellular automaton model is used to simulate carcinogenesis. This two-dimensional model is composed of an $M \times N$ array of automaton elements with a specific rule-set governing their evolution, as well as oxygen, glucose and H^+ fields, each satisfying reaction-diffusion equations. A two-dimensional automaton is used as we focus on growth away from the basement membrane, rather than along the duct. Each automaton element corresponds to either a cell or a vacant space. Tumour cell diameter can be highly variable, ranging from 10 to $100\,\mu$m [85], depending on the specific tumour type under consideration. Here we assume each automaton element, and hence each tumour cell, has constant physical size $\Delta \times \Delta$, where $\Delta = 25\,\mu$m.

In the model we reflect the avascular geometry of premalignant epithelia by assuming that one edge of the array represents the basement membrane. The array (i, j) is labelled so that $i = 0$ corresponds to the basement membrane. Beyond this membrane we assume the stroma is sufficiently well-vascularised that the metabolites remain at their normal extracellular concentrations.

To investigate the hypothesis presented in Fig. 4.1, we consider the selective pressures placed on a number of different possible tumour phenotypes. Initially, the automaton consists of a layer of a normal epithelial tissue. We assume it to be a simple epithelium i.e. the cells grow in a monolayer along the basement membrane. Then the initial array consists of normal cells at $(1, j)$ and is vacant elsewhere. As well as proliferation and death, we assume that these cells may randomly undergo three possible heritable changes, either through mutations or epigenetic changes such as alterations in the methylation patterns of promoters. The cells may become:

- hyperplastic, allowing growth away from the basement membrane;
- glycolytic, increasing their rate of glucose uptake and utilisation;
- acid-resistant, requiring a lower extracellular pH to induce toxicity.

These three changes give rise to eight different phenotype combinations, and thus eight competing cellular populations. The timescales for induction of the three heritable changes during carcinogenesis will give insight as to their relative importance.

The model development is set out in three sections below. In the first section, we create a model of cellular glucose and oxygen consumption, and ATP and hydrogen ion production. This model of metabolism is then used in the second section to determine the extracellular glucose, oxygen and hydrogen ion profiles for a given cellular distribution. Finally, in the third section, we define the rules that govern automaton evolution at each generation in response to local metabolite levels.

4.2.1 Cellular metabolism

We first define a simple model of cellular glucose metabolism. Under normal physiological conditions, human cells rely on aerobic respiration to produce their energy. Each glucose molecule reacts with six oxygen molecules to produce carbon dioxide and ATP. This reaction may be caricatured by

$$\mathrm{glucose} + 6\,\mathrm{O_2} \longrightarrow 6\,\mathrm{CO_2} + \mathrm{n_A}\,\mathrm{ATP}, \tag{4.1}$$

where n_A denotes the number of ATP molecules produced during complete oxidation of glucose. Here we assume $n_A = 36$, though this value may vary slightly depending on the specific cell type under consideration.

During periods of hypoxia, cells revert to the less efficient anaerobic metabolism, producing two molecules of lactic acid per glucose molecule

$$\mathrm{glucose} \longrightarrow 2\,\mathrm{lactic\,acid} + 2\,\mathrm{ATP}. \tag{4.2}$$

Suppose the cell consumes glucose and oxygen at rates Φ_G and Φ_C respectively, and that all of the consumed glucose and oxygen is used to generate ATP under the two processes outlined above. This is a reasonable assumption, as the primary role of cellular glucose and oxygen is to generate energy via ATP. Now, from Eq. (4.1), we are assuming $\Phi_G \geq \Phi_C/6$. If this condition is satisfied, we may calculate the rates of ATP production Φ_A and lactic acid production Φ_L from Eqs. (4.1) and (4.2)

$$\Phi_A = \frac{n_A \Phi_C}{6} + 2\Big(\Phi_G - \frac{\Phi_C}{6}\Big), \tag{4.3}$$

$$\Phi_L = 2\Big(\Phi_G - \frac{\Phi_C}{6}\Big). \tag{4.4}$$

The lactic acid produced by the cell partially disassociates into H^+ and lactate. These H^+ ions lower the pH of the extracellular space, inducing cellular toxicity. The rate of cellular H^+ production Φ_H is taken to be proportional to the rate of lactic acid production, $\Phi_H = k_H \Phi_L$, for some $k_H < 1$. We return to discuss this assumption of simple, linear dynamics at the end of Section 4.2. Note that the aerobic pathway also contributes to cellular acid production through hydration of CO_2. However, this contribution is small – for each mole of ATP synthesised, anaerobic metabolism produces one mole of lactic acid, whilst aerobic metabolism produces only 1/6 mole of CO_2. As such we ignore this term, considering only the acid production in excess of the normal rate.

It remains to define the rates of cellular glucose and oxygen consumption Φ_G and Φ_C respectively. Whilst complex empirical functional forms for these rates are available [20], here we assume that the rates follow simpler first-order dynamics

$$\Phi_G = \begin{cases} k_N G & \text{in a normal cell,} \\ k_T G & \text{in a glycolytic cell,} \end{cases} \tag{4.5}$$

$$\Phi_C = k_C C, \tag{4.6}$$

where G and C denote the extracellular concentrations of glucose and oxygen respectively, and $k_T > k_N$. Note that we assume that tumour cells do not significantly alter their rate of oxygen consumption during carcinogenesis, consistent with experimental observations [99].

We non-dimensionalise Eqs. (4.3) – (4.6) to reduce the size of the parameter space. Let G_X and C_X denote the normal extracellular concentrations of glucose and oxygen, and suppose that under normal conditions, normal cells rely on aerobic respiration alone to produce energy. Then $k_C C_X = 6k_N G_X$ and

$$\phi_g = \begin{cases} g & \text{in a normal cell,} \\ kg & \text{in a glycolytic cell,} \end{cases} \tag{4.7}$$

$$\phi_c = c, \tag{4.8}$$

$$\phi_a = c + n(\phi_g - c), \tag{4.9}$$

$$\phi_h = \phi_g - c, \tag{4.10}$$

subject to the condition $\phi_g \geq c$, where

$$\begin{gathered} g = \frac{G}{G_X},\ c = \frac{C}{C_X},\ \phi_g = \frac{\Phi_G}{k_N G_X},\ \phi_c = \frac{\Phi_C}{k_C C_X}, \\ \phi_a = \frac{\Phi_A}{n_A k_N G_X},\ \phi_h = \frac{\Phi_H}{2k_H k_N G_X},\ n = \frac{2}{n_A},\ k = \frac{k_T}{k_N}. \end{gathered} \tag{4.11}$$

The non-dimensionalised model of cellular respiration relies on two parameters: $n = 1/18$ and k. Given ranges $10^{-6}\,\mathrm{s}^{-1} < k_N < 5 \times 10^{-4}\,\mathrm{s}^{-1}$ and $10^{-5}\,\mathrm{s}^{-1} < k_T < 10^{-3}\,\mathrm{s}^{-1}$ [63] for the rates of glucose consumption by normal and tumour cells respectively, we assume $1 < k < 10^3$, i.e. that glycolytic cells may increase their glucose consumption by up to three orders of magnitude.

During the first stage of carcinogenesis, the dominant growth constraints involve cellular interactions with the extracellular matrix and other cells. Once these social constraints have been overcome, the dominant growth constraint becomes limited substrate availability, and thus increased ATP production confers a competitive advantage. From Eqs. (4.7) – (4.10), we see that within our model, glycolytic cells always produce more ATP than their normal counterparts. However, this ATP is produced very inefficiently (in terms of glucose uptake) and the benefits of their transformed metabolism are only seen when oxygen supply is low. As a quantitative example, consider the case $k = 10$. The model predicts that, under normoxic ($c = 1$) and normoglycaemic ($g = 1$) conditions, normal cells produce ATP at rate 1 non-dimensional unit, whilst their glycolytic counterparts produce ATP at rate 1.5; despite the tenfold increase in glucose uptake, under normal conditions glycolytic cells have only a small proliferative advantage. However, under anoxic ($c = 0$) and normoglycaemic conditions normal cells produce ATP at a rate approximately equal to 0.06, whilst glycolytic cells produce ATP at a rate approximately equal to 0.6. Thus we see that glycolytic cells are much better suited to adapt to periods of low oxygen supply.

Differences between the two cell types are also seen in H^+ production. Normal cells only rely on glycolysis, thus producing acid, when oxygen supply is low. However, glycolytic cells produce H^+ at a high rate, and thus acidify the extracellular space, irrespective of the oxygen levels. Continuing with the example $k = 10$ above, under normoxic conditions normal cells produce H^+ at rate 0, whilst under anoxic conditions they are produced at rate 1. In contrast, the glycolytic cells produce H^+ at rates 9 and 10 under normoxic and anoxic conditions respectively.

4.2.2 Metabolite profiles

Having defined a model of cellular respiration, we are now in a position to determine the metabolite distributions around the cells. After each automaton generation, the known rates of metabolite consumption and production for each cell are used to calculate the corresponding metabolite profiles. Consider first the extracellular concentration of glucose, G. Note that the glucose diffusion time-scale (∼minutes) is much shorter than the cellular proliferation timescale (∼days), and thus we may assume that G is in diffusive equilibrium at all times. Then we have

$$D_G \nabla^2 G - \Phi_G = 0, \tag{4.12}$$

where D_G is the (assumed constant) glucose diffusion coefficient. We non-dimensionalise Eq. (4.12), taking cell diameter as our length scale. Using Eq. (4.11),

$$d_g^2 \, \nabla_\xi^2 \, g - \phi_g = 0, \tag{4.13}$$

where $\xi = x/\Delta$ and $d_g = \sqrt{D_G/k_N \Delta^2}$. Given $D_G = 5 \times 10^{-6}\,\mathrm{cm}^2\,\mathrm{s}^{-1}$ [54] and taking $k_N = 5 \times 10^{-5}\,\mathrm{s}^{-1}$, we find $d_g = 1.3 \times 10^2$. In a spatially homogeneous system of normal cells, $d_g \log 2 \approx 90$ represents the number of cells away from the basement membrane at which the glucose concentration drops to half its normal level. In a system of glycolytic cells, where glucose is consumed at a higher rate, this distance falls to $d_g \log 2/\sqrt{k}$.

Eq. (4.13) is solved using a finite-difference approximation on the square grid

$$g_{i+1,j} + g_{i-1,j} + g_{i,j+1} + g_{i,j-1} - (4 + \delta_{i,j}) g_{i,j} = 0, \tag{4.14}$$

where $g_{i,j}$ refers to the glucose level of the i-jth automaton element and $\delta_{i,j}$ depends on the element's occupancy

$$\delta_{i,j} = \begin{cases} 0 & \text{in a vacant cell,} \\ 1/d_g^2 & \text{in a normal cell,} \\ k/d_g^2 & \text{in a glycolytic cell.} \end{cases} \tag{4.15}$$

As boundary conditions, we assume that the glucose level is fixed at its normal level $g = 1$ at the basement membrane (as the stroma is well-vascularised), zero flux at the edge furthest from the membrane (as there are no sources or sinks of glucose beyond this point), and periodic boundary conditions at the other two edges. Periodic boundary conditions are used as the cross-sectional view of a duct is approximately circular, and hence the edges of our array will adjoin. Using the notation of Eq. (4.14), the boundary conditions may be written as

$$g_{0,j} = 1, \quad g_{M+1,j} = g_{M,j} \qquad \forall j = 1, \ldots, N,$$

$$g_{i,0} = g_{i,N}, \quad g_{i,N+1} = g_{i,1} \qquad \forall i = 1, \ldots, M. \tag{4.16}$$

Eq. (4.14) holds $\forall i = 1, \ldots, M$ and $\forall j = 1, \ldots, N$ and is thus representative of a system of $M \times N$ linear algebraic equations in the unknowns $g_{i,j}$. The equilibrium glucose field $g = (g_{i,j})$ may then be found through simple matrix inversion.

The oxygen distribution around the tumour is found using the same method. In non-dimensional form we have

$$d_c^2 \, \nabla_\xi^2 \, c - \phi_c = 0, \tag{4.17}$$

where $d_c = \sqrt{D_C / k_C \Delta^2}$ and D_C is the oxygen diffusion coefficient. Given $k_C = 9.41 \times 10^{-2}\,\mathrm{s}^{-1}$ [20] and $D_C = 1.46 \times 10^{-5}\,\mathrm{cm}^2\,\mathrm{s}^{-1}$ [90], we find $d_c = 5 \ll d_g$. In stark contrast to glucose, oxygen supply is very limited due to its small diffusion to consumption ratio, with areas of hypoxia developing within a few cells of the basement membrane. Note that, in order for the model to be well-defined, from Eq. (4.10) we require $\phi_g \geq c$ at each cell, for which it is sufficient that $g \geq c$ everywhere. This holds if $k \leq d_g^2 / d_c^2 \approx 700$ and as such we restrict our attention here to the parameter range $1 < k \leq 500$.

The equilibrium oxygen field c is found from Eq. (4.17) using the same technique as for glucose. Having determined the glucose and oxygen fields, we know their rates of consumption, ϕ_g and ϕ_c, for each individual cell. Then, from (4.10), we may calculate the rate of cellular H^+ production, ϕ_h. Unlike glucose and oxygen, H^+ ions do not follow simple (Fickian) diffusion, as this would lead to charge separation. Rather, they diffuse in association with mobile buffering species such as bicarbonate, phosphate, or amino acids [104]. However, their movement may be approximated by simple diffusion, with appropriate modification of the diffusion coefficient. Thus the H^+ distribution, h, is defined by

$$\nabla_\xi^2 h + \phi_h = 0, \tag{4.18}$$

where $h = (H - H_X)/H_0$ and $H_0 = 2k_H k_N G_X \Delta^2/D_H$. Here the variable H denotes the extracellular concentration of H^+, $H_X \equiv$ pH 7.25 the normal level and D_H the effective H^+ diffusion coefficient. This specific non-dimensionalisation is chosen to remove all parameters from (4.18). Given parameter values $D_H = 1.08 \times 10^{-5}$ cm^2 s^{-1} and a maximum tumour acid production rate of 10^{-4} mM s^{-1} [92], and assuming this is equivalent to our maximum non-dimensionalised rate of $\phi_h = 500$, we may estimate $H_0 = 1.1 \times 10^{-7}$ mM.

Eq. (4.18) is solved as before using a finite-difference approximation, with the difference in this case that $h = 0$ is the normal level at the basement membrane.

4.2.3 Cell dynamics

We now proceed to investigate how the carcinoma evolves in response to the associated distributions of glucose, oxygen and H^+ within the tissue. Initially, the automaton is composed of normal cells forming a monolayer along the basement membrane. After each generation, the resultant glucose, oxygen and H^+ fields are calculated using the methods outlined above. Each cell in the automaton is then updated (in a random order) according to the local metabolite levels. Cells may proliferate, adapt or die, and cells with different phenotypic patterns respond to the microenvironmental pressures in different ways. As such, competition is incorporated into the model: for a new population to progress and grow, it must successfully compete for space and resources with existing populations. Through randomly updating the automaton, and defining cellular death and division as stochastic processes (see Eqs. (4.19) and (4.20)), we go a long way to addressing the problems associated with synchronicity in cellular automata [126].

The rules governing the evolution of the automaton elements are as follows:

1. An element that is empty does not evolve directly. It may evolve indirectly when cell division takes place in a neighbouring cell.
2. If the amount of ATP produced by a cell ϕ_a falls below a critical threshold value, a_0, it dies, and the element becomes empty. As such, a_0 represents the level of ATP required for normal cellular maintenance. We do not allow hypoxia to directly induce cellular death within our model. Rather, hypoxia indirectly causes cell death through a reduction in ATP production. As mentioned previously, cells displaying the glycolytic phenotype produce significantly more ATP than their normal counterparts during periods of hypoxia, thus they are less susceptible to cell death via this mechanism. We assume $a_0 = 0.1$, corresponding to normal cell death occurring when oxygen levels drop below $c = 0.05$ [5].
3. The local H^+ level may also induce cellular death, with probability p_{dea}. We define this probability by

$$p_{\mathrm{dea}} = \begin{cases} h/h_N & \text{in a normal cell, if } h < h_N, \\ h/h_T & \text{in an acid-resistant cell, if } h < h_T, \\ 1 & \text{otherwise.} \end{cases} \tag{4.19}$$

   where $h_N < h_T$. Thus the probability of cell death increases with acidity, and the cell will always die if the H^+ level is greater than h_N or h_T, dependent on the cell type under consideration. These values are taken to be $h_N = 9.3 \times 10^2$ and

$h_T = 8.6 \times 10^3$ for normal and acid-resistant cells respectively, corresponding to threshold values of pH 6.8 and pH 6 [92].

4. If the cell is not attached to the basement membrane, and is not hyperplastic, it dies.

5. If the cell does not die through any of the mechanisms above, it either attempts to divide, with probability p_{div}, or becomes quiescent. The probability of division is a function of the cellular ATP production

$$p_{\text{div}} = \begin{cases} (\phi_a - a_0)/(1 - a_0) & a_0 < \phi_a < 1, \\ 1 & \phi_a \geq 1. \end{cases} \tag{4.20}$$

   Hence we assume that the probability of division is proportional to the ATP generated that is not needed for maintenance, and that the cell will always attempt to divide if the production rate is more than its normal level of 1. If the cell attempts to divide, we determine whether cell division occurs by sampling its neighbouring elements. If there is one empty space, then the cell divides, and the new cell occupies this empty space. If there is more than one empty space, the new cell goes to the element with the largest oxygen concentration (following [2]).

6. If a cell divides, each of the two daughter cells has probability p_a of randomly acquiring one of the three heritable characteristics (hyperplasia, glycolysis and acid-resistance). In order to avoid bias in the model, we assume these changes are reversible. For example, a cell displaying constitutive up-regulation of glycolysis may revert to normal glucose metabolism; if this metabolism is most appropriate for the current microenvironmental conditions, the cell will successfully compete for

resources with its neighbours. We choose $p_a = 10^{-3}$ as a base value, to reflect the fact that heritable change is a relatively rare occurrence.

It remains to define the dimensions of the automaton M and N. We take $N = 50$, corresponding to a typical ductal carcinoma of radius 200 μm. However, we leave M undefined, allowing it to dynamically increase as the carcinoma grows. Essentially the final value taken by M will represent the maximum distance from the basement membrane the cells may survive, given the limited nutrient supply and acid removal.

Throughout this model derivation, we have assumed that various processes follow simple, linear dynamics (Eqs. (4.5), (4.6), (4.19) and (4.20)). It can be argued that these assumptions are too unrealistic to represent complex biological phenomena such as these. However, these processes are poorly understood and, as a first approximation, an assumption of linearity is sufficient to capture qualitatively similar monotonic behaviour. We would not expect these assumptions to have a marked effect on the model's conclusions. Moreover, the relative simplicity of the model means that the parameter space is kept to a manageable size.

4.3 Results

We now apply the procedures outlined in the previous section. The simulations involved systematically varying the glycolytic rate k, tumour cell acidity threshold h_T and adaptation rate p_a whilst keeping other parameters constant. Multiple repetitions of the evolution of the system for each (k, h_T, p_a) triple were performed to obtain adequate statistics.

Fig. 4.2 shows the temporal evolution of a typical cellular automaton ($k = 10$, $h_T = 8.6 \times 10^3$, $p_a = 10^{-3}$), and may be compared to the model described in Fig. 4.1. Initially, normal epithelial cells (grey) line the basement membrane (Fig. 4.2 (a)). Acquisition of the hyperplastic phenotype (pink) allows growth away from the membrane towards the oxygen diffusion limit (Fig. 4.2 (b)). Beyond this point, cells cannot exist as the oxygen levels are insufficient to meet cellular ATP demands. This drives adaptation to a glycolytic phenotype (green), less reliant on oxygen for ATP production (Fig. 4.2 (c)). The increased ATP levels within glycolytic cells give a competitive advantage over the existing population, thus glycolytic cells dominate the system. Note, however, that the total number of cells within the system has decreased; the increased reliance on glycolysis has resulted in higher levels of acidity, in turn inducing cell death. Further adaptation occurs to an acid-resistant phenotype (Fig. 4.2 (d)). Increased use of glycolysis allows growth well beyond the oxygen diffusion limit, whilst the cells are more resistant to the resulting acidosis.

Fig. 4.3 shows how metabolite levels vary across the lesion at this final stage of development. Here we see growth approximately thirty cells deep from the basement membrane. Oxygen levels drop to $c = 0.02$, in comparison to their normal level of 1. In contrast, glucose levels fall to $g = 0.9$; despite the tenfold increase in consumption rate, the extracellular glucose levels are only slightly reduced. This is an important point – over the length scale of carcinogenesis, glucose supply is not a limiting factor. Rather, the cells furthest from the basement membrane are kept at equilibrium through a modest reduction in ATP production ($\phi_a = 0.5$) accompanying cellular death through a large increase in H$^+$ levels ($h = 2 \times 10^3$). In contrast to the theoretical model presented in Fig. 4.1, we find that the most likely mechanism for necrosis of cells furthest from the basement mem-

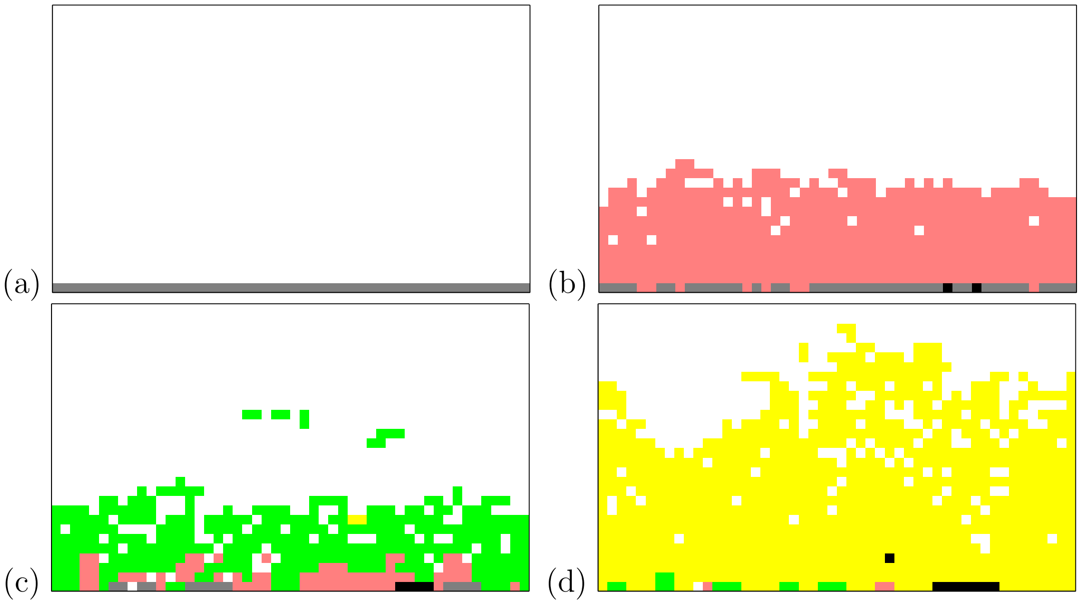

Figure 4.2: The temporal evolution of a typical cellular automaton ($k = 10$, $h_T = 8.6 \times 10^3$, $p_a = 10^{-3}$) after (a) $t = 0$, (b) $t = 100$, (c) $t = 250$ and (d) $t = 300$ generations. Shown are normal epithelial (grey), hyperplastic (pink), hyperplastic–glycolytic (green) and hyperplastic–glycolytic–acid-resistant (yellow) cells. Cells with other phenotypic patterns are shown as black.

brane is acid-induced toxicity, rather than glucose deprivation. In turn, this enhances the argument that acid-induced cellular toxicity is a major evolutionary force in the hypoxic regions of premalignant tumours. The inhibitory effect conferred by acidosis increases with distance from the basement membrane, inducing heterogeneities that may be seen in Fig. 4.2 (b)–(d).

In Fig. 4.4 the proportion of cells displaying each heritable change is shown for the automaton displayed in Fig. 4.2. The three stages of growth from normal cells acquiring, in turn, hyperplastic, glycolytic and acid-resistant phenotypes can be clearly seen. The steepness of the hyperplastic and acid-resistant curves suggests that these changes are extremely beneficial to the underlying population. The glycolytic curve is shallower as the benefits of increased ATP production are counteracted by acidosis. The order in which

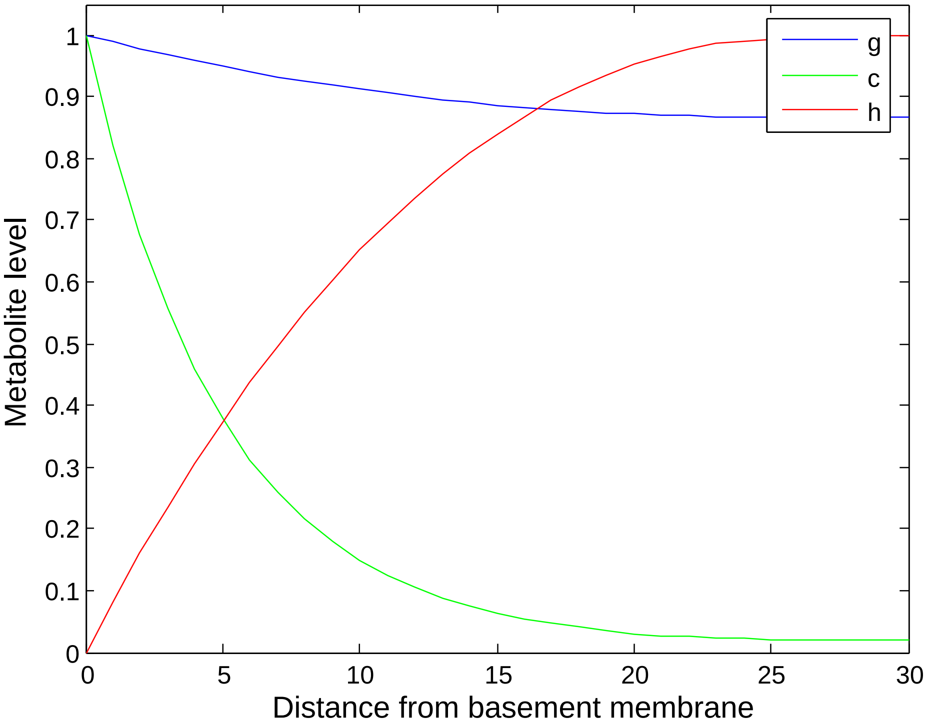

Figure 4.3: Variation in metabolite concentrations with distance from the basement membrane for the automaton generation displayed in Fig. 4.2 (d). Shown are the mean glucose (g), oxygen (c) and H^+ (h) concentrations. The H^+ profile has been scaled by its maximum value ($h \approx 2 \times 10^3$).

changes are accumulated is random; however, for a new phenotype to successfully compete with an existing population for resources it must be better suited to respond to existing microenvironmental factors. It is interesting to note that throughout the simulations performed here, the heritable changes within the dominant population are accumulated in this same order. Within our model, the underlying environmental selection parameters drive the cells to always follow this adaptive pathway – escaping in turn from the constraints of limited proliferation (hyperplasia), substrate availability (glycolysis) and waste removal (acid-resistance). The same order of progression occurs despite allowing phenotypic reversibility within our model. This is an important conceptual advance as it means mutations are not a necessary mechanism for phenotypic variation within tumour tissue; rather the model demonstrates that reversible, epigenetic changes are sufficient to drive global change.

In order to examine the effects of parameter changes on system dynamics, we define a measure of the 'fitness' of a specific parameter set. Let 'invasive' be used to describe cells displaying all three heritable changes and, for a particular automaton, let T denote the number of generations after which 95% of the cells in the system display the invasive phenotype. Thus T is representative of the amount of time taken for full carcinogenesis to occur. Now let the development rate $R = T^{-1}$, where we take $R = 0$ if $T \geq 5000$ (equivalent to approximately 20 years). Automata with a higher value of R proceed more quickly through the carcinogenesis pathway.

In Fig. 4.5 we see how the development rate R varies with changes in (a) glycolytic rate k, (b) acid-resistance h_T and (c) adaptation rate p_a. Using default parameters of $k = 10$, $h_T = 8.6 \times 10^3$ and $p_a = 10^{-3}$, the three graphs show the effects of changing one of these

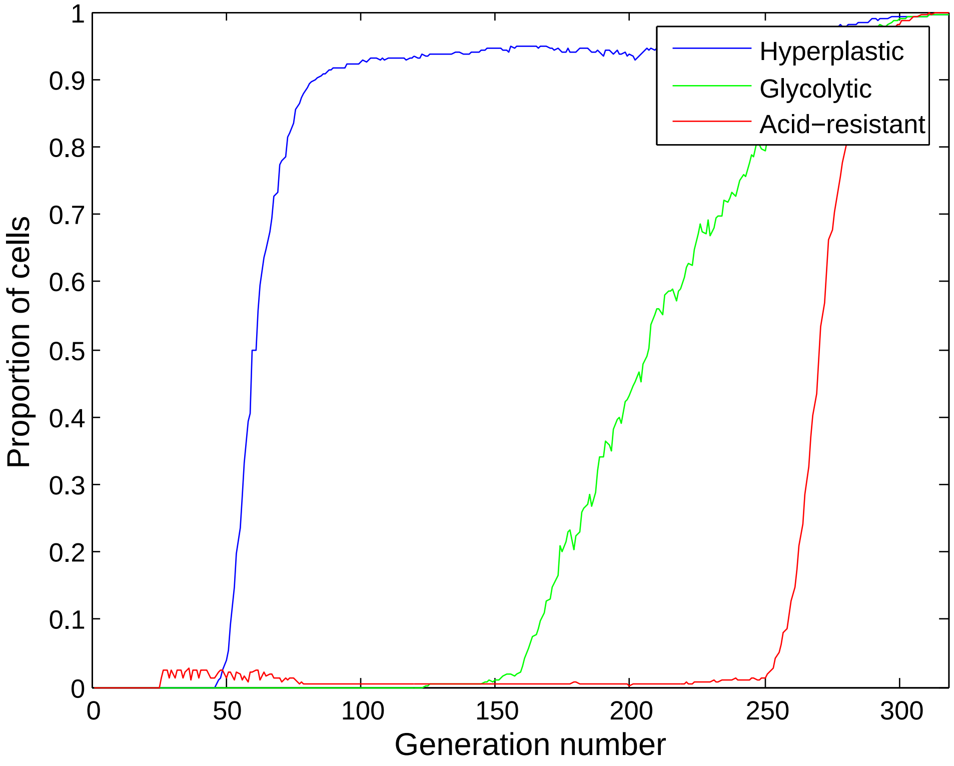

Figure 4.4: Accumulation of heritable changes over time for the automaton displayed in Fig. 4.2. Shown are the proportion of cells displaying the hyperplastic, glycolytic and acid-resistant phenotypes.

parameters whilst keeping the other two fixed at their default value. Each data point is the mean value of R calculated over fifty simulations, whilst the accompanying error bars show the standard errors of these means.

Fig. 4.5 (a) shows a sharp transition from slow development to rapid development as the glycolytic rate k is increased through a critical threshold value of $k \approx 3$. This transition occurs when the increase in ATP production and extracellular acidity, due to upregulation of glycolysis, is sufficient to give the invasive cell population a significant advantage over their untransformed counterparts. A similar bifurcation has been seen in other models looking at the role of acidity in tumour growth, whereby a transition from benign to malignant growth is seen when the cellular acid production rate increases through a critical point [41, 46, 92, 107]. Increasing k beyond 20 results in a slow monotonic decrease in the development rate. For such large values of k, acid accumulates to a degree unfavourable even to the resistant invasive cells, inducing auto-toxicity.

In Fig. 4.5 (b) we see that initially the development rate increases sharply with increasing acid-resistance, reaching a plateau at $h_T \approx 2 \times 10^3$. For large h_T, we find the benefits of increasing acid-resistance are counteracted by clumps of acid-resistant non-glycolytic cells developing near the basement membrane, withstanding the progression of the invasive phenotype. In the microenvironment near the membrane, the non-glycolytic cells produce sufficient ATP and are extremely resistant to extracellular acidity; thus their invasive, glycolytic counterparts have only a small competitive advantage.

Finally, Fig. 4.5 (c) shows that, as with the glycolytic rate k, there is a value of adaptation rate p_a at which the development rate is optimal. Increasing the adaptation rate increases the diversity of the system. This leads to an increased chance of acquiring the invasive

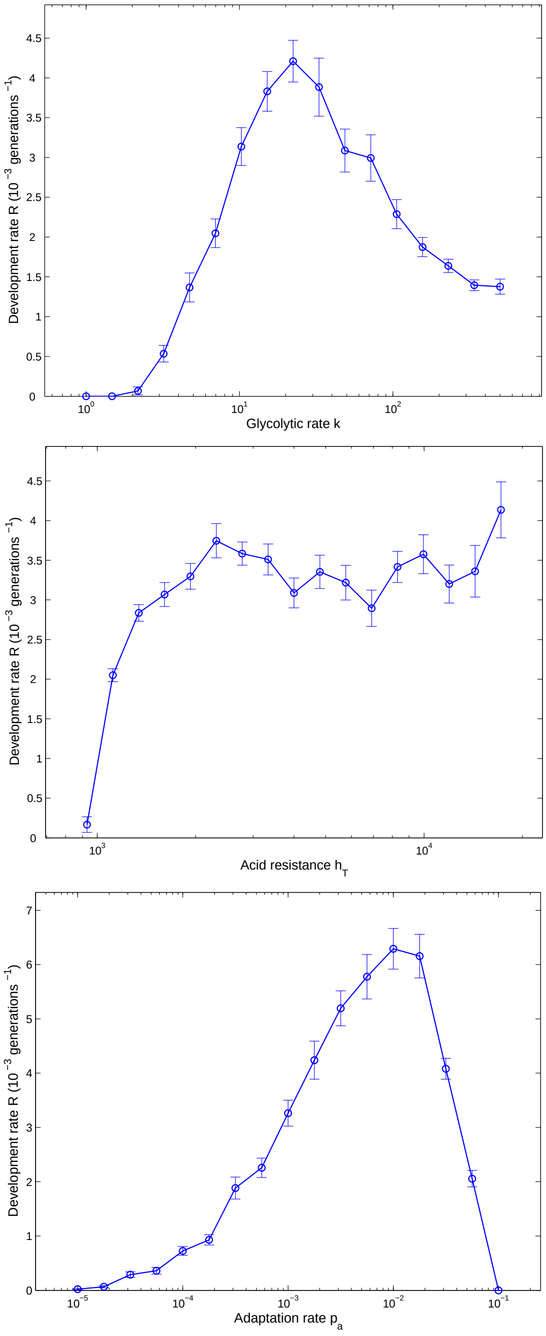

(a)

(b)

(c)

Figure 4.5: Variation in the development rate R with (a) glycolytic rate k, (b) acid-resistance h_T and (c) adaptation rate p_a. Default parameter values used are $k = 10$, $h_T = 8.6 \times 10^3$ and $p_a = 10^{-3}$. Note that k, h_T and p_a are plotted on a log-scale. Each data point is the mean value of R calculated over fifty simulations, whilst the accompanying error bars show the standard errors of these means.

phenotype, whilst reducing the dominance of the main population in the system. This balance resolves itself with the maximum development rate occurring at $p_a \approx 10^{-2}$.

4.4 Variable adaptation rates

RNA viruses are known to mutate at very high rates. The evolutionary success of RNA viruses is due to their enormous plasticity and adaptability to changing environments. This high mutation rate generates a highly heterogeneous population, known as molecular quasispecies. The quasispecies structure provides an extraordinary reservoir of variants with potentially useful phenotypes in the face of environmental change. As predicted by Eigen and Schuster's theory of quasispecies [31, 105], a critical mutation rate known as the 'error catastrophe' exists beyond which the genomic information is lost i.e. no Darwinian selection operates. Ribavirin, a common antiviral drug, exploits this property therapeutically; by its mutagenic action it drives poliovirus into an error catastrophe of replication, thereby turning a productive infection into an abortive one [25].

One hallmark of cancer cells is their underlying genetic instability – a term used to describe the occurrence of both small genetic changes such as nucleotide deletions or insertions, or larger changes such as alterations in the number of chromosomes (aneuploidy). Tumour progression benefits from genetic instability by generating cellular diversity, allowing the cells to overcome selection barriers.

Given the similarities in the quasispecies structure of cancer and RNA virus populations, we would expect a similar error catastrophe threshold to exist beyond which cancer cells cannot survive. Returning to Fig. 4.5 (c), we see this is indeed the case; as the adaptation rate p_a increases beyond a critical value ($p_a \approx 10^{-2}$) the fitness of the cells quickly drops to zero. This analysis suggests that cancers close to this threshold value will be highly susceptible to therapies directed at further increasing their mutation rate.

To investigate how adaptation rates vary during carcinogenesis, we extend the model presented in Sections 4.2–4.3 to allow this rate p_a to change dynamically. Specifically, we add a further automaton rule as follows:

7. When a cell with adaptation rate p_a divides, each of its two daughter cells has new adaptation rate p_a', where

   $$p_a' \sim U\Big((1-\sigma)p_a, (1+\sigma)p_a\Big) \tag{4.21}$$

   is drawn from a uniform distribution on the interval $\big((1-\sigma)p_a, (1+\sigma)p_a\big)$, for some $\sigma \in [0,1]$. Note that $\sigma = 0$ implies $p_a' = p_a$, and the analysis reduces to that given in the previous section.

There are two points of note about this choice of definition for p_a'. Firstly, $p_a' > 0$, as adaptation rates cannot be negative. Secondly, the daughter cell's mean adaptation rate $\mathrm{E}(p_a') = p_a$ is the same as that of the parent. As such, we introduce no bias into the system; rather, the underlying evolutionary pressures will drive changes in systemic adaptation.

The results of this extended model are presented in Fig. 4.6, showing how the adaptation rate changes during carcinogenesis over fifty simulations. Initially, each cell in the simple epithelium has adaptation rate $\bar{p}_a$, where we choose $\bar{p}_a = 10^{-4}$, an order of magnitude less than the base value taken in the previous section. Cellular adaptation then varies

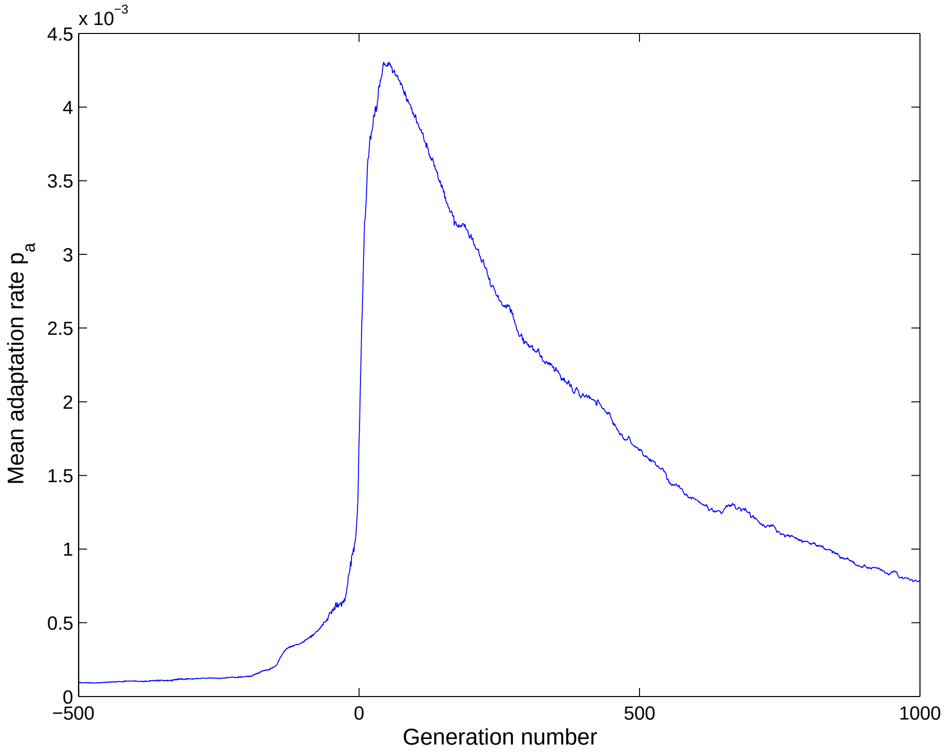

Figure 4.6: Variation in the mean adaptation rate p_a with time during carcinogenesis. The graph shows the average rates over fifty simulations, with time scaled so that generation 0 corresponds to the first appearance of the invasive phenotype. Parameter values used are $\bar{p}_a = 10^{-4}$, $\sigma = 0.25$, $k = 10$ and $h_T = 8.6 \times 10^3$.

according to Eq. (4.21). We choose $\sigma = 0.25$, so that p_a may change by up to 25% at each cellular division. Generation numbers are shifted in the figure so that time 0 corresponds to the first appearance of the invasive phenotype (hyperplastic–glycolytic–acid-resistant).

Following the appearance of the invasive phenotype, its clone cells quickly populate the lesion (see Fig. 4.2). As this cell is first to display the phenotype, it is likely to have a higher adaptation rate than its competitors. Thus, at time 0 we see a very sharp rise in the average systemic adaptation rate. Once the majority of cells within the system are of the invasive phenotype, evolutionary pressures will act against cells that adapt into other, less fit, phenotypes. As such, approximately 50 generations after the appearance of the invasive phenotype, pressures act to reduce the adaptation rate in the system.

In summary, the model predicts that during early carcinogenesis, evolutionary pressures act to favour cells with high adaptation rates. Later in the process, once cells have reached the peak of the fitness landscape, the model predicts that these pressures will act to favour cells with smaller adaptation rates.

4.5 Discussion

In this chapter we address the evolutionary dynamics in carcinogenesis that promote aerobic glycolysis in the malignant phenotype and examine the potential role of abnormal glucose metabolism in formation of invasive cancers.

Carcinogenesis is a complex multi-step process governed by the interactions of heritable phenotypic variations with continuously changing environmental selection forces. The dynamics of carcinogenesis are often summarised as somatic evolution because they appear to be formally analogous to Darwinian selection in nature. Thus defined, the common appearance of a specific phenotype within different cancer populations must be the result of environmental selection and, therefore, must confer a significant growth advantage.

Since the pioneering work of Warburg [119] nearly a century ago, experimental observations have consistently demonstrated that cancer cells, unlike their normal counterparts, utilise anaerobic pathways to metabolise glucose even in the presence of oxygen. The clinical importance of this phenotypic trait is suggested by FDG-PET imaging, which demonstrates a several-fold increased glucose uptake in the vast majority of human primary and metastatic cancers. However, in the context of the evolutionary model of carcinogenesis, the competitive advantage of altered glucose metabolism is not immediately clear since it represents a highly inefficient means of energy production and results in significant acidosis of the tumour microenvironment.

The work presented here uses a hybrid cellular automaton approach to examine the role of the microenvironment in mediating the somatic evolution of cancer cells. Utilising the fact that epithelial tumours evolve on mucosal surfaces separated from their blood supply by the intact basement membrane, we extend previous evolutionary modelling of carcinogenesis to explicitly include spatial parameters that accommodate these boundary conditions. This new modelling approach allows quantification of regional variations in the microenvironment in premalignant lesions.

We examine the hypothesis that upregulation of glycolysis represents an adaptation to hypoxia in premalignant lesions that develops as tumour cells grow into the lumen of the duct and away from their blood supply. This new phenotype, in turn, produces environmental acidosis which promotes additional adaptation to prevent acid-induced cell death. The phenotype that emerges from this sequence has a substantial proliferative advantage because it creates an environment that is toxic to its competitor but not to itself. The invasive phenotype permits penetration through the basement membrane and formation of a primary carcinoma.

Our results confirm the hypothesis that hypoxia and anoxia will be common in premalignant lesions such as DCIS or advanced colon polyps. In fact, we demonstrate that even early hyperplastic lesions will contain areas of hypoxia once tumour growth carries cells to more than a few cell layers beyond the basement membrane. Similarly, our results confirm that regional development of hypoxia will promote upregulation of anaerobic metabolism of glucose and subsequent development of extracellular acidosis. Finally, we find the acidic $\mathrm{pH_X}$ that develops from this sequence will, in some regions, result in cellular toxicity and therefore become a significant environmental selection factor that promotes resistant phenotypes.

Clearly, confirmation of the modelling results by direct measurement of regional variations in oxygen, glucose and H^+ concentrations in premalignant lesions will be difficult. However, our results are likely to be realistic since the work is based on well established biological application of reaction–diffusion models where the values of critical parameters are known. In fact, the potential for development of hypoxia within tissue was demonstrated mathematically by Krogh nearly 100 years ago [72]. The presence of hypoxia in tumour cells more than 100 to 150 microns from a blood vessel has been demonstrated experimentally by many investigators since the pioneering work by Thomlinson and Gray [29, 113]. Finally, experimental measurement of perivascular oxygen and $\mathrm{pH_X}$ gradients that both qualitatively and quantitatively resemble our modelling results have been reported by Helmlinger *et al.* [56].

The results also demonstrate possible pathways in somatic evolution that may result as cellular populations acquire new, fitter phenotypes in response to local proliferative constraints caused by variations in microenvironmental properties. This allows explicit predictions regarding regional variations in phenotype in both premalignant lesions such as DCIS and early invasive cancers. This predicted phenotypic variability should be experimentally verifiable and we are encouraged that published studies [127] have shown evidence of adaptation to hypoxia through increased expression of carbonic anhydrase IX in DCIS cells that are nearest the lumen (i.e. most distant from the basement membrane

– see Fig. 2.7 (a)).

Finally, the results suggest that tumour prevention strategies aimed at interrupting the hypoxia–glycolysis–acidosis cycle and the resulting cellular adaptations will delay or prevent transition from *in situ* to invasive cancer. For example, our results suggest that drugs that block the function of the Na^+/H^+ antiport (such as amiloride) would likely inhibit the adoption of constitutive upregulation of aerobic glycolysis.

In summary, the model supports the hypothesis that regional variations in oxygen, glucose and H^+ levels drive the final stages of somatic evolution during carcinogenesis. We propose that the phenotypic adaptations to the sequence of hypoxia–glycolysis–acidosis are necessary to form an invasive cancer. For this reason, interruption will likely delay or prevent transition from *in situ* to invasive cancer.

Chapter 5

Acidity in tumour growth and invasion

5.1 Introduction

In Section 2.4 we saw that tumour cells generally display increased anaerobic respiration, known as the glycolytic phenotype. This metabolic regime is more than an order of magnitude less efficient than its aerobic counterpart. Moreover, glycolysis produces lactic acid, causing an acidification of the extracellular space that is potentially toxic. Despite its sub-optimality, the presence of aerobic glycolysis in such a wide range of cancer populations is evidence that it must confer a significant growth advantage during somatic evolution.

Recall that tumour cells are relatively resistant to extracellular acidity due to increased Na^+/H^+ antiport activity and mutations in acid-induced apoptosis pathways. As discussed in Section 3.3, Gatenby and coworkers propose that tumour cells' increased acid secretion, coupled with their resistance to low extracellular pH, provides a simple but complete mechanism for cancer invasion. Their models show that the H^+ ions produced by tumour cells diffuse along concentration gradients into normal tissue, inducing normal cell death. The tumour edge forms a travelling wave progressing into normal tissue, preceded by another travelling wave of increased microenvironmental acidity. Significantly, their model predicts an acellular gap separating the tumour and host tissue fronts, a prediction observed in subsequent experiments.

One major flaw in both the partial differential equation [41, 42] and cellular automaton [92] models of acid-mediated invasion is their inability to capture physiologically realistic benign growth patterns (see Fig. 3.3 (b) and the discussion in Section 3.3). In this chapter we overcome this problem, through reformulating the acid-mediated invasion hypothesis within the framework devised by Greenspan [51]. Modelling this hypothesis on the macroscopic scale allows us to investigate the general tissue dynamics in both vascular and avascular tumour growth. In particular, for tumour cells displaying the glycolytic phenotype, we determine the critical parameters that cause the change, within our modelling framework, from a benign to invasive growth pattern. This in turn suggests new therapeutic regimes for counteracting this invasive growth.

5.2 Model development

Following previous models, we assume that the tumour acts as an incompressible fluid. As such, local changes in the cell population, caused by the birth or death of cells, give rise to internal pressure gradients that induce cellular motion and the expansion or contraction of the tumour colony. This expansive force is counterbalanced by cell-cell adhesion forces at the tumour periphery that maintain the tumour as a compact mass. Subsequent tumour growth is determined by the interaction between these expansive and restraining forces.

We model the tumour as a sphere and assume that spherical symmetry prevails at all times. Whilst this assumption is valid for early tumour and MCS growth, during later development tumours often become asymmetric. Moreover, it has been suggested that some measure of the irregularity of the tumour boundary may provide clinicians with useful prognostic information [24]. However, under the assumption of spherical symmetry, the model remains analytically tractable and allows us to perform analysis of the general tissue dynamics in response to acid production. Having established the validity of our assumptions, the basic model may then be reworked using a more physiologically accurate description of the tissue, for example employing finite element or cellular automaton approaches.

A schematic cross-sectional view of a tumour and its surrounding normal tissue is given in Fig. 5.1. Let R_M denote the tumour (<u>m</u>alignant tissue) radius and R_D the radius of the necrotic core (<u>d</u>ead tissue). We assume that $R_D < R < R_M$ is a viable region where the proliferating tumour cells exist in a spatially homogeneous state at their carrying capacity K_M. We further assume $R < R_D$ is a necrotic region, containing no viable cells, and that the necrotic debris continually disintegrates into simpler compounds that are freely permeable through cell membranes. The cell volume lost in this way is replaced by cells pushed inward through adhesion or surface tension. Note that, at this point, we are neglecting the effects of quiescent (non-proliferating) tumour tissue. We return to this in Section 5.3 and Chapter 6.

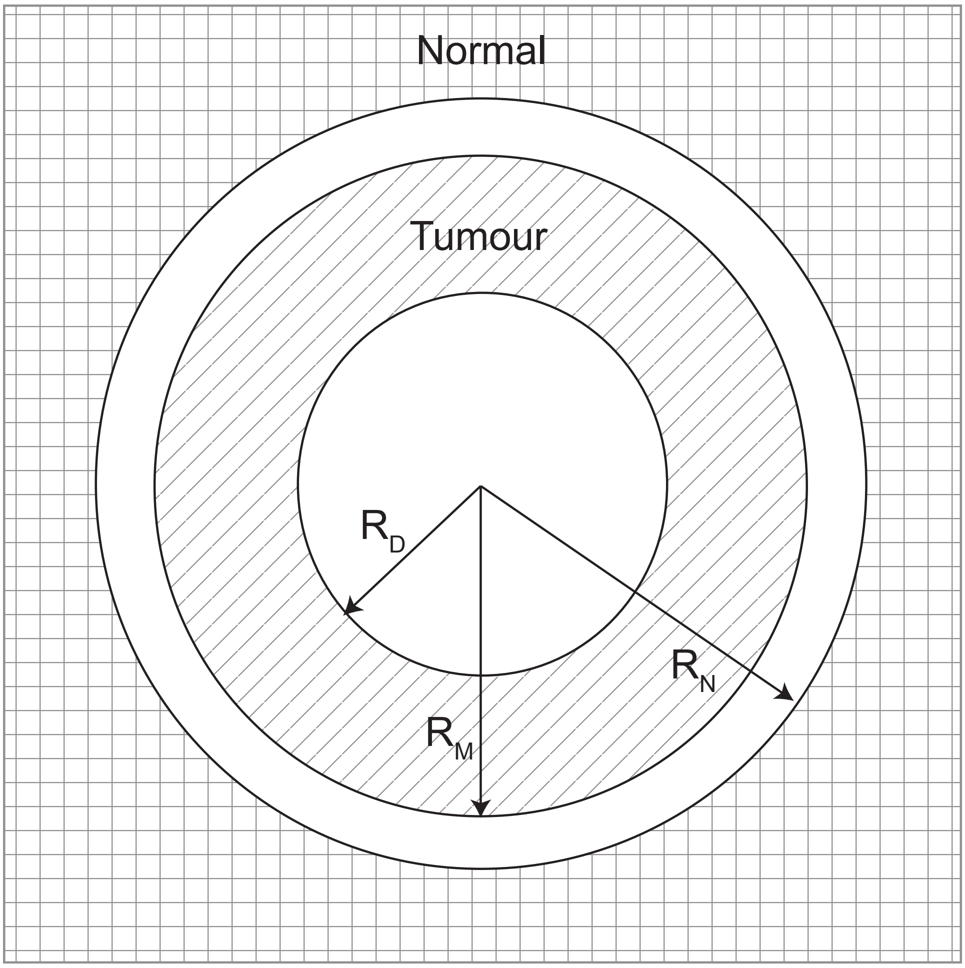

Figure 5.1: Schematic cross-section of a tumour and its surrounding tissue showing the central necrotic core, $R < R_D$, the layer of proliferating tumour cells $R_D < R < R_M$, the acellular gap separating normal and tumour cell fronts $R_M < R < R_N$, and the normal cells $R_N < R$.

5.2.1 Acid profile

We consider first the distribution of acid generated by the tumour. Let H denote the extracellular concentration of excess hydrogen ions. Here *excess* means above the normal level of $10^{-7.25}$ M = pH 7.25. It is assumed that there is a sharp acid threshold concentration H_M above which tumour cells cannot survive. Similarly, normal cells die when this concentration H rises above H_N. We assume $H_N \ll H_M$ to represent the relative resistance of tumour cells to extracellular acidity. As such, metabolically-produced acid can act both as a promoter or inhibitor of tumour growth. Diffusing into the normal tissue, the acid causes normal cell death which in turn allows the tumour to expand. Conversely, if acid is not removed from within the tumour sufficiently quickly, tumour cell death will occur. The interplay between these two mechanisms forms the heart of the model described below.

We assume that the evolution of H can be described by a reaction-diffusion equation

$$\frac{\partial H}{\partial t} = F_H + D_H \nabla^2 H \tag{5.1}$$

where D_H is the (assumed constant) acid diffusion coefficient and F_H represents the combined rate of acid production and removal from the system.

Acid is produced by tumour cells as a result of their increased reliance on glycolysis and we assume that this occurs at a constant rate r_H per unit volume. The primary mode for removal of acid from the system is through blood vessels and we assume that this occurs at a rate r_V proportional to the local acid concentration. Note that the acid diffusion timescale ($\sim$ minutes) is much shorter than the tumour growth timescale ($\sim$ days). Hence, as the tumour grows, the acid quickly redistributes and reaches equilibrium. Following previous work, we assume that H is in diffusive equilibrium at all times and set $\partial H/\partial t = 0$ in the acid reaction–diffusion equation. Under these assumptions, and noting spherical symmetry, Eq. (5.1) becomes

$$0 = r_H M - r_V V H + \frac{D_H}{R^2}\frac{d}{dR}(R^2\frac{dH}{dR}) \tag{5.2}$$

where M denotes the viable tumour cell density and V the vascular density.

We consider separately the acid profiles generated by vascular and avascular tumours. In the avascular case, we define $V = 0$ for $R < R_M$ and $V = V_N$ elsewhere, i.e. there is no vasculature within the tumour and the vasculature exists homogeneously at its normal level outside the tumour. Note we also assume that the acellular gap $R_M < R < R_N$ contains no tumour or normal tissue, but does remain vascularised. This is because endothelial tissue is extremely resistant to acid-induced toxicity [92]. Taking tumour cell density M to be constant (K_M) within the viable region $R_D < R < R_M$, and further taking $p = \sqrt{r_V V_N/D_H}$ and $H_0 = r_H K_M/r_V V_N$, we may non-dimensionalise Eq. (5.2) with $r = pR$ and $h = H/H_0$ to obtain

$$r^2 h'' + 2rh' = \begin{cases} 0 & 0 < r < r_D \\ -r^2 & r_D < r < r_M \\ r^2 h & r_M < r \end{cases} \tag{5.3}$$

where the primes denote the derivative with respect to r.

Previous models of tumour growth have made the assumption that the nutrients and other factors determining tumour growth are constant outside the tumour tissue, i.e. for any growth factor g, $g(r) = g_\infty$ for $r > r_M$. In the case of acid, however, this would be inconsistent with the data of Martin and Jain [80]. Reporting *in vivo* extracellular pH profiles for VX2 rabbit carcinoma, they demonstrate a smooth pH gradient extending from the tumour edge into the peritumoural normal tissue. Instead, we assume here that $\lim_{r\to\infty} h(r) = 0$, i.e. that there is no excess acidity a long distance from the tumour. Assuming further that h and its derivative are continuous at r_D and r_M, and that $\lim_{r\to 0} h(r)$ is finite, Eq. (5.3) has solution

$$h_a(r) = \begin{cases} k_1 & 0 < r < r_D \\ k_2 - k_3\frac{1}{r} - \frac{1}{6}r^2 & r_D < r < r_M \\ k_4\frac{1}{r}e^{-r} & r_M < r \end{cases} \tag{5.4}$$

where the constants k_i are given by

$$\begin{aligned} k_1 &= \frac{2r_D^3 + 3r_M^2 + r_M^3}{6(r_M+1)} - \frac{r_D^2}{2} \\ k_2 &= \frac{2r_D^3 + 3r_M^2 + r_M^3}{6(r_M+1)} \\ k_3 &= \frac{r_D^3}{3} \\ k_4 &= \frac{e^{r_M}(r_M^3 - r_D^3)}{3(r_M+1)} \ . \end{aligned} \tag{5.5}$$

Returning to Eq. (5.2), we also calculate the predicted acid profile for a vascularised tumour. In this case we define $V = 0$ for $r < r_D$ and $V = V_N$ elsewhere, i.e. the vasculature exists in a spatially homogeneous state at its normal level throughout the tumour cell population. For simplicity, we neglect the poor efficiency ('leakiness') and heterogeneities generally found in tumour vasculature, considering only the extreme case where the tumour is fully vascularised. Moreover, we assume there is no vasculature within the necrotic core. Non-dimensionalising as before, we find

$$r^2h'' + 2rh' = \begin{cases} 0 & 0 < r < r_D \\ r^2(h-1) & r_D < r < r_M \\ r^2h & r_M < r \end{cases} \tag{5.6}$$

with solution

$$h_v(r) = \begin{cases} k_1 & 0 < r < r_D \\ 1 - k_2 \frac{1}{r} e^{-r} - k_3 \frac{1}{r} e^{r} & r_D < r < r_M \\ k_4 \frac{1}{r} e^{-r} & r_M < r \end{cases} \tag{5.7}$$

where

$$\begin{aligned} k_1 &= 1 - \frac{e^{r_D - r_M}(r_M + 1)}{r_D + 1} \\ k_2 &= \frac{e^{2r_D - r_M}(r_D - 1)(r_M + 1)}{2(r_D + 1)} \\ k_3 &= \frac{e^{-r_M}(r_M + 1)}{2} \\ k_4 &= \frac{e^{r_M}(r_M + 1)}{2} - \frac{e^{2r_D - r_M}(r_D - 1)(r_M + 1)}{2(r_D + 1)} \ . \end{aligned} \tag{5.8}$$

An example of this predicted vascular acid profile with a comparison against the predicted avascular profile can be seen in Fig. 5.2, with $r_D = 1$ and $r_M = 1.5$. Given experimentally determined parameter estimates of $p = 0.47$ mm^{-1} and $H_0 = 1.0 \times 10^{-5}$ M $\equiv$ pH 5.0 [41, 80], this corresponds to a tumour of radius $R_M \approx 3$ mm, with necrotic core radius $R_D \approx 2$ mm. Notice that the model predicts acidity for an avascular tumour to be higher than that for a vascular tumour, when both tumours produce acid at the same rate. This is to be expected given that there is no acid removal within the tumour in the avascular case. Note, however, that due to an increased reliance on glycolysis, vascular tumours are often found to be more acidic than their avascular counterparts. In the model, this is represented by a higher value of H_0.

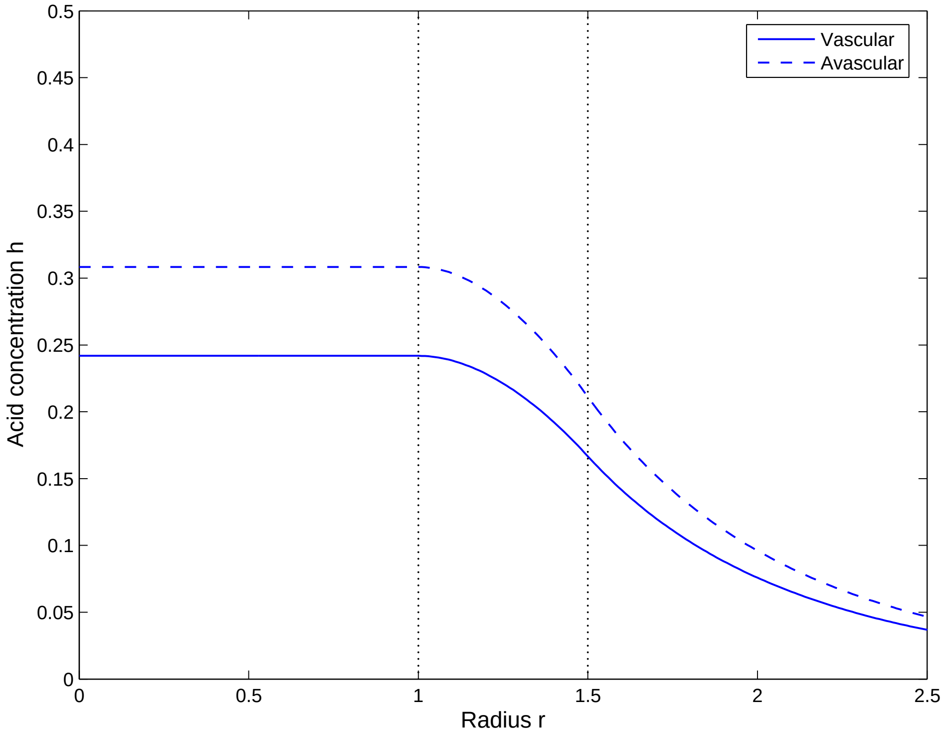

Figure 5.2: Predicted avascular and vascular acid profiles from Eqs. (5.4) and (5.7), with $r_D = 1$ and $r_M = 1.5$.

5.2.2 Necrotic core development

Previous models of tumour growth have assumed tumour necrosis occurs as a result of insufficient nutrient supply. In this chapter we focus on the effect of acid-mediated tumour necrosis on the system. Assuming that high acidity is the sole cause of necrosis in the tumour allows us to calculate the radius of the necrotic core r_D in terms of the tumour outer radius r_M.

In the avascular case and in the absence of a necrotic core (i.e. when $r_D = 0$), from Eq. (5.4) we have

$$h_a(0) = \frac{r_M^2(r_M+3)}{6(r_M+1)} \longrightarrow \infty \qquad \text{as } r_M \to \infty. \tag{5.9}$$

Thus at some critical value of r_M, $h_a(0) > h_M$ and the cells at the centre of the tumour will become necrotic. The critical radius $\hat{r}_M$ at which the necrotic core develops can be found by solving $h_a(0) = h_M$, with $r_D = 0$

$$c_a(\hat{r}_M) = \hat{r}_M^3 + 3\hat{r}_M^2 - 6h_M\hat{r}_M - 6h_M = 0\ . \tag{5.10}$$

As an aside, given a cubic equation

$$f(x) = x^3 + a_2x^2 + a_1x + a_0 = 0, \tag{5.11}$$

define

$$\begin{aligned} P &= \frac{3a_1 - a_2^2}{9}, \\ Q &= \frac{9a_1a_2 - 27a_0 - 2a_2^3}{54}. \end{aligned} \tag{5.12}$$

Then, if the polynomial discriminant $D = P^3 + Q^2 < 0$, all solutions to Eq. (5.11) are real and unequal, and are given by

$$x_n = 2\sqrt{-P}\cos\left(\frac{\theta + 2n\pi}{3}\right) - \frac{a_2}{3}, \tag{5.13}$$

where

$$\theta = \arccos\left(\frac{Q}{\sqrt{-P^3}}\right), \tag{5.14}$$

for $n = 0, 1, 2$, where we choose $\arccos : [-1, 1] \to [0, \pi]$.

Returning to Eq. (5.10), this cubic has exactly one positive real root $\hat{r}_M$, given by application of Eq. (5.13) with $n = 0$. The correct value of n required here is found simply through trial and error across the three possibilities. Taking the threshold for tumour death due to acidity to be $h_M = 0.1$, corresponding to $H_M \equiv$ pH 6 [92], we find that necrosis due to acidity first occurs at $\hat{r}_M = 0.51$ ($\hat{R}_2 \approx 1$ mm).

If $r_M > \hat{r}_M$, then a necrotic core exists, and its radius r_D can be found by noting that the acid concentration at the boundary of the necrotic core will be $h_a(r_D) = h_M$

$$2r_D^3 - 3(r_M + 1)r_D^2 + c_a(r_M) = 0\ . \tag{5.15}$$

In this case, the root of the cubic satisfying $0 < r_D < r_M$ is found from Eq. (5.13), with $n = 2$.

From equation (5.15)

$$\lim_{r_M \to \infty} (r_M - r_D) = \sqrt{2h_M + 1} - 1 \tag{5.16}$$

and hence

$$\frac{r_D}{r_M} \longrightarrow 1, \quad \mathrm{Vol}(r_D, r_M) = \frac{4\pi}{3}(r_M^3 - r_D^3) \longrightarrow \infty \qquad \text{as } r_M \to \infty. \tag{5.17}$$

This means that a large tumour will be mostly comprised of the necrotic core, with the layer of viable cells limited to a thin region at the tumour edge, consistent with experimental results. Nonetheless, the total number of viable cells will continue to increase as the tumour grows.

Turning now to the vascular case, in the absence of a necrotic core we have, from Eq. (5.7)

$$h_v(0) = 1 - e^{-r_M}(r_M + 1) \longrightarrow 1 \qquad \text{as } r_M \to \infty \tag{5.18}$$

and hence we see two distinct patterns of growth, depending on the sign of $h_M - 1$. If $h_M \geq 1$, $h_v(0) < h_M$ for any value of r_M; the tumour vasculature removes the excess acid sufficiently quickly to avoid tumour cell death and no necrotic core will develop. If, however, $h_M < 1$, at some value of r_M, $h_v(0) \geq h_M$ and a necrotic core will develop. This critical radius $\hat{r}_M$ can be found by solving $h_v(0) = h_M$, with $r_D = 0$, leading to the equation

$$c_v(\hat{r}_M) = e^{-\hat{r}_M}(\hat{r}_M + 1) + (h_M - 1) = 0 \ , \tag{5.19}$$

with solutions

$$\hat{r}_M = -1 - W(\frac{h_M - 1}{e}). \tag{5.20}$$

Here W denotes the multivalued Lambert W (or product log) function – the inverse function of $f(W) = We^W$. Note that for $-1/e \leq x < 0$, there are two possible real values of $W(x)$, $W_0(x) \geq -1$ and $W_{-1}(x) \leq -1$ [22]. As $\hat{r}_M \geq 0$, for $h_M < 1$ we can define

$$\hat{r}_M = -1 - W_{-1}(\frac{h_M - 1}{e}) \ . \tag{5.21}$$

Further, for $h_M < 1$ and r_M greater than this critical radius, we find r_D by solving $h_v(r_D) = h_M$

$$e^{r_D - r_M}(r_M + 1) + (h_M - 1)(r_D + 1) = 0 \tag{5.22}$$

with solution

$$r_D = -1 - W_{-1}(\frac{e^{-(r_M+1)}(r_M + 1)}{h_M - 1}) \ . \tag{5.23}$$

From Eq. (5.22), we find

$$\lim_{r_M \to \infty}(r_M - r_D) = -\log(1 - h_M) \tag{5.24}$$

and hence as in the avascular case, Eq. (5.17) holds.

5.2.3 Tumour growth

We consider now the growth dynamics of the tumour, whilst neglecting for now the role of normal tissue on the system. As such, we analyse the inhibitory effects of acidity on tumour growth, whilst neglecting the invasive dynamics arising through the destruction of normal tissue. The rate at which a tumour grows may be dependent on a large number of factors, such as nutrient supply, cellular density or internal pressure gradients. Here we make the simplifying assumption that the rate of change of tumour volume is entirely dependent on the tumour radius and the radius of the necrotic core

$$\frac{d}{dt}(\mathrm{Vol}) = F(R_D, R_M) \tag{5.25}$$

for some mitosis function F. It should be noted, however, that the necrotic radius R_D is defined by the acid profile around the tumour ($H(R_D) = H_M$), and hence the growth function is implicitly dependent on a range of factors, such as vascular density.

Greenspan [51] makes the assumption that the necrotic cellular debris continually disintegrates into simpler chemical compounds at a rate proportional to the core volume. These compounds flow into the surrounding tissue and the cell volume lost in this way is replaced by cells pushed inward through surface tension forces. Moreover, the assumption is made that the rate of cellular proliferation is constant per unit volume in the viable region. Under these assumptions, Eq. (5.25) becomes

$$\frac{dR_M^3}{dt} = S(R_M^3 - R_D^3) - LR_D^3\ . \tag{5.26}$$

Taking $\tau = St/3$ and $r = qR$, we may non-dimensionalise the system to obtain

$$r_M^2 \frac{dr_M}{d\tau} = r_M^3 - \gamma^3 r_D^3 \tag{5.27}$$

where $\gamma = \sqrt[3]{L/S + 1}$.

Note that while there is no necrotic core (when $r_D = 0$), the tumour radius will grow exponentially with

$$r_M(\tau) = r_M(0)e^{\tau} \ . \tag{5.28}$$

This corresponds to well-known experimental evidence that the early stages of solid tumour development follow a simple exponential growth pattern [74]. In particular, in the case of a vascular tumour with $h_M \geq 1$, the model predicts that a necrotic core will never develop and thus the tumour will continue to grow exponentially into the surrounding tissue. For an avascular tumour or a vascular tumour with $h_M < 1$, however, a different growth pattern is observed. From Eq. (5.17), we know that $r_D/r_M \to 1$ as $r_M \to \infty$. Assuming that, at time 0, the tumour is small enough that there is no necrotic core (i.e. $r_M(0) \leq \hat{r}_M$), at some value of r_M we will find $r_D = r_M/\gamma < r_M$. Then from Eq. (5.27), $dr_M/d\tau = 0$, and a benign steady state is reached. In other words, we find that an avascular tumour will always have a benign growth pattern. A vascular tumour will either have a benign or invasive growth pattern dependent on the value of the critical parameter h_M.

The system is completely defined by Eq. (5.27) and Eq. (5.15) or (5.23), and relies only on the parameters γ, h_M and the initial condition $r_M(0)$. Examples of the growth patterns observed are given in Fig. 5.3. In the avascular case, a two-phase growth pattern is observed (Fig. 5.3 (a)). Initially, the tumour grows exponentially, without a necrotic core. At the critical time $\hat{\tau}$, a necrotic core begins to develop and the second phase of tumour growth begins. During this phase, we see very little change in tumour size. However, the necrotic core grows rapidly towards its equilibrium value. Note that γ represents the equilibrium $r_M : r_D$ ratio. The corresponding vascular growth is very similar when $h_M < 1$ (Fig. 5.3 (b)) and may be contrasted to the invasive growth seen when $h_M \geq 1$ (Fig. 5.3 (c)). In this final case, as r_M becomes large, other limiting factors such as nutrient supply and immune response will have greater impact on the tumour growth.

The time $\hat{\tau}$ at which we see the onset of necrosis can be found from Eq. (5.28), taking $r_M = \hat{r}_M$

$$\hat{\tau} = \log \hat{r}_M - \log r_M(0) \ . \tag{5.29}$$

Using parameters $h_M = 0.1$ and $r_M(0) = 0.1$ ($R_M(0) \approx 0.2$ mm), we find necrosis occurs at $\hat{\tau} = 1.63$ and $\hat{\tau} = 1.67$ in the avascular and vascular cases respectively. The equilibrium size $\bar{r}_M$ may be found by noting that $\bar{r}_M = \gamma \bar{r}_D$. In the avascular case, using Eq. (5.15) we find

$$\bar{r}_M = \frac{\gamma}{(\gamma-1)(\gamma+2)} \Big[-(\gamma+1) + 2c_1 \cos\Big[\frac{1}{3}\arccos(-\frac{c_2}{c_1^3})\Big]\Big] \tag{5.30}$$

where

$$\begin{aligned} c_1 &= \sqrt{(\gamma+1)^2 + 2h_M\gamma(\gamma+2)} \ , \\ c_2 &= (\gamma+1)^3 + 6h_M(\gamma+2) \ . \end{aligned} \tag{5.31}$$

For the parameter set used in Fig. 5.3, we find $\bar{r}_M = 0.75$, corresponding to a final radius of $\bar{R}_M \approx 1.6$ mm. For the vascular case, we use Eq. (5.22), again setting $\bar{r}_M = \gamma \bar{r}_D$. Solving this numerically, we find $\bar{r}_M = 0.80$ corresponding to $\bar{R}_M \approx 1.7$ cm. These numbers demonstrate further the similarity between avascular and vascular growth when h_M is small.

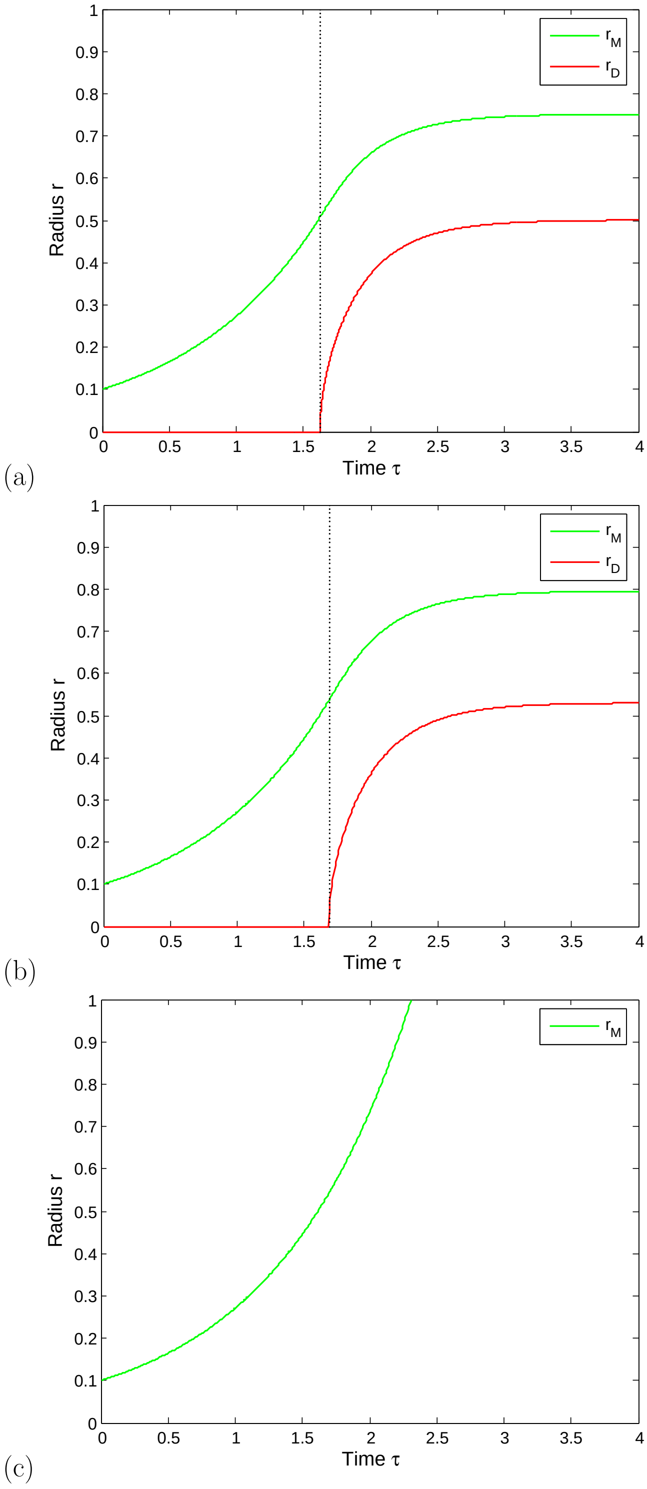

Figure 5.3: Results from Eqs. (5.15), (5.23)) and (5.27). Predicted (a) avascular and (b) vascular tumour growth with parameters $\gamma = 3/2$, $h_M = 0.1$ and $r_M(0) = 0.1$. (c) Vascular growth with $h_M = 1.5$ and $r_M(0) = 0.1$.

5.2.4 Normal tissue invasion

We now move on to consider the effects of normal tissue on the system. Let r_N denote the non-dimensionalised distance from the tumour centre to the normal tissue. Assume that initially the system has $r_D = 0$ and $r_N = r_M$ i.e. the tumour is small enough that there is no necrotic core. Normal cells die if h increases above a critical value $h_N = H_N/H_0$, where $h_N \ll h_M$.

In the vascular case, from Eq. (5.7)

$$h_v(r_M) = (r_M \cosh r_M - \sinh r_M)\frac{e^{-r_M}}{r_M} \qquad (\text{as } r_D = 0). \tag{5.32}$$

We assume that the only mechanism by which the tumour may invade the normal tissue is to acidify the peritumoural space and induce normal tissue death. Hence normal tissue will recede and the tumour will advance if and only if the acid levels at the tumour periphery are higher than the threshold for normal cell death i.e. $h(r_M) > h_N$. Note that h is an increasing function of r_M, and hence if $h(r_M(0)) > h_N$, the tumour will grow unimpeded as was seen when normal tissue was neglected in the system.

In the avascular case, from Eq. (5.4)

$$h_a(r_M) = \frac{r_M^2}{3(1 + r_M)} \qquad (\text{as } r_D = 0). \tag{5.33}$$

Again the normal tissue will recede if and only if $h(r_M) > h_N$. Taking $h_N = 0.01$, corresponding to $H_N \equiv$ pH 6.8 [92], we find that in both the vascular and avascular cases invasion will occur only if $r_M \geq 0.19$, equivalent to $R_M \approx 0.4$ mm.

If $h(r_M) > h_N$, then we can calculate r_N through solution of the equation $h(r_N) = h_N$,

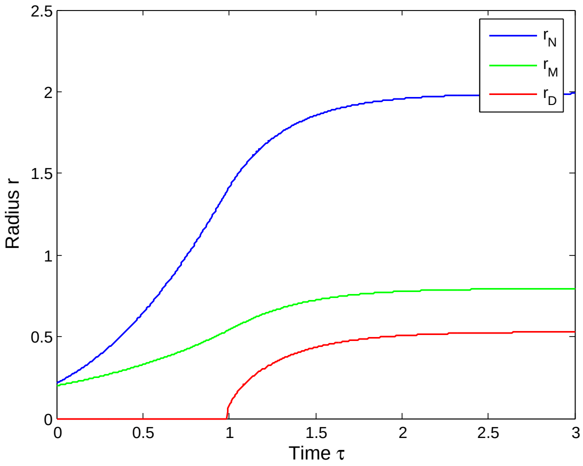

Figure 5.4: Results from Eq. (5.34). Recession of normal tissue accompanying vascular tumour growth. Parameter values used are $h_N = 0.01$, $\gamma = 3/2$, $h_M = 0.1$ and $r_M(0) = 0.2$.

i.e. $k_4 e^{-r_N}/r_N = h_N$

$$r_N = W_0\left(\frac{k_4}{h_N}\right) \tag{5.34}$$

where here we choose the principal value of the Lambert W-function as $k_4 > 0$ and $h > 0$.

Fig. 5.4 shows normal tissue receding as the tumour grows. Notice the development of an acellular gap between the advancing tumour front and receding normal tissue, consistent with experimental observations [41].

5.3 Acid-induced quiescence

In the previous section, we developed a simple model of three-dimensional tumour growth to examine the role of acidosis in the interaction between normal and tumour cell populations. Both vascular and avascular tumour dynamics were investigated, and a number of different behaviours observed. Whilst an avascular tumour always proceeds to a benign steady state, a vascular tumour may display either benign or invasive dynamics, depending on the value of the critical parameter h_M. The model also predicts the development of an experimentally-observed acellular gap separating the advancing tumour and receding host tissue fronts. One criticism that may be levelled at the model is the size of the acellular gap as predicted in Fig. 5.4 – the interfacial gap is predicted to be of a similar size to the tumour, and larger than the experimentally-determined estimates of 10–100 μm [41] (see Fig. 3.4).

In this section, we extend the previous model through the inclusion of quiescent (non-proliferating) tumour cells. Within avascular tumours, in particular, the vast majority of viable cells are quiescent, with active cells restricted to the nutrient-rich outer rim. These quiescent cells are essentially metabolically-inactive, producing significantly less acid than their proliferating counterparts. By considering both active and quiescent cells, we give a more physiologically-accurate description of the acidity in and around the tumour tissue.

The tumour is again modelled as a sphere; however, we assume here that within the viable region $R_D < R < R_M$, the active proliferating tumour cells are restricted to the outer rim $R_Q < R < R_M$, whilst the region $R_D < R < R_Q$ contains quiescent cells (see Fig. 5.8). Returning to Eq. (5.2), we define the acid production rate $r_H = \phi_Q$ within the quiescent region and $r_H = \phi_A$ within the active region, where $\phi_Q \ll \phi_A$, as quiescent cells are relatively metabolically inactive.

We focus here on avascular tumour growth (i.e. $V = 0$ within the tumour), as this case is more amenable to analysis. As before, taking $p = \sqrt{r_V V_N / D_H}$ and $H_0 = \phi_A K_M / r_V V_N$,

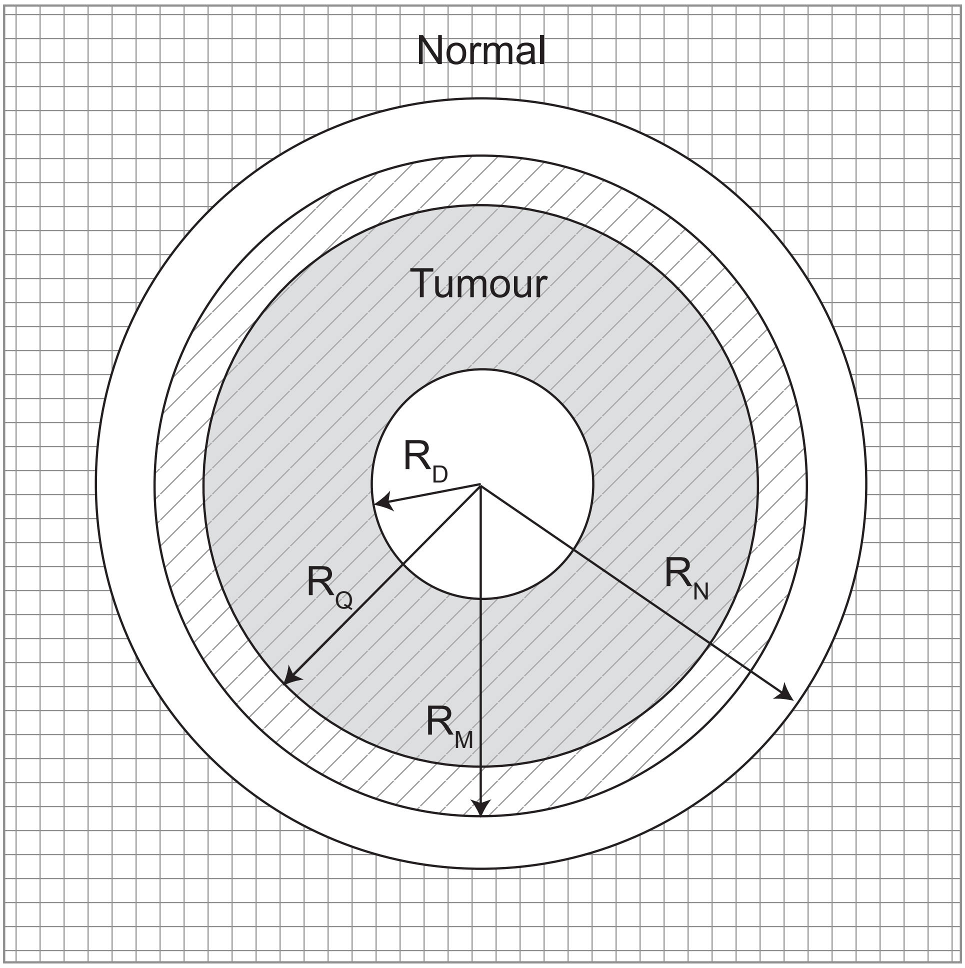

Figure 5.5: Cross-section of a tumour and its surrounding tissue showing the central necrotic core, $R < R_D$, a layer of quiescent tumour cells $R_D < R < R_Q$, a layer of proliferating tumour cells $R_Q < R < R_M$, the acellular gap separating normal and tumour cell fronts $R_M < R < R_N$, and the normal cells $R_N < R$.

we may non-dimensionalise Eq. (5.2) with $r = pR$ and $h = H/H_0$ to obtain

$$r^2 h'' + 2rh' = \begin{cases} 0 & 0 < r < r_D, \\ -\varepsilon r^2 & r_D < r < r_Q, \\ -r^2 & r_Q < r < r_M, \\ r^2 h & r_M < r, \end{cases} \tag{5.35}$$

where $\varepsilon = \phi_Q/\phi_A \ll 1$, and the primes denote the derivative with respect to r.

Assuming as before that $\lim_{r\to\infty} h(r) = 0$ i.e. that there is no excess acidity a long distance from the tumour, and further that h and its derivative are continuous at r_D, r_Q and r_M, Eq. (5.35) has solution

$$h(r) = \begin{cases} k_1 & 0 < r < r_D, \\ k_2 - k_3\frac{1}{r} - \varepsilon\frac{1}{6}r^2 & r_D < r < r_Q, \\ k_4 - k_5\frac{1}{r} - \frac{1}{6}r^2 & r_Q < r < r_M, \\ k_6\frac{1}{r}e^{-r} & r_M < r, \end{cases} \tag{5.36}$$

where the constants k_i are given by

$$\begin{aligned} k_1 &= \frac{2\varepsilon r_D^3 + 2(1-\varepsilon)r_Q^3 + r_M^2(r_M+3)}{6(r_M+1)} - \frac{\varepsilon r_D^2 + (1-\varepsilon)r_Q^2}{2}, \\ k_2 &= k_1 + \varepsilon\frac{r_D^2}{2}, \\ k_3 &= \varepsilon\frac{r_D^3}{3}, \\ k_4 &= k_1 + \frac{\varepsilon r_D^2 + (1-\varepsilon)r_Q^2}{2}, \\ k_5 &= \frac{\varepsilon r_D^3 + (1-\varepsilon)r_Q^3}{3}, \\ k_6 &= e^{r_M}\frac{-\varepsilon r_D^3 - (1-\varepsilon)r_Q^3 + r_M^3}{3(r_M+1)}. \end{aligned} \tag{5.37}$$

An example of this predicted acid profile can be seen in Fig. 5.6. Following Patel *et al.* [92], we take $\varepsilon = 0.01$ – that is, quiescent tumour cells' rate of acid production is two

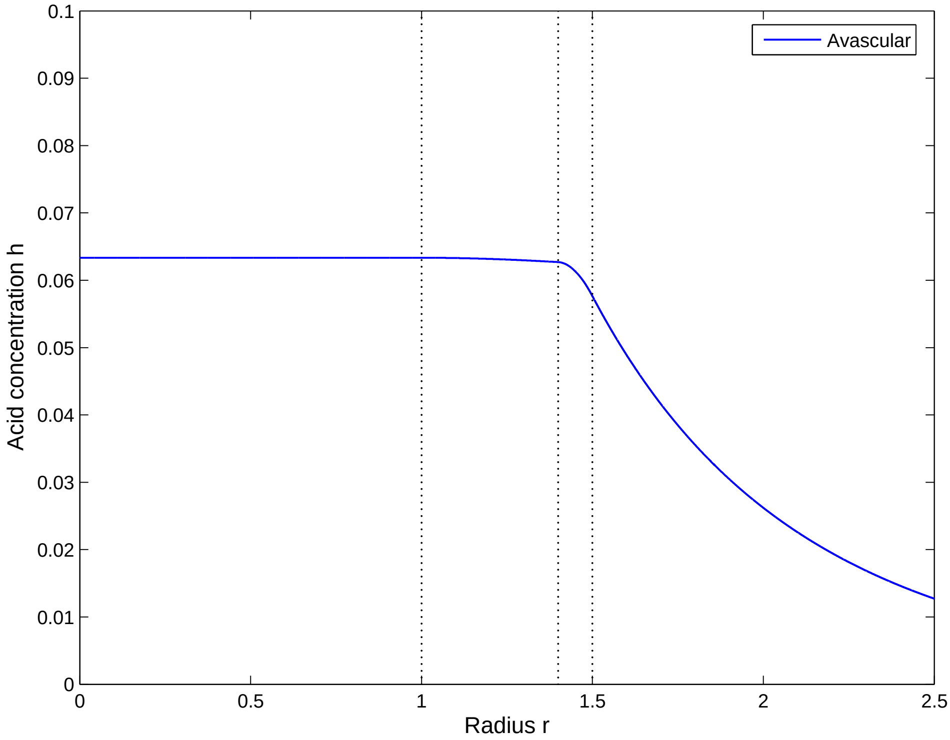

Figure 5.6: Results from Eq. (5.36). Predicted avascular acid profile for the extended model including quiescent cells. Parameter values used are $r_D = 1$, $r_Q = 1.4$, $r_M = 1.5$ and $\varepsilon = 0.01$.

orders of magnitude less than their proliferating counterparts. Because of this, the levels of acidity within the tumour are found to be significantly lower than those predicted by the basic model (compare Fig. 5.2).

It is known that high levels of acidity can induce quiescence in tumour tissue [20]. Assuming that acidity is the sole cause of necrosis and quiescence within the tumour allows us to calculate the radii of the necrotic core, r_D, and the quiescent region, r_Q, as functions of the tumour outer radius, r_M. As before, we assume there exist sharp acid threshold concentrations H_Q and H_D above which tumour cells cannot proliferate and survive respectively. Taking $h_i = H_i/H_0$, the case $h_Q = h_D$ does not allow for any quiescent tumour cells within the system, and the analysis reduces to that found in the previous section.

We consider instead here the case $h_Q < h_D$.

Continuing as before, while the tumour consists of only active proliferating cells (i.e. $r_D = r_Q = 0$), from Eq. (5.36) we have

$$h(0) = \frac{r_M^2(r_M + 3)}{6(r_M + 1)} \longrightarrow \infty \qquad \text{as } r_M \to \infty. \tag{5.38}$$

Thus at some critical value $r_M = \hat{r}_M$, $h(0) = h_Q$, and the cells at the centre of the tumour will become quiescent. This critical radius is found by solving

$$c_3(\hat{r}_M) = \hat{r}_M^3 + 3\hat{r}_M^2 - 6h_Q\hat{r}_M - 6h_Q = 0. \tag{5.39}$$

The positive solution $\hat{r}_M$ is given by Eq. (5.13), taking $n = 0$.

If $r_M > \hat{r}_M$, then a quiescent region exists, and its radius r_Q may be found by noting that the acid concentration at its boundary will be $h(r_Q) = h_Q$

$$c_4(r_Q, r_M) = 2(1 - \varepsilon)r_Q^3 - (3 - 2\varepsilon)(r_M + 1)r_Q^2 + c_3(r_M) = 0. \tag{5.40}$$

The solution in r_Q is given by Eq. (5.13), choosing $n = 2$.

If $\varepsilon > 0$, then we find that acidity will increase at the tumour boundary as it grows. Eventually all tumour cells will become quiescent, and the radius $\hat{r}_Q$ at which this occurs may be found through solution of Eq. (5.40), with $r_Q = r_M$

$$\hat{r}_Q = \frac{3h_Q + \sqrt{9h_Q^2 + 12h_Q\varepsilon}}{2\varepsilon}. \tag{5.41}$$

Consider now the formation of necrosis within the tumour. While $r_D = 0$ and $r_Q > 0$, from Eq. (5.36) we have

$$h(0) = h(r_Q) + \varepsilon\frac{r_Q^2}{6} = h_Q + \varepsilon\frac{r_Q^2}{6}. \tag{5.42}$$

Thus setting

$$h_* = h_Q + \varepsilon\frac{\hat{r}_Q^2}{6} = \frac{h_Q(\hat{r}_Q + 3)}{2}, \tag{5.43}$$

we see two distinct patterns of growth, dependent on the sign of $h_D - h_*$. If $h_D > h_*$, then no necrotic core will develop, and the tumour will grow to a state containing only quiescent cells. If $h_D < h_*$, however, at some critical value $r_M = \hat{r}_D$, $h(0) = h_D$ and the cells at the centre of the tumour will become necrotic. From Eq. (5.42), we find that this occurs when

$$r_Q = r_* = \sqrt{\frac{6(h_D - h_Q)}{\varepsilon}}. \tag{5.44}$$

$\hat{r}_D$ may then be found by solving $c_4(r_*, r_M) = 0$ for r_M. This is achieved using Eq. (5.13), taking $n = 0$.

If $r_M > \hat{r}_D$, then a necrotic core exists and its radius is given by noting that $h(r_D) = h_D$

$$c_5(r_D, r_Q) = 2r_D^3 - 3r_Q r_D^2 + (r_Q^2 - r_*^2)r_Q = 0. \tag{5.45}$$

The solution in r_D is found using Eq. (5.13), taking $n = 2$.

Furthermore, we know that $h(r_Q) = h_Q$

$$c_6(r_D, r_Q, r_M) = r_Q c_4(r_Q, r_M) - 2\varepsilon(1 + r_M - r_Q)r_D^3 = 0. \tag{5.46}$$

Given r_M, we may numerically calculate $r_Q \in (r_D, r_M)$ from Eq. (5.46), using the expression for r_D in Eq. (5.45).

The set of equations above allows calculation of the non-dimensional quiescent tissue radius, r_Q, and the necrotic core radius, r_D, for any value of outer radius r_M. These radii may then be used to determine tumour growth. As an analogue to Eq. (5.26), we have

$$\frac{dR_M^3}{dt} = S(R_M^3 - R_Q^3) - LR_D^3, \tag{5.47}$$

that is, the tumour grows at a rate proportional to the volume of active proliferating cells, whilst growth is inhibited through constant degradation of the necrotic material. Taking $\tau = St/3$ and $r = pR$, we may non-dimensionalise to obtain

$$r_M^2 \frac{dr_M}{d\tau} = r_M^3 - r_Q^3 - \gamma^3 r_D^3, \tag{5.48}$$

where $\gamma = \sqrt[3]{L/S}$. Assuming that, at time 0, the tumour is small enough that there is no necrotic core or quiescent region (i.e. $r_D = r_Q = 0$), then the system is completely defined by Eqs. (5.45), (5.46) and (5.48), relying on parameters ε, γ, h_D, h_Q and the initial condition $r_M(0)$.

Examples of the growth patterns observed are given in Fig. 5.7. Using parameter estimates of $h_D = 0.1$, corresponding to pH 6, and $h_Q = 0.04$, corresponding to pH 6.4 [92], $h_D < h_*$ and so we see a three-phase growth. Initially, the tumour grows exponentially, whilst all cells are proliferative. At the critical radius $r_M = \hat{r}_M$, the central tissue becomes quiescent, restricting the active cells to a thin outer rim (Fig. 5.7 (a)). At a later stage, when $r_M = \hat{r}_D$, we see the development of a necrotic core, followed by convergence of the tumour to its equilibrium size (Fig. 5.7 (b)). In Fig. 5.7 (c), we increase the tumour's susceptibility to acid-induced quiescence, taking $h_Q = 0.01$, equivalent to pH 6.8. In this case, $h_D > h_*$, and no necrotic core will develop. Rather, it slowly grows to its equilibrium size $r_M = \hat{r}_Q$ where all the tumour cells are quiescent.

We move on now to the acid-mediated invasion of normal tissue, and the corresponding development of an acellular gap separating the advancing tumour and receding host tissue fronts. Assume as before that there exists a sharp acid threshold concentration H_N above which normal cells die, and let $h_N = H_N/H_0$. Then the normal tissue front r_N is defined by the relationship $h(r_N) = h_N$. In Fig. 5.7 (b), we see that in necrotic growth, the

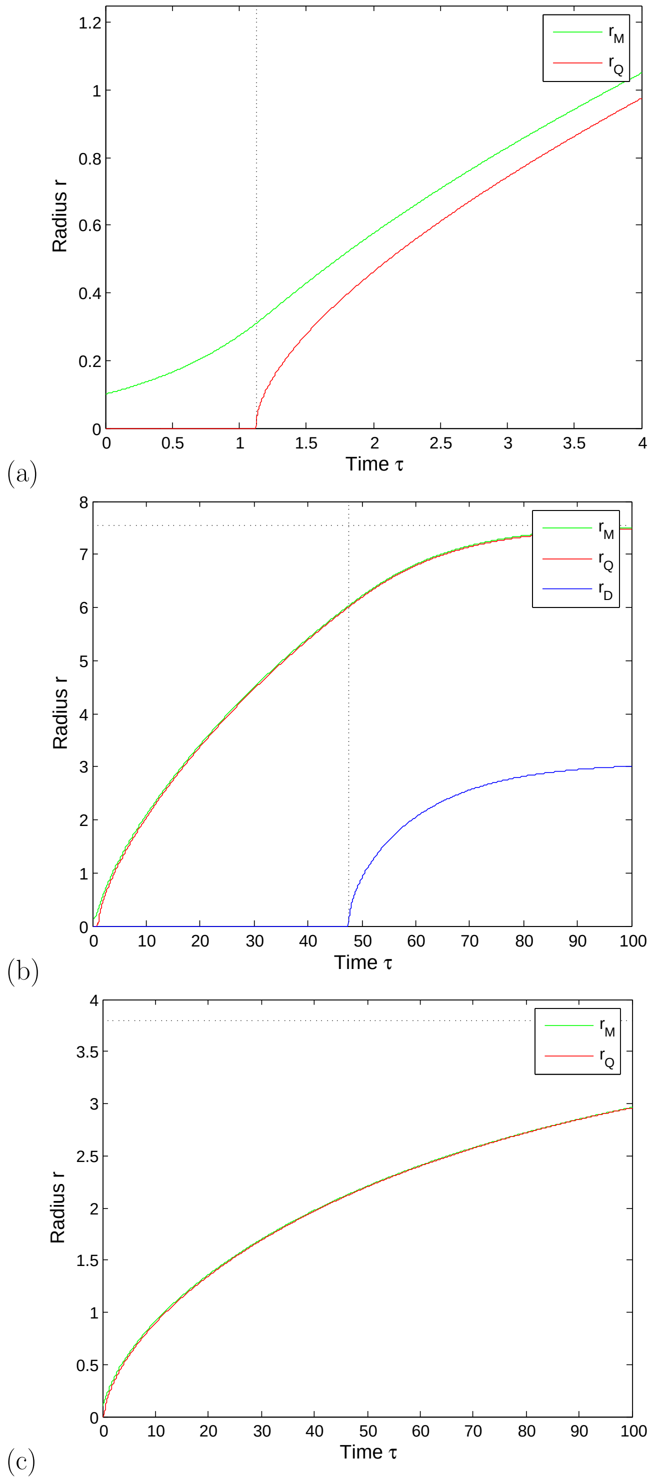

Figure 5.7: Results from Eqs. (5.45), (5.46) and (5.48). (a) Early-stage and (b) late-stage tumour growth with quiescence and necrosis, with parameters $\varepsilon = 0.01$, $\gamma = 1/2$, $h_D = 0.1$, $h_Q = 0.04$ and $r_M(0) = 0.1$. (c) Non-necrotic growth with parameters $\varepsilon = 0.01$, $h_D = 0.1$, $h_Q = 0.01$ and $r_M(0) = 0.1$.

layer of proliferating cells forms a very thin layer at the edge of the tumour, hence we may approximate $r_M \approx r_Q$ at equilibrium. In non-necrotic growth (c), there are no proliferating cells at equilibrium, hence $r_M = r_Q$. In both cases, we may assume that $h(r_M) = h(r_Q) = h_Q$. Assuming further that $r \gg 0$, then, from Eq. (5.36), the interfacial width ω at equilibrium may be approximated by the simple relationship

$$\omega = r_N - r_M \approx \log \frac{h_Q}{h_N}. \tag{5.49}$$

In Fig. 5.8 we compare the interfacial width at equilibrium ω with changes in tumour quiescence threshold h_Q. Eq. (5.49) represents a reasonable approximation to ω, but we see the assumptions $h(r_M) = h_Q$ and $r \gg 0$ cause a slight overestimation of this gap size. Most importantly, through comparison of Figs. 5.7 and 5.8, we see that the equilibrium tumour width is predicted to be approximately ten times as large as the interfacial width. This is a significantly more physiologically accurate than the basic model (see Fig. 5.4), where the gap was predicted to be of a similar size to the tumour.

5.4 Discussion

In this chapter we have presented a mathematical study of both vascular and avascular tumour growth, where the invasion mechanism is the acidification of the microenvironment surrounding the tumour due to increased reliance on glycolysis. Utilising the vast difference between the timescales of tumour growth and acid movement allows us to treat the tumour radius as a parameter in terms of which other variables are expressed. In particular, we determine the equilibrium acid profile and necrotic core radius as a function of the tumour radius.

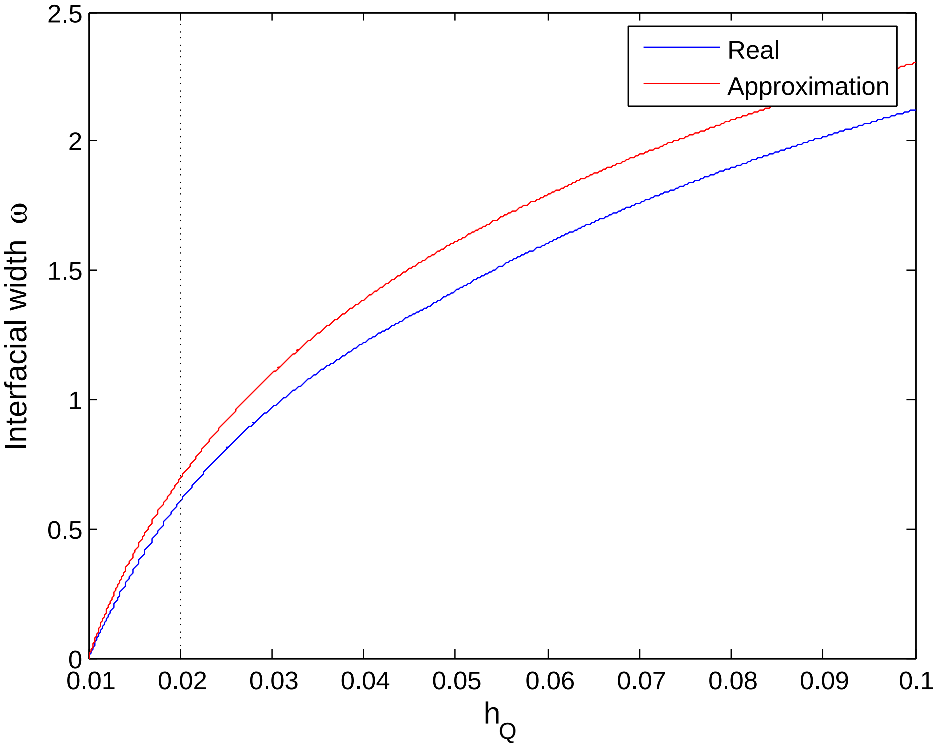

Figure 5.8: Variation in size of acellular gap separating tumour and normal tissue fronts at equilibrium, with changes in the tumour quiescence threshold h_Q. The gap width is compared with the simple approximation in Eq. (5.49). Parameter values used are $\varepsilon = 0.01$, $\gamma = 1/2$, $h_D = 0.1$ and $h_N = 0.01$. The dotted line represents the crossover from non-necrotic to necrotic growth.

The analysis of the basic model in Section 5.2 predicts three regimes of tumour growth. If the rate of acid removal from the tumour is insufficient, we see exponential growth followed by auto-toxicity, resulting in a benign tumour. This is found always to occur in an avascular tumour, and it may also occur in a vascular tumour if the critical parameter $h_M < 1$. Conversely, if $h_M \geq 1$, a vascular tumour displays sustained growth, and invades the whole of the normal tissue space. In both of these cases, the advancing tumour front is separated from the receding normal tissue by an acellular gap. Finally, if the tumour is sufficiently small, we see no growth as the microenvironmental acid perturbations are insufficient to induce normal cell death. Note, however, that for tumours of this size, inhomogeneities have more effect on the system and thus stochastic or cellular automaton [5, 92] approaches may be more applicable than the mean-field type approach used here.

Within the model, three dominant factors determine tumour growth: acid production, acid removal due to tumoural and peritumoural vascularity, and cellular sensitivity to acid. In general, tumour growth is enhanced through increasing acid production to induce toxicity in the adjacent normal tissue. However, in order to display sustained growth, the tumour must limit excess acid accumulation to avoid auto-toxicity. This balance may resolve itself in several ways. Tumour growth could be limited by cellular sensitivity: that is, the dominant populations within the tumour may retain significant sensitivity to acid-induced apoptosis. As such, tumour expansion is halted when the intratumoural $\mathrm{pH_X}$ is only modestly reduced. Tumour growth could also be limited if the vascularity is limited: the intratumoural hydrogen ions will accumulate sufficiently to create an acidic $\mathrm{pH_X}$ that halts proliferation. In these settings, tumour growth could be rapidly increased through adoption of the angiogenic phenotype or emergence of new populations with additional mutations that render them more resistant to acid-induced apoptosis. Finally, tumour growth could be limited by acid production: the tumour does not produce enough acid to create a peritumoural hydrogen ion gradient sufficient to kill the normal cells. In this case, emergence of phenotypes with higher glycolytic metabolism will result in invasive growth, consistent with findings that rate of glucose uptake correlates with more malignant behaviour [73].

The converse of each of the above scenarios suggests possible cancer treatment strategies. In general, the results favour tumour anti-angiogenesis strategies, because decreased vascular density will reduce acid removal as well as nutrient supply. If the resulting decrease in $\mathrm{pH_X}$ exceeds the tolerance of tumour cells to local acidosis, the resulting apoptosis would halt tumour growth. Mathematically, this is achieved through reducing $h_M = H_M r_V V_N / r_H K_M$ below the critical value of 1. This parameter may also be reduced through the novel strategy of manipulating systemic pH. A recent study demonstrated that patients with metastatic renal cancer benefit from cytoreductive nephrectomy [44]. The authors propose that removal of functioning nephrons produces mild renal failure that is associated with systemic acidosis. This decrease in the serum pH reduces acid removal, since diffusion of hydrogen ions from the tumour interstitium into blood vessels is dependent on the concentration gradient across the vessel wall. The resulting decrease in intratumoural $\mathrm{pH_X}$ may again induce tumour auto-toxicity. However, both approaches above come with a cautionary note. Reduced acid removal will result in an increased peritumoural pH gradient, thus increasing degradation of normal tissue and thus potentially promoting tumour growth. As such, perhaps the most effective treatment suggested by the model is to poison the membrane pumps that transport hydrogen ions from the intracellular to extracellular space within the tumour (through drugs such as amiloride, for example). This would increase the tumour cell sensitivity to $\mathrm{pH_X}$ and furthermore decrease the peritumoural acid gradient.

The model's predictions may be compared to experimental results and clinical observations. The prediction of the presence and range of a pH gradient extending into the peritumoural normal tissue is consistent with the data of Martin and Jain [80]. We also demonstrate that whilst acidity correlates with increased tumour invasion [81], brief systemic acidosis may induce widespread tumour apoptosis and regression [65]. The most verifiable prediction is the development of an appreciable acellular gap separating the advancing tumour and receding normal tissue edges. Our analysis shows that the existence of such a gap is dependent only on tumour size and acid production rates and thus should be apparent in a wide range of cancer types. In a study performed on human head and neck carcinoma, this acellular gap was observed in 67% of cases [41]. It should be noted, however, that tumours use a variety of mechanisms to invade normal tissue. As such, they may create insufficient acid perturbations to induce an acellular gap, but nonetheless continue to grow. In these cases, mechanisms additional to tissue acidification must be considered.

One criticism of the basic model described in Section 5.2 is that the width of the interfacial acellular gap is predicted to be of a similar size to the tumour, larger than has been observed experimentally. Within the basic model, we considered two types of tumour cell – active proliferating cells and necrotic cells. Within avascular tumours in particular, the vast majority of the viable cells are quiescent, producing significantly less acid than their proliferating counterparts. In Section 5.3 we extended our modelling framework to account for these quiescent tumour cells within avascular tumours. Analysis of this extended model gives a more physiologically accurate description of the interfacial gap, predicting that the gap width is an order of magnitude smaller than the tumour radius at equilibrium.

It is clear that tumour growth is dependent on the complex interactive dynamics of many different factors, including the supply of nutrients and growth factors and the specific mutations displayed by the tumour population. This growth is further complicated by any inhomogeneities found within the tumour. Using simplifying assumptions, we have shown here that increased tumour acid production alone, almost universally observed in clinical cancers, is sufficient to explain both benign and invasive growth. As such, acidity may play a dominant role in tumour progression. Critical parameters in the transition from premalignant to malignant morphology include acquisition of angiogenesis, increased glucose utilisation and loss of critical pH-sensitive genes, all observed in human tumours. Various therapeutic strategies are suggested to inhibit tumour growth. In particular, the model suggests the counter-intuitive approach of further increasing tumour acidity, in order to induce auto-toxicity. Experimental results verifying this observation would be of considerable interest.

Chapter 6

Quiescence as a mechanism for cyclical acidosis

6.1 Introduction

A key factor in the adoption of aerobic glycolysis by tumour cell populations is their exposure to an unstable microenvironment, experiencing fluctuations in substrate supply. For example, normoxic–hypoxic cycles in tumours have been measured to occur with periodicities of minutes [68], hours [58] and days [47]. From a bioenergetic perspective, those cells in which aerobic glycolysis is constitutively upregulated will be better placed to respond to these periods of hypoxia, and thus positively selected by somatic evolutionary pressures.

Using a magnetic resonance imaging (MRI) technique that is sensitive to oxygen levels, fluctuations in signal intensity (oxygenation) have been shown to occur with periodicities of both one and twenty cycles per hour [9]. Contrastingly, using microelectrodes, oxygenation cycles have been measured with periodicities of 1–2 per minute [13]. These discrepancies may be explained because MRI is relatively insensitive to rapid fluctuations, whilst instabilities in microelectrodes mean this modality is insensitive to slower changes [45].

Each of the studies mentioned above shows that tumour cells experience considerable inconsistencies in oxygen delivery. The primary explanation put forward for transient hypoxia and reoxygenation is fluctuations in the haemodynamics, or blood delivery, of nearby and distant vessels [45, 67]. Rapid normoxic–hypoxic cycles are thought to occur due to fluctuations in haematocrit, the concentration of red cells in the blood [28], or through vasomotion, rhythmic oscillations in vessel diameter [109]. Longer cycles, occurring over days, are likely to be due to vascular remodelling, the active process of altering the structure and arrangement of blood vessels [67, 91]. Vascular remodelling is driven by cycles of angiogenesis promoted by hypoxia-induced expression of vascular endothelial growth factor (VEGF), an induction and survival factor for new blood vessels [47].

In this chapter, we examine an alternative mechanism for the observed substrate fluctuations in tumour tissue, namely cellular quiescence. In Section 5.3, we noted that high levels of acidity can induce cells to cease proliferation, i.e. become quiescent [20]. Quiescent cells are essentially metabolically inactive, producing significantly less acid than their proliferating counterparts. Thus the level of acidity will decrease, in time allowing cells to resume proliferation. We demonstrate that this simple negative feedback mechanism may produce the observed cycles in tumour substrate levels. Whilst our focus is on growth inhibitors produced by tumour tissue, such as lactic acid, the analysis is equally valid for growth promoters consumed by tumour tissue, such as oxygen.

6.2 Model development

Following Chapter 5, we model the tumour as a sphere of radius R_M and assume that spherical symmetry prevails at all times. We consider first the dynamics of acidity in and around the tumour, though later we shall show that the analysis holds for the dynamics of other substrates, such as oxygen.

Reiterating the notation of Eq. (4.2), let H denote the extracellular concentration of excess hydrogen ions, where excess means above its normal level. We assume that there exists a sharp acidity threshold H_Q above which tumour cells cease proliferation [20]. Define the acid production rate $r_H = \phi_Q$ per unit volume for quiescent cells and $r_H = \phi_A$ for active cells, where $\phi_Q \ll \phi_A$ as quiescent cells are relatively metabolically inactive. The vascular density is taken to be homogeneously $V = V_M$ within the tumour, and $V = V_N$ elsewhere. Extending the work of Chapter 5, we allow for a lag time t_0 between extracellular acid levels changing, and cells mounting the appropriate response of quiescence or proliferation. Under these assumptions, we have

$$\frac{\partial H}{\partial t} - \frac{D_H}{R^2}\frac{\partial}{\partial R}\left(R^2\frac{\partial H}{\partial R}\right) \tag{6.1}$$

$$= \begin{cases} \Big[(\phi_A - \phi_Q)\theta(H_Q - H(t-t_0)) + \phi_Q\Big]K_M - r_V V_M H & 0 < R < R_M \\ -r_V V_N H & R_M < R, \end{cases}$$

where K_M denotes the tumour cell density, r_V the acid removal rate, D_H the acid diffusion coefficient and θ the Heaviside (or unit step) function defined by

$$\theta(x) = \begin{cases} 0 & x < 0 \\ 1 & x \geq 0. \end{cases} \tag{6.2}$$

The bracketed term in the second line of Eq. (6.1) simply represents cells producing acid at rate ϕ_A if $H(t-t_0) < H_Q$, and ϕ_Q otherwise.

Taking $p = \sqrt{r_V V_N / D_H}$, $H_0 = \phi_A K_M / r_V V_N$ and $T = (r_V V_N)^{-1}$, we may non-dimensionalise Eq. (6.1) with $r = pR$, $h = H/H_0$ and $\tau = t/T$ to obtain

$$h_\tau - (h_{rr} + 2h_r/r) = \begin{cases} (1-\varepsilon)\theta(h_Q - h(\tau - \tau_0)) + \varepsilon - \psi^2 h & 0 < r < r_M \\ -h & r_M < r, \end{cases} \tag{6.3}$$

where $\varepsilon = \phi_Q/\phi_A \ll 1$, $\tau_0 = t_0/T$, $h_Q = H_Q/H_0$, $\psi = \sqrt{V_M/V_N}$ and $r_M = pR_M$, subject to continuity of h and h_r at $r = r_M$ and $\lim_{r\to\infty} h(r) = 0$.

Whilst within this thesis we focus on describing the dynamics of acid in and around tumour tissue, Eq. (6.3) can be applied to describe a number of different growth factors. Consider, for example, the dynamics of oxygen – from this perspective a positive growth factor consumed by both normal and tumour tissue. Let C denote the extracellular concentration of oxygen, and suppose that tumour cells cease proliferation when oxygen drops below a threshold concentration C_Q. Let $\bar{\phi}_A$, $\bar{\phi}_Q$ and $\bar{\phi}_N$ denote the rates of oxygen consumption by active tumour, quiescent tumour and normal cells respectively. We assume that oxygen is supplied through blood vessels at a rate $\bar{r}_V$, proportional to the difference between the extracellular oxygen and serum oxygen concentration C_S. Then we find

$$\frac{\partial C}{\partial t} - \frac{D_C}{R^2}\frac{\partial}{\partial R}\Big(R^2 \frac{\partial C}{\partial R}\Big) \tag{6.4}$$

$$= \begin{cases} -\Big((\bar{\phi}_A - \bar{\phi}_Q)\theta(C(t-t_0) - C_Q) + \bar{\phi}_Q\Big)K_M + \bar{r}_V V_M (C_S - C) & 0 < R < R_M \\ -\bar{\phi}_N K_N + \bar{r}_V V_N (C_S - C) & R_M < R, \end{cases}$$

where D_C is the oxygen diffusion coefficient, and K_N the normal tissue density. Now using the transformations $h = (C_X - C)/C_0$, $r = \bar{p}R$ and $\tau = t/\bar{T}$ where

$$\begin{aligned} &C_X = C_S - \frac{\bar{\phi}_N K_N}{\bar{r}_V V_N},\ C_0 = \frac{(\bar{\phi}_A - \phi_0)K_M}{\bar{r}_V V_N},\ \bar{p} = \sqrt{\frac{\bar{r}_V V_N}{D_C}}, \\ &\bar{T} = \frac{1}{\bar{r}_V V_N},\ \varepsilon = \frac{\bar{\phi}_Q - \phi_0}{\bar{\phi}_A - \phi_0},\ \phi_0 = \bar{\phi}_N \frac{K_N}{K_M}\psi^2,\ \tau_0 = \frac{t_0}{\bar{T}}, \\ &h_Q = \frac{C_X - C_Q}{C_0},\ \psi = \sqrt{\frac{V_M}{V_N}},\ r_M = \bar{p}R_M, \end{aligned} \tag{6.5}$$

we may recover Eq. (6.3). Note that this model only makes sense if $\bar{\phi}_A > \phi_0$, or equivalently $\bar{\phi}_A K_M/V_M > \bar{\phi}_N K_N/V_N$. If this effective rate of active tumour cell oxygen consumption is smaller than the corresponding normal rate, the tumour will receive sufficient oxygen supply, and no regions of hypoxia will occur. One minor difference between the two models is that for acid-induced quiescence we require $\varepsilon \geq 0$, whilst for hypoxia-induced quiescence no such restriction is in place.

Through the remainder of this chapter, we shall investigate the delay partial differential equation (6.3). This analysis will allow us to understand the effects of cellular quiescence on cyclical acidosis within tumour tissue.

6.2.1 Spatial homogeneity

We first consider the dynamics of Eq. (6.3) in the absence of diffusion. Assuming spatial homogeneity, within the tumour ($r < r_M$) we have

$$h_\tau = (1-\varepsilon)\theta(h_Q - h(\tau - \tau_0)) + \varepsilon - \psi^2 h. \tag{6.6}$$

To reduce the size of the parameter space, when the vascular density within the tumour is non-zero (i.e. $\psi > 0$), we may rescale the variables in Eq. (6.6) to obtain

$$\hbar_{\bar{\tau}} = (1-\varepsilon)\theta(\hbar_Q - \hbar(\bar{\tau} - \bar{\tau}_0)) + \varepsilon - \hbar, \tag{6.7}$$

where

$$\bar{h} = \psi^2 h,\ \bar{h}_Q = \psi^2 h_Q,\ \bar{\tau} = \psi^2 \tau,\ \bar{\tau}_0 = \psi^2 \tau_0. \tag{6.8}$$

If there is no lag time, i.e. $\bar{\tau}_0 = 0$, then this equation reduces to

$$\bar{h}_{\bar{\tau}} = (1-\varepsilon)\theta(\bar{h}_Q - \bar{h}) + \varepsilon - \bar{h}. \tag{6.9}$$

Looking for steady state solutions to Eq. (6.9), we see differing behaviours dependent on the value of $\bar{h}_Q$. If $\bar{h}_Q > 1$, then the unique steady state is given by $\bar{h} = 1$, whilst if $\bar{h}_Q < \varepsilon$ this steady state is given by $\bar{h} = \varepsilon$. However, if $\bar{h}_Q \in (\varepsilon, 1)$, Eq. (6.9) has no steady state solution. Interestingly in this case, $\bar{h}_{\bar{\tau}} > 0$ for $\bar{h} < \bar{h}_Q$ and $\bar{h}_{\bar{\tau}} < 0$ for $\bar{h} > \bar{h}_Q$, and thus $\bar{h}$ globally converges to $\bar{h}_Q$, even though it is not strictly a steady state solution.

We move on to consider Eq. (6.7) with a non-zero lag time $\bar{\tau}_0$. In determining typical parameter values, we assume as a base value $\psi^2 = 1$ i.e. waste removal occurs at the same rate in both normal and tumour tissue. Given experimentally-determined parameter values of $p = 4.7$ cm^{-1}, $H_0 = 10^{-2}$ mM and $D_H = 1.08 \times 10^{-5}$ cm^2 s^{-1} [41, 80, 92], we may calculate $T = 4.2 \times 10^3$ s, meaning that each time unit is equivalent to approximately one hour. Following Chapter 5, we take $\varepsilon = 0.01 \ll 1$, as quiescent cells are essentially metabolically-inactive, and $\bar{h}_Q = 0.04 \equiv$ pH 6.4 [92]. A change in cellular metabolism in response to a change in extracellular acidity is likely to be mediated by gene transcription and expression. Thus the lag time is likely to be on a similar timescale to that of gene transcription; as such we take $\bar{\tau}_0 = 0.5$, equivalent to a lag of $t_0 \approx 30$ minutes. Notice that with this parameter set we find $\bar{h}_Q \in (\varepsilon, 1)$, and thus from the analysis above there is no steady state and we would expect cyclical acidosis to occur.

For $\hbar_Q \in (\varepsilon, 1)$, Eq. (6.7) has analytical solution

$$\hbar = \begin{cases} 1 - (1 - \hbar_Q)e^{-\bar{\tau}} & \hbar \text{ increasing} \\ \varepsilon + (\hbar_Q - \varepsilon)e^{-\bar{\tau}} & \hbar \text{ decreasing.} \end{cases} \tag{6.10}$$

where $\bar{\tau}$ is shifted such that $\bar{\tau} = 0$ corresponds to $\hbar = \hbar_Q$. The maximum and minimum acid levels are given, respectively, by substituting $\bar{\tau} = \bar{\tau}_0$ above. The cycle time is given by

$$\bar{\tau}_c = \log\left[\left(e^{\bar{\tau}_0}\frac{1-\varepsilon}{\hbar_Q - \varepsilon} - 1\right)\left(e^{\bar{\tau}_0}\frac{1-\varepsilon}{1-\hbar_Q} - 1\right)\right]. \tag{6.11}$$

In Fig. 6.1 we present results for the spatially homogeneous model of tumour acidity, using the typical parameter values above. Cycles of acidosis are indeed observed; the acid levels vary between their maximum level of $\hbar \approx 0.42 \equiv$ pH 5.4 to their minimum level of $\hbar \approx 0.028 \equiv$ pH 6.5. The cycle time is $\bar{\tau} \approx 3.6$, equivalent to four hours.

6.2.2 Temporal homogeneity

Typically, the first step we take when investigating the role of a specific metabolite in tumour development is to look for temporally-homogeneous solutions to the metabolite evolution equation. The justification for this is that the timescale of metabolite diffusion is much less than the timescale of, for example, tumour growth, and hence the metabolite can be assumed to be in diffusive equilibrium. This removes the need for both the metabolite evolution term $\partial h/\partial\tau$ and the lag term τ_0, and is the same assumption we used in the previous chapter. However, the astute reader will have noticed that we considered only avascular ($\psi = 0$) growth in Section 5.3; the reasons for this will become clear below. Essentially, the previous chapter relied on the fact that acid levels increase towards

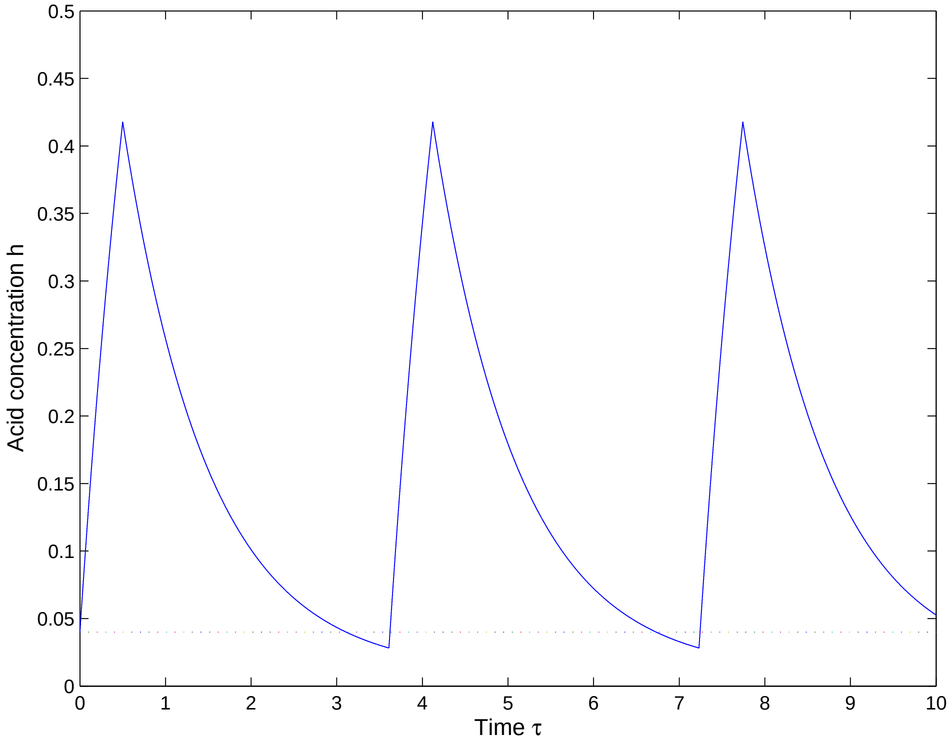

Figure 6.1: Results from Eq. (6.10). Predicted cyclical acidosis for the spatially-homogeneous model, using typical parameter values $\hbar_Q = 0.04$, $\varepsilon = 0.01$ and $\bar{\tau}_0 = 0.5$ and initial conditions $\hbar(t) = \hbar_Q$ for $\bar{\tau} \in [-\bar{\tau}_0, 0]$. The acid level cycles around $\hbar_Q$, between its maximum value of $\hbar \approx 0.42$ and minimum value of $\hbar \approx 0.028$. The cycle time is approximately 3.6 non-dimensional units.

the centre of the tumour. When considering a vascularised tumour ($\psi > 0$) containing quiescent cells, this property does not necessarily hold.

Assuming temporal homogeneity, Eq. (6.3) reduces to

$$r^2 h'' + 2rh' = \begin{cases} \psi^2 r^2 h - \big((1-\varepsilon)\theta(h_Q - h) + \varepsilon\big) r^2 & 0 < r < r_M \\ r^2 h & r_M < r, \end{cases} \tag{6.12}$$

where the primes denote the derivative with respect to r. To simplify the analysis, when $\psi > 0$ we may rescale the variables

$$\hbar = \psi^2 h, \ \ \hbar_Q = \psi^2 h_Q, \ \ \rho = \psi r, \ \ \rho_M = \psi r_M. \tag{6.13}$$

We may solve Eq. (6.12) for $r_M < r$; applying continuity of h and its derivative at r_M we find that within the tumour

$$\rho^2 \hbar'' + 2\rho \hbar' = \rho^2 \hbar - \big((1-\varepsilon)\theta(\hbar_Q - \hbar) + \varepsilon\big)\rho^2 \qquad 0 < \rho < \rho_M, \tag{6.14}$$

subject to the boundary conditions

$$\hbar'(0) = 0, \qquad \hbar'(\rho_M) = -\hbar(\rho_M)\frac{\rho_M + \psi}{\psi \rho_M}, \tag{6.15}$$

where the primes now denote derivative with respect to ρ.

We will now move on to show that, if $\hbar_Q \in (\varepsilon, 1)$ and ρ_M is sufficiently large, Eq. (6.14) has no solution. As such, the standard assumption that the substrate of interest is in diffusive equilibrium will be invalid, and cycles of limited substrate availability must be observed.

Consider first a tumour in which all cells are active. Then, from Eq. (6.14)

$$\rho^2 \hbar'' + 2\rho \hbar' - \rho^2 \hbar + \rho^2 = 0, \tag{6.16}$$

which, subject to the boundary conditions in Eq. (6.15) has solution

$$\hbar(\rho) = 1 - k_1 \frac{\sinh \rho}{\rho}, \tag{6.17}$$

where

$$k_1 = \frac{\rho_M + \psi}{\psi \cosh \rho_M + \sinh \rho_M}. \tag{6.18}$$

In particular

$$\hbar(0) = 1 - k_1 \to 1, \qquad \text{as } \rho_{\mathrm{M}} \to \infty. \tag{6.19}$$

Thus, if $\hbar_Q < 1$, at some radius $\rho_M = \rho^\star$, $\hbar(0) = \hbar_Q$ and the cells at the tumour centre will become quiescent. This radius $\rho^\star$ may be found numerically from the expression above for $h(0)$, i.e. through solution of

$$\rho^\star = (1 - \hbar_Q)(\psi \cosh \rho^\star + \sinh \rho^\star) - \psi. \tag{6.20}$$

For typical parameter values $\hbar_Q = 0.04$ and $\psi = 1$, we find $\rho^\star = 0.31$, equivalent to the first quiescent cells appearing when the tumour has radius $R \approx 0.7$ mm.

Assuming that $\rho > \rho^\star$, some of the tumour cells must be quiescent. Suppose $\hbar_Q \in (\varepsilon, 1)$ and consider a region (ρ_1, ρ_2) containing only quiescent cells, i.e. a region where $\hbar > \hbar_Q$ everywhere. Then, from Eq. (6.14) within this region

$$\rho^2 \hbar'' + 2\rho \hbar' - \rho^2 \hbar + \varepsilon \rho^2 = 0. \tag{6.21}$$

The edges of the region ρ_1 and ρ_2 must either be a tumour boundary (0 or ρ_M) and satisfy the appropriate boundary condition in Eq. (6.15) or they must satisfy $\hbar(\rho_i) = \hbar_Q$. We consider each case separately below.

- Case 1, $\rho_1 = 0$, $\rho_2 = \rho_M$.

Consider the case where all the cells in the tumour are quiescent. Then, applying the boundary conditions in Eq. (6.15),

$$\hbar(\rho) = \varepsilon(1 - k_1 \frac{\sinh \rho}{\rho}), \tag{6.22}$$

where, in particular

$$\hbar(0) = \varepsilon(1 - k_1) < \max(\varepsilon, 0) < \hbar_Q. \tag{6.23}$$

This contradicts the fact that the whole tumour is quiescent.

- Case 2, $\rho_1 = 0$, $\hbar(\rho_2) = \hbar_Q$.

Consider now the case where the quiescent cells are limited to the tumour centre. Then in $(0, \rho_2)$

$$\hbar(\rho) = \varepsilon + \left[(\hbar_Q - \varepsilon)\frac{\rho_2}{\sinh \rho_2}\right]\frac{\sinh \rho}{\rho}, \tag{6.24}$$

where, in particular

$$\hbar(0) = \varepsilon + (\hbar_Q - \varepsilon)\frac{\rho_2}{\sinh \rho_2} < \hbar_Q, \tag{6.25}$$

as $\rho_2/\sinh \rho_2 \in (0,1)$, again contradicting the fact that cells at the tumour centre are quiescent.

- Case 3, $\hbar(\rho_1) = \hbar_Q$.

Suppose finally that the cells in the tumour centre $(0, \rho_1)$ are active ($\hbar < h_Q$) and surrounded by quiescent cells. Then $\hbar(\rho_1) = \hbar_Q$ and, in $(0, \rho_1)$,

$$\hbar(\rho) = 1 - \left[(1 - \hbar_Q)\frac{\rho_1}{\sinh \rho_1}\right]\frac{\sinh \rho}{\rho}, \tag{6.26}$$

where, in particular

$$\hbar(0) = 1 - (1 - \hbar_Q)\frac{\rho_1}{\sinh \rho_1} > \hbar_Q, \tag{6.27}$$

contradicting the fact that the cells at the tumour centre are active.

The analysis presented above has shown that, when $\psi r = \rho > \rho^\star$ and $\psi^2 h = \hbar \in (\varepsilon, 1)$, Eq. (6.12) has no solution. As such, the standard assumption of temporal homogeneity is not valid; instead we must consider the temporal dynamics of the system. In the previous section we showed that when $\hbar \in (\varepsilon, 1)$, the assumption of spatial homogeneity leads to cyclical solutions. Given this evidence, for the full model defined in Eq. (6.3), we expect cyclical behaviour to occur whenever $\rho > \rho^\star$ and $\hbar \in (\varepsilon, 1)$. This behaviour is analysed in the next section.

6.2.3 Full model analysis

We move on to analyse the full model, including both temporal and spatial dynamics. The model is defined by Eq. (6.3), which we reiterate here

$$h_\tau - (h_{rr} + 2h_r/r) = \begin{cases} (1-\varepsilon)\theta(h_Q - h(\tau - \tau_0)) + \varepsilon - \psi^2 h & 0 < r \leq r_M \\ -h & r_M < r, \end{cases} \tag{6.28}$$

subject to the boundary conditions $h_r(0, \tau) = 0$, continuity of h and h_r at $r = r_M$ and $\lim_{r\to\infty} h(r, \tau) = 0$, and initial conditions $h(r, \tau) = 0$ for $\tau \in [-\tau_0, 0]$

The method of lines [86] is a technique that may be applied to numerically solve parabolic equations, involving discretising in all but one dimension, and then integrating the semi-discrete problem as a system of ordinary differential equations (ODEs). The method allows us to take advantage of the sophisticated tools available for numerical solution of ODEs and, in this case, delay (ordinary) differential equations (DDEs).

We discretise Eq. (6.28) with respect to the variable r using finite differences, in particular using the approximations

$$\begin{aligned} h_r(r,\tau) &\approx \frac{h(r+\Delta,\tau)-h(r-\Delta,\tau)}{2\Delta} \\ h_{rr}(r,\tau) &\approx \frac{h(r+\Delta,\tau)+h(r-\Delta,\tau)-2h(r,\tau)}{\Delta^2}, \end{aligned} \tag{6.29}$$

for small Δ.

To use the discretisation above, we first approximate the infinite domain $[0,\infty)$ as a finite domain $[0,r_\infty]$, where $r_\infty = kr_M$ for some integer $k>1$. The boundary condition at $r=\infty$ is then replaced by the condition $h(r_\infty,\tau)=0$. We then choose a uniform grid r_j, $j=1,\ldots,kN$ with spacing $\Delta = r_\infty/kN = r_M/N$ such that $r_j = j\Delta$. This allows us to define $h_j(\tau) = h(r_j,\tau)$ to be the value of h at each of these grid points.

The Dirichlet boundary condition $h(r_\infty,\tau)=0$ is handled easily by defining $h_{kN}(\tau) = 0$. The Neumann boundary condition $h_r(0,\tau)=0$ requires more care. We first apply l'Hôpital's rule to obtain

$$\lim_{r\to 0}\frac{h_r(r,\tau)}{r} = \lim_{r\to 0}\frac{[h_r(r,\tau)]_r}{[r]_r} = h_{rr}(0,\tau). \tag{6.30}$$

To handle this second order difference, imagine the problem is instead being solved on the domain $[-r_\infty,r_\infty]$, with the tumour tissue confined to $[-r_M,r_M]$ and the same boundary conditions at $r=\pm r_\infty$. The Neumann boundary condition then implies that the solution will be symmetric with respect to r for all time. Thus $h(-\Delta,\tau)=h(\Delta,\tau)$, so $h_{-1}(\tau) = h_1(\tau)$.

The system of $(kN+1)$ DDEs in the variable τ is then given by

$$h_j' = \begin{cases} 6\Big[h_1 - h_0\Big]\Delta^{-2} + f_0 & j = 0 \\ \Big[(1+j^{-1})h_{j+1} + (1-j^{-1})h_{j-1} - 2h_j\Big]\Delta^{-2} + f_j & j = 1, \ldots, N \\ \Big[(1+j^{-1})h_{j+1} + (1-j^{-1})h_{j-1} - 2h_j\Big]\Delta^{-2} - h_j & j = N+1, \ldots, kN-1 \\ 0 & j = kN, \end{cases} \tag{6.31}$$

where

$$f_j(\tau) = (1-\varepsilon)\theta(h_Q - h_j(\tau - \tau_0)) + \varepsilon - \psi^2 h_j(\tau). \tag{6.32}$$

The system of DDEs in (6.31) is solved using the `MATLAB`® integrator `dde23` [106]. Preliminary tests showed that $k = 5$ was a suitable choice – integrating over domains larger than $[0, 5\,r_M]$ had a negligible effect on the system solution.

Typical model solutions are shown in Figs. 6.2 and 6.3. Given typical parameter values of $h_Q = 0.04$ and $\psi = 1$, we may calculate from Eq. (6.20) $r^\star = \rho^\star/\psi = 0.31$, the tumour radius at which quiescence first occurs. Choosing $r_M = 1 > r^\star$ and $\varepsilon = 0.01$, we have $\psi^2 h_Q \in (\varepsilon, 1)$, and thus, from previous analyses, cyclical acidosis will occur.

Fig. 6.2 shows cyclical acidity at the tumour centre (red) and tumour edge (blue) using these parameter values. The cells at the tumour centre cycle between their maximum level of $h \approx 0.23 \equiv$ pH 5.6 and their minimum level $h \approx 0.016 \equiv$ pH 6.7. The cells at the tumour edge also experience cyclical acidity about the quiescence threshold, though their maximum acidity $h \approx 0.11 \equiv$ pH 5.9 is less than the cells at the centre. The cycle time is $\tau \approx 1.4$, equivalent to 100 minutes. This may be compared to the spatially homogeneous model presented in Fig. 6.1. Addition of diffusion to the model acts to smooth system

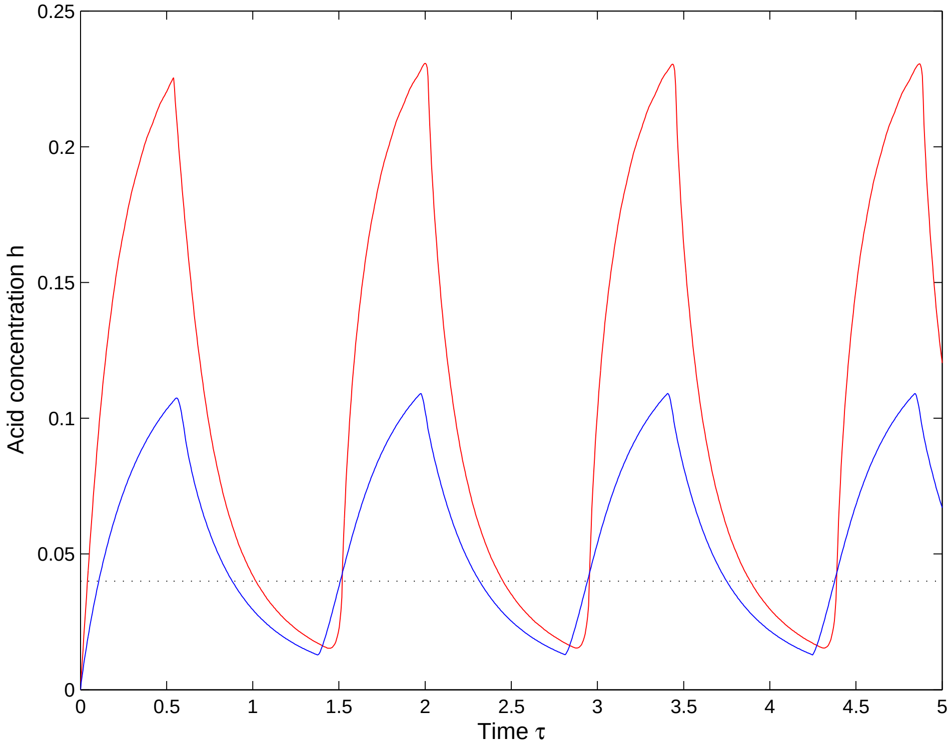

Figure 6.2: Results from Eq. (6.31). Predicted cycles of acidity observed at the tumour centre (red) and tumour edge (blue) for the full model, using typical parameter values $h_Q = 0.04$, $\varepsilon = 0.01$, $\psi = 1$, $\tau_0 = 0.5$ and $r_M = 1$. The domain of integration used is $[0, 5\,r_M]$, divided into 251 grid points. The acidity levels cycle around the quiescence threshold h_Q, with cycle time of approximately 1.4 units.

dynamics, reducing the maximum acidity levels seen and in turn decreasing the acid cycle time.

In Fig. 6.3 we investigate how acidity levels vary through the tumour during each cycle. Initially (blue), all the cells within the tumour are below the quiescence threshold. Cycles of acidity are out of phase for different sections of the tumour and an increase in acidity is first seen at the tumour edge ($r = 1$, red). Acidity then increases at the tumour centre ($r = 0$, black), before reaching its maximum level (green). This figure demonstrates that, whilst acid levels are on average higher in the tumour centre than the tumour edge, this

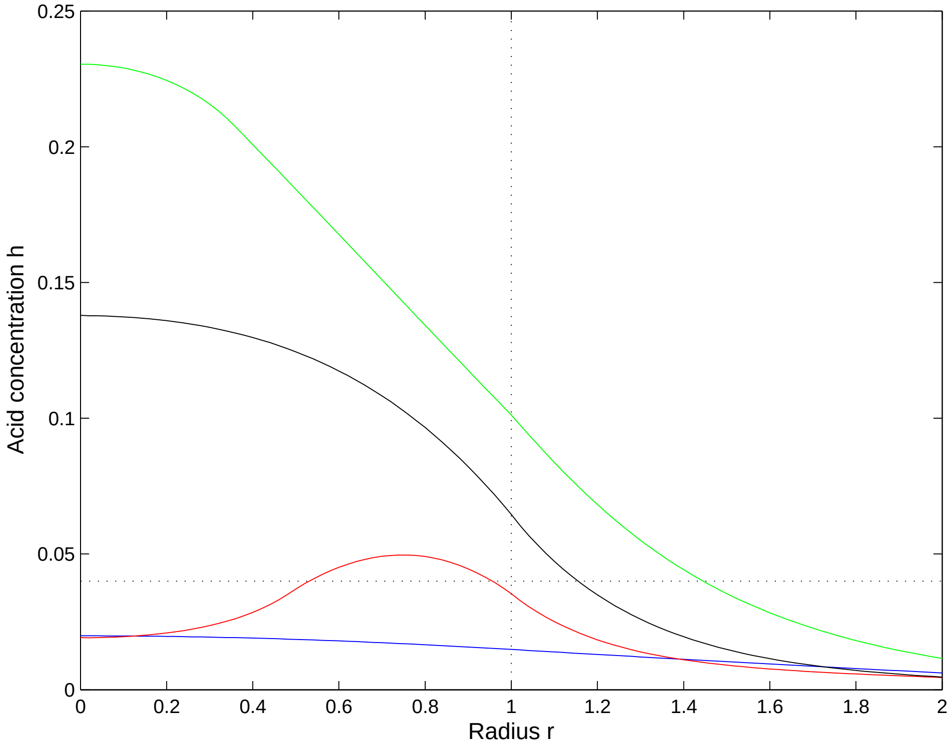

Figure 6.3: Changing acid profiles in and around the tumour during the acidosis cycle as depicted in Fig. 6.2. Times shown are $\tau = 1.3$ (blue), $\tau = 1.5$ (red), $\tau = 1.6$ (black) and $\tau = 2.0$ (green). Notice that for some of this cycle, acidity is higher at the tumour edge than centre. Parameter values used are as in Fig. 6.2. The dotted lines represent the tumour radius ($r_M = 1$) and quiescence threshold ($h_Q = 0.04$).

property does not hold throughout the acid cycle. The point is reinforced in Fig. 6.4, which shows how the metabolic characteristics of tumour cells vary during each cycle. The first cells to become quiescent due to high extracellular acidity are not at the tumour centre, rather this occurs at $r \approx 0.81$ near the edge of the tumour.

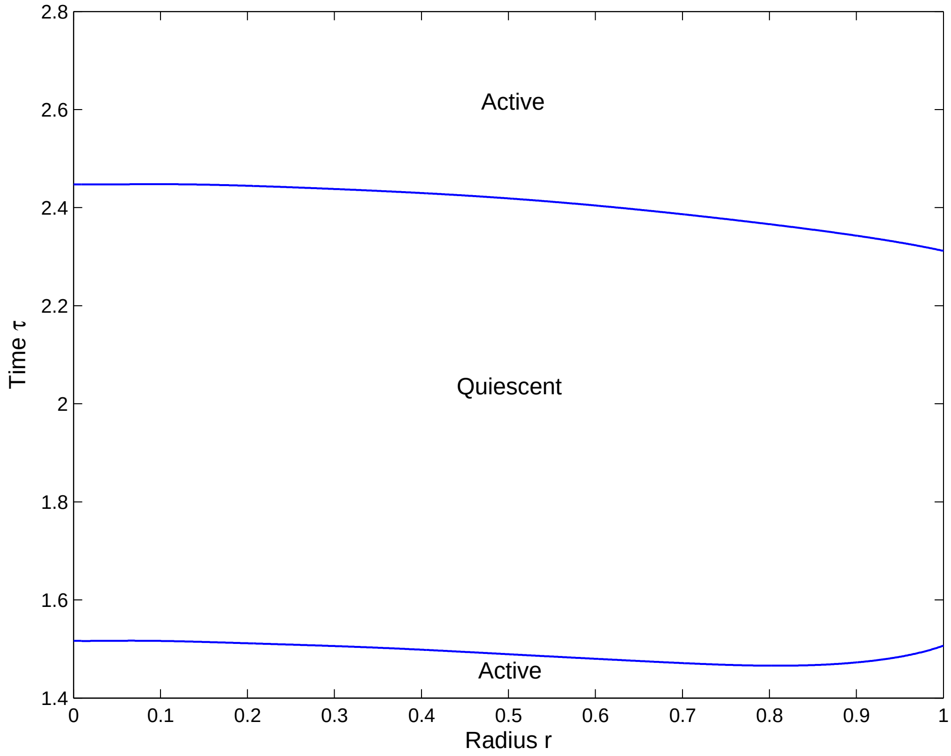

Figure 6.4: Changing metabolic characteristics during the acidosis cycle as depicted in Figs. 6.2 and 6.3. The first cells to become quiescent are located at $r \approx 0.81$, whilst the first cells to resume proliferation are at the tumour edge, $r = 1$. For the majority of the cycle, the whole of the tumour is in the same metabolic state, with all cells either active or quiescent. Parameter values used are as in Fig. 6.2.

6.3 Discussion

Fluctuations in metabolite levels are known to occur within tumours with discrete periodicities of hours, minutes and days. Cells that are best suited to respond to these periods of cellular stress, such as through constitutive upregulation of aerobic glycolysis, will be positively selected by somatic evolutionary forces. These cycles are assumed to occur due to haemodynamic variations such as changes in the local concentration of red blood cells or structural rearrangement of blood vessels. In this chapter we have investigated a further hypothesis, namely that quiescence in response to cellular stress, and the corresponding drop in metabolism, provides a negative feedback mechanism capable of reproducing such metabolite cycles.

A simple reaction-diffusion system is used to describe the evolution of the metabolite of interest. Whilst we focus on the dynamics of acidity within the tumour, the model is equally valid for any growth inhibitor produced by tumour cells or any growth promoter consumed by tumour cells. The model is similar to that used in Chapter 5, with the addition of temporal dynamics and a lag term corresponding to gene transcription and expression.

We show, for a biologically realistic range of parameter values ($r_M > r^\star$ and $\psi^2 h_Q \in (\varepsilon, 1)$), that the standard assumption of the metabolite reaching diffusive equilibrium is not valid. Rather, when investigating the distribution of acid around a vascularised tumour in which cellular quiescence occurs, temporal dynamics must be considered.

We first investigate a spatially homogeneous model, and find that cycles of acidity due to cellular quiescence occur with a periodicity of around four hours. Inclusion of spatial aspects and diffusion reduces this cycle time to between one and two hours, consistent with experimental evidence [58]. Within the parameter regime used here we find the acid levels at the tumour centre will fluctuate between pH 6.7 and pH 5.6. Given the importance of acidic and hypoxic cycles in mediating the evolution of cancer cell metabolism and resistance to acidity, further experimental verification of the role of quiescence in inducing metabolic cycles will be of considerable interest.

Chapter 7

pH imaging

7.1 Introduction

The relatively young field of molecular imaging is focused on the *in vivo* characterisation and measurement of biological processes at the cellular and molecular level. In contrast to 'classical' diagnostic imaging, it probes the molecular abnormalities that are the basis of disease, rather than imaging the end effects of these molecular alterations. Specific imaging of such targets allows earlier detection and characterisation of disease, earlier and direct molecular assessment of treatment effects, and a more fundamental understanding of the disease process.

The measurement of extracellular pH of tumours *in vivo* has historically been performed using microelectrodes [118]. This approach has the disadvantage of being both invasive and destructive. Over the past two decades, noninvasive magnetic resonance (MR) techniques have been developed to measure both intracellular pH ($\mathrm{pH_I}$) and extracellular pH ($\mathrm{pH_X}$) of human and animal tissues [48, 49]. Virtually all tumour pH data to date show an acidic $\mathrm{pH_X}$ and alkaline $\mathrm{pH_I}$ relative to normal tissue. Moreover, it is found that the

Tumour	Species	Type	pH_X	pH_I
Normal	Rat	Liver	7.34 ± 0.03	7.26 ± 0.02
Normal	Rat	Muscle	7.39	7.39 ± 0.10
MCF-7	Human	Breast	6.99 ± 0.11	7.15 ± 0.08
MDA-mb-435	Human	Breast	6.80 ± 0.11	7.37 ± 0.07
MDA-mb-435/nm23-H1	Human	Breast	7.17 ± 0.10	7.16 ± 0.05
HT-29	Human	Colon	6.79 ± 0.05	7.02 ± 0.05

Table 7.1: Extracellular and intracellular human and animal tumour pH, measured with ^{31}P magnetic resonance spectroscopy [49].

pH_X becomes more acidic as the tumour grows, consistent with reduced perfusion [49]. In Table 7.1, we present a sample of the data as measured using ^{31}P MR spectroscopy. Significant differences in tumour pH_X have been found that correlate with the aggressiveness of the tumour cell phenotype. For example, breast cancer tumours expressing nm23, a metastasis-inhibiting protein, had significantly higher pH_X and lower pH_I compared to their metastatic counterparts. Similarly, tumours of highly metastatic cells, such as MDA-mb-435, have a lower pH_X than non-metastatic MCF-7 tumours of comparable size.

Most recently we have witnessed the development of pH-sensitive gadolinium complexes, offering the possibility of imaging pH with a spatial resolution comparable to that of standard MR imaging. Through sequentially administering two contrast agents with similar tissue pharmacokinetics, one insensitive to tissue pH and the other pH-sensitive, it has been possible to compute pH images of kidneys and nearby tissues following renal acidosis [97].

In the long term, clinical applications of this emergent high-resolution tumour pH imaging technology can be envisioned, including the characterisation of tumours and the assessment of chemotherapy. The extraction of key biological parameters from such images could prove invaluable to the clinician as a diagnostic tool, for example in determining whether a given tumour is benign or cancerous.

In this chapter we undertake a comparison between tumour pH images obtained through optical imaging techniques to the reaction-diffusion model of acid dynamics set out in previous chapters. The motivations behind this are two-fold. Firstly, the analysis will allow us to assess and verify the previous modelling work, giving the mathematics a firm biological foundation. Secondly, we aim provide a methodology for calculating cellular acid production rates from pH images – an important parameter known to correlate with tumour aggressiveness [81].

7.2 Fluorescence data

The data used in this chapter have been provided by collaborators at the University of Arizona. The data are extracted from eight tumours implanted in severe combined-immuno-deficient (SCID) mice. These SCID mice have no immune system, allowing the foreign tumour cells to invade. Each of the eight data sets consists of three pH images, taken approximately one, two and three weeks after tumour implantation, making a total of 24 images. The tumour cell line used, PC3N/eGFP, is a rapidly growing human prostate cancer, modified to express green fluorescent protein (GFP). Each tumour pH image has a corresponding GFP image, allowing detection of the tumour cells. Each image contains 512×512 pixels, with a spatial resolution of 25 μm. An example of a typical pH–GFP image pair is given in Fig. 7.1.

The pH profile is created using a technique known as fluorescence ratio imaging. Fluorescence occurs when a molecule absorbs a photon, then emits a photon of slightly longer wavelength. This simple concept has been used in a wide variety of applications in biology and medicine. The tumour was injected with the pH-sensitive fluorescent dye seminaphthorhodofluor-1 (SNARF-1) prior to image acquisition. Two sets of emission data were then collected in different spectral regions (red and blue). Using a suitable transformation, the ratio of the two intensities at each point was used to calculate the pH as in Fig. 7.1 (a). This method was shown to yield a pH resolution of 0.042 pH units [64]. Examination of a third spectral region (green), allows us to view the emission of the GFP used to locate the tumour, as shown in Fig. 7.1 (b). Note that the GFP image has been scaled here so that 1 corresponds to the intensity threshold used by the experimentalists to identify the tumour edge [64].

It should be noted that, in order to perform the optical imaging technique described above, a dorsal skin fold chamber must be attached to the mouse (see Fig. 7.2). The dorsal skin is a flap of tissue on the back of the mouse. This tissue is clamped inside a thin window chamber, and the skin is then removed, exposing the smooth muscle tissue and allowing the implanted tumour to be viewed. The circular window of the chamber can also be clearly seen at the edge of both the pH and GFP profiles in Fig. 7.1.

Because of these experimental methods, this fluorescence imaging technique is suitable only for animal models, rather than in a clinical setting. Nonetheless, the methods of analysis presented below will apply to any imaging modality capable of producing pH profiles around a tumour, such as the MR imaging discussed in the Introduction.

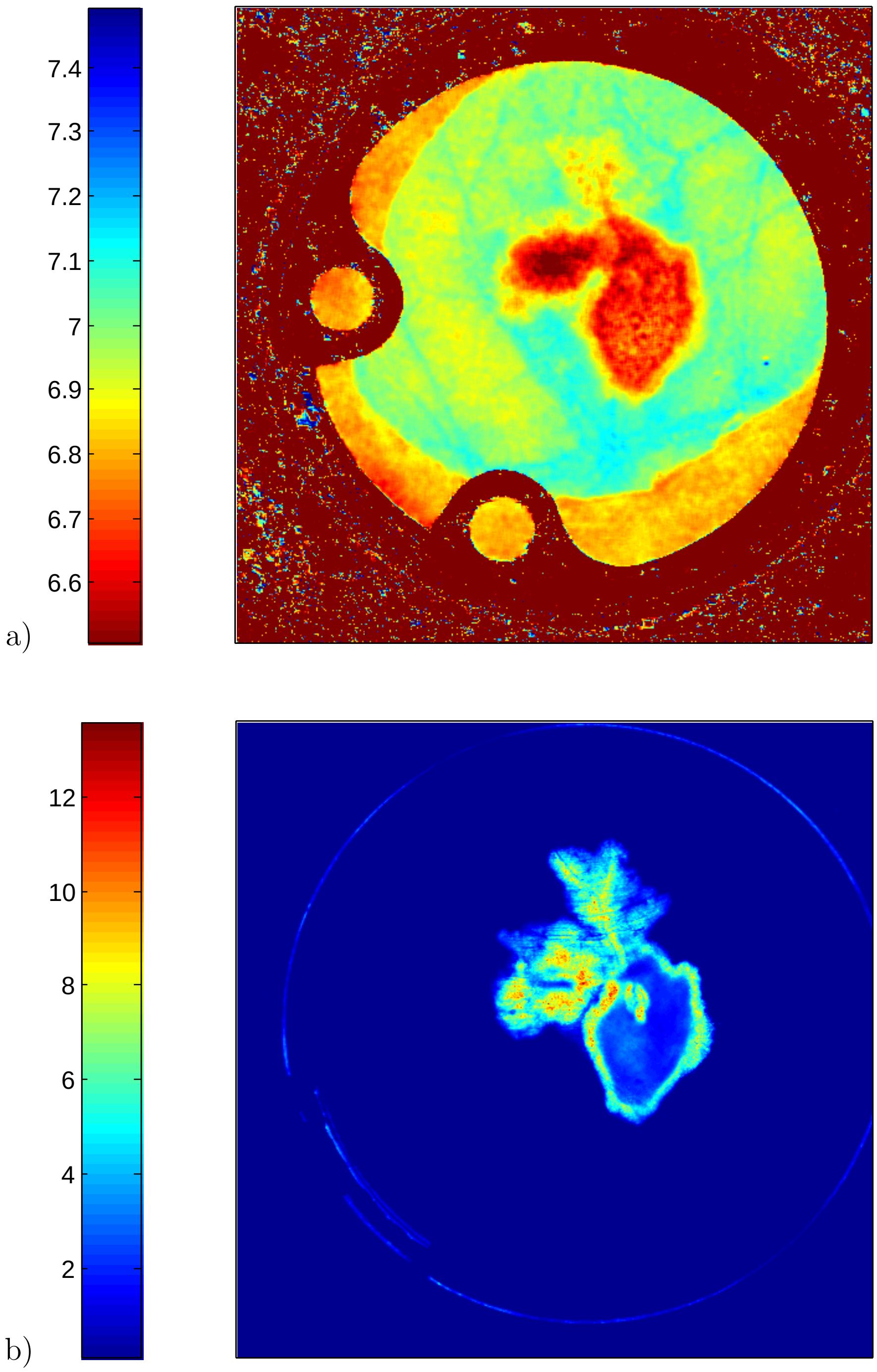

Figure 7.1: (a) Typical pH profile of tumour and surrounding tissue obtained through SNARF-1 fluorescence ratio imaging. (b) Corresponding GFP profile of tumour. The field of view is $(12.74\text{mm})^2$.

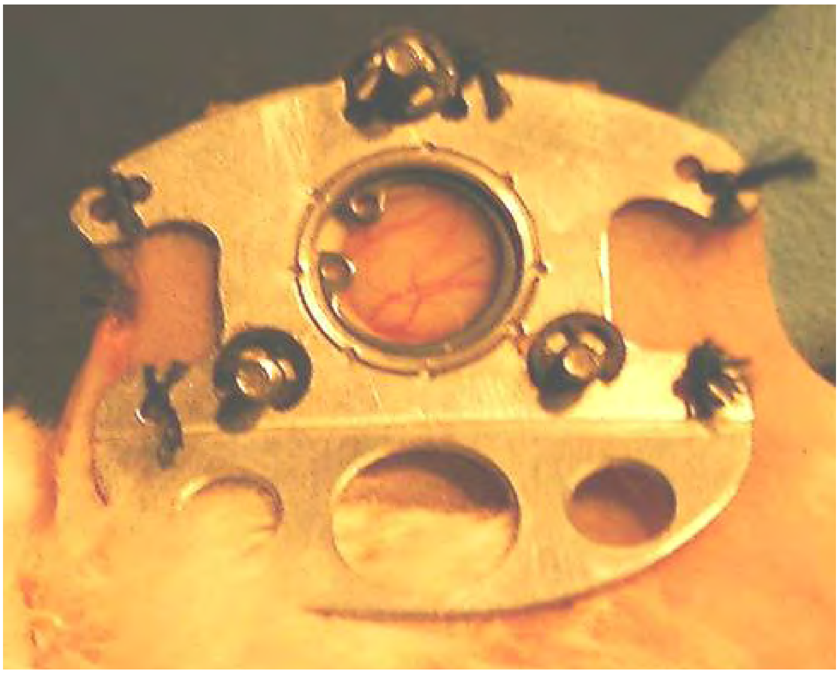

Figure 7.2: Dorsal skin fold chamber. Figure courtesy of R. Gatenby.

7.3 Image analysis

7.3.1 Preprocessing

Determining the ROI

Before undertaking a comparison between the models and experimental data, the images must be preprocessed. Returning to Fig. 7.1 (a), we see some artefacts of the experimental approach that must be removed before analysis can be performed. The region of interest (ROI) of the image is the tumour and its surrounding smooth muscle tissue, which has a pH of approximately 7 (green). Other than this region, the image shows points outside the circular window, which are the metal casing of the window chamber. These points have a speckled appearance, with some pixels having very high or very low apparent pH.

The image also shows an area of low apparent pH (orange) just inside the window; this is skin that has regrown or slipped into view.

In order to remove the artefacts and show only the ROI – the tumour and surrounding smooth muscle tissue – we use the method presented pictorially in Fig. 7.3. The method is based essentially on removing regions of the image that have a low pH. Since the tumour itself has a low pH and we do not wish to remove it from the processed image, the first step is to set all pixels with a non-zero GFP level to have a high pH (Fig. 7.3 (b)). This has the effect of removing the cells within the tumour, as well as a ring of cells at the edge of the image. The next step is to apply an erosion–dilation filter (Fig. 7.3 (c)). Erosion works by replacing each pixel's pH by the minimum pH in a specified neighbourhood of that pixel, where we choose the neighbourhood to be a disc of radius R pixels. This is followed by a dilation, which works in the same way except that the maximum pH in the neighbourhood is taken. The erosion–dilation filter modifies the intensity values in the image, but does not affect the overall geometry.

There is now a clear delineation between the different regions within the image. Thus we may threshold the image to extract all pixels where $\mathrm{pH} < \mathrm{pH_c}$ (Fig. 7.3 (d)), and then the region of interest is given by the central 'hole' (Fig. 7.3 (e)). The final panel (Fig. 7.3 (f)) shows the ROI plotted on the original pH image. Also highlighted is the tumour edge as found from the GFP image.

Scaling

Let $\bar{P}$ denote the experimental pH profile, $\bar{G}$ the GFP profile and let $\bar{H} = 10^{-\bar{P}}$ denote the hydrogen ion concentration. Because we are dealing with micromolar concentrations

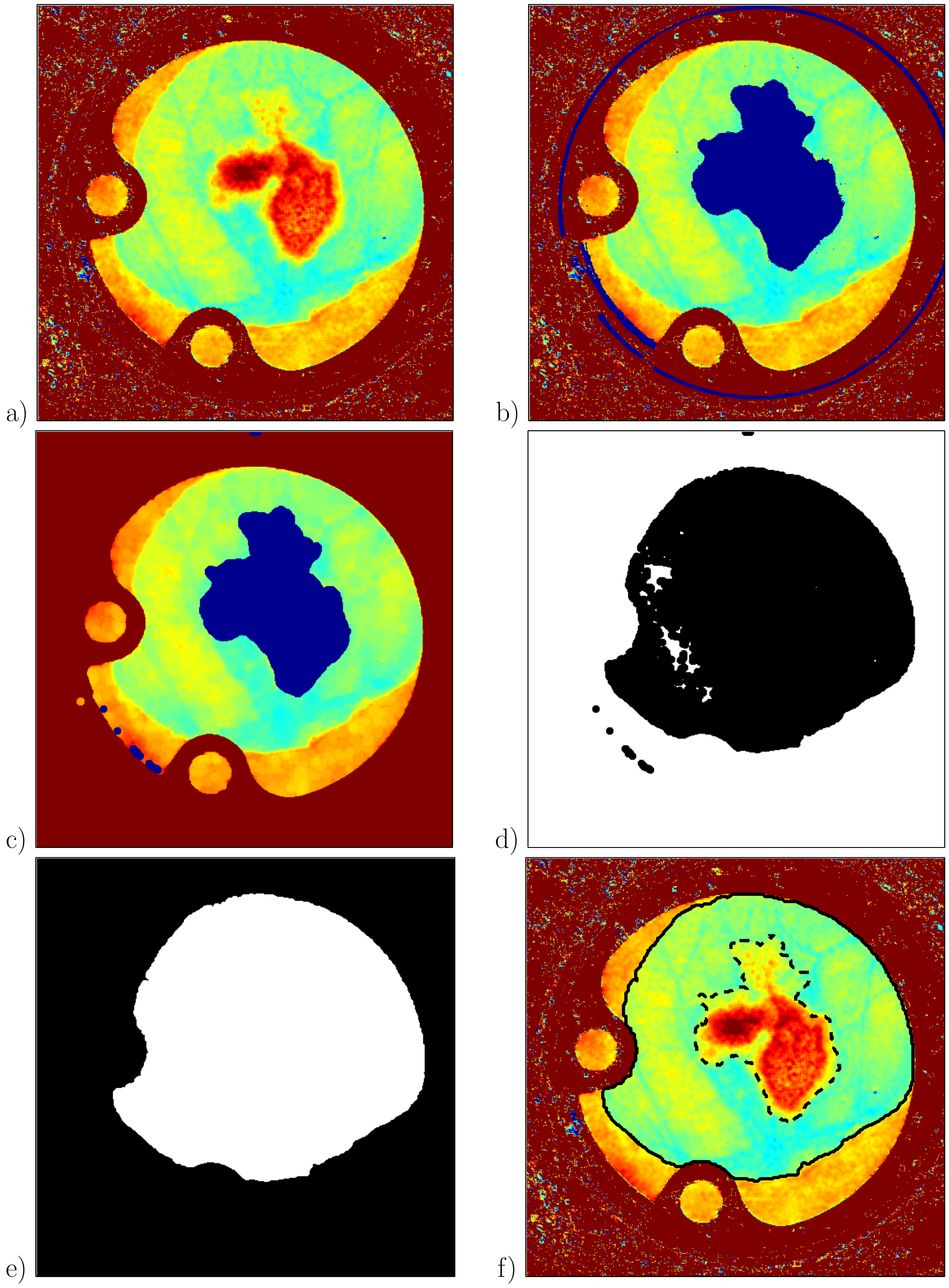

Figure 7.3: Method for determining the ROI of the pH image. (a) Initial tumour pH image. (b) Removal of tumour. (c) Erosion-dilation filter with $R = 5$. (d) Thresholding the image with $\mathrm{pH_c} = 6.9$. (e) Extracting the critical region. (f) The ROI (solid line) plotted on the original pH image, with the tumour boundary also highlighted (dashed line).

of hydrogen ions over micrometre distances, it is important to scale the variables to avoid computational problems associated with very small numbers.

We non-dimensionalise:

$$\hbar = \frac{\bar{H}}{H_0}, \ \xi = \frac{x}{\Delta}, \ \bar{g} = \max(\bar{G} - 1, 0), \tag{7.1}$$

where we choose $H_0 = 10^{-7.25}\mathrm{M} \equiv \mathrm{pH}\ 7.25$ and $\Delta = 25\ \mu\mathrm{m}$ is the pixel width. Under these scalings, the hydrogen ion concentration and distance variables $\hbar$ and ξ are non-dimensional and of order unity. As mentioned earlier, the tumour tissue is defined as all points where $\bar{G} > 1$. By performing the shift above, the tumour tissue is redefined as all points where $\bar{g}$ is non-zero.

7.3.2 Parameter estimation

Having performed the necessary preprocessing, we are now in a position to compare the experimental data to the modelling work discussed in previous chapters.

Let $\hbar$ denote the experimental hydrogen ion profiles, $\bar{g}$ the GFP profile and Ω_R the region of interest as calculated above. The viable tumour tissue Ω_M is defined to be all points $\underline{x} \in \Omega_R$ such that $\bar{g}(\underline{x}) > 0$, and all points surrounded by tumour tissue. In this way, debris within the tumour not expressing GFP will still be considered part of the tumour.

Returning now to Eq. (5.1), we assumed that the evolution of the model hydrogen ion profile H may be described by a reaction-diffusion equation:

$$\frac{\partial H}{\partial t} = r_H M - r_V V(H - H_X) + D_H \nabla^2 H \tag{7.2}$$

where r_H is the rate of tumour cell acid (hydrogen ion) production, M the tumour cell density, r_V the rate of acid removal through blood vessels in normal tissue, V the vascular density, H_X the normal extracellular hydrogen ion concentration, and D_H the acid diffusion coefficient. The boundary condition is that $H \to H_X$ a long distance from the tumour. This equation was analysed in Section 5.2, for the case of a spherically-symmetric tumour.

In order to compare the model of hydrogen ion evolution given in Eq. (7.2) to the experimental pH images, a number of simplifying assumptions must be made. Whilst we do not know the tumour cell density M, it may sensibly approximated as proportional to the level of GFP expression, $M = k_g \bar{g}$. The vascular density V is also not known. In reality tumour tissue is initially avascular, with tumour vessel density increasing with growth through angiogenesis mechanisms. However, in the absence of precise information, we assume that there exists a region Ω_V where the vessels exist homogeneously at their carrying capacity ($V = K_V$), and that the remaining tissue is avascular ($V = 0$). Finally, we assume that the acid reaches equilibrium over the timescale of tumour growth, i.e. $\partial H/\partial t = 0$. However, as was shown in Chapter 6, this assumption may not be valid for a particular parameter range. With these reservations in mind and under the assumptions stated above, in non-dimensional form Eq. (7.2) becomes

$$\theta_1 \bar{g} + (\theta_2 - h)\Big\rfloor_{\Omega_V} + \theta_3 \nabla_\xi^2 h = 0, \tag{7.3}$$

where

$$h = \frac{H}{H_0},\ \theta_1 = \frac{r_H k_g}{r_V K_V H_0},\ \theta_2 = \frac{H_X}{H_0},\ \theta_3 = \frac{D_H}{r_V K_V \Delta^2}\ . \tag{7.4}$$

The notation $f(\underline{x})\Big\rfloor_{\Omega}$ is used to represent taking the value $f(\underline{x})$ if $\underline{x} \in \Omega$, and 0 otherwise. As boundary conditions, we take the hydrogen ion concentration at the edge of the region of interest to be fixed at the background level, $H(\delta\Omega_R) = \theta_2$.

It remains to define the unknown region of vascularity Ω_V, for which we investigate three possibilities. We first consider the tumour to be avascular, $\Omega_V = \Omega_R - \Omega_M$. We also take the tumour to be fully vascularised $\Omega_V = \Omega_R$. In Chapter 5, we considered a third possibility, a partially vascularised tumour – the vasculature exists homogeneously throughout the tumour, except for in the necrotic core. Thus $\Omega_V = \Omega_R - \Omega_D$, where $\Omega_D \subset \Omega_M$ denotes the necrotic region. Whilst we do not have precise information about the areas of necrosis within the tumour, this region may be estimated from the data available. Noting that necrotic debris will be expressing significantly less GFP than the surrounding, viable tissue, we empirically define $\Omega_D^\star = \{\underline{x} \in \Omega_M : \bar{g}(\underline{x}) > \max(\bar{g})/4\}$. We then take Ω_D to be all pixels surrounded by, but not in $\Omega_D^\star$.

For a given parameter set $\Theta = (\theta_1, \theta_2, \theta_3)$, the solution $h = h_\Theta$ to Eq. (7.3) may be found through first making a finite difference approximation.

$$\nabla_\xi^2 h(x,y) \approx h(x+1,y) + h(x-1,y) + h(x,y+1) + h(x,y-1) - 4h(x,y). \tag{7.5}$$

Then Eq. (7.4) reduces to a system of N linear equations, using the same methods as Chapter 4, where $N \sim 10^5$ denotes the number of pixels within the region of interest Ω_R.

The full parameter estimation problem to compare an experimental image $\hbar$ with our model Eq. (7.3) may be described as:

> Find $\Theta = (\theta_1, \theta_2, \theta_3)$ to minimise $\|d\|_R$ where $d = h_\Theta - \hbar$, $\hbar$ is the experimental image, h_Θ is the solution to Eq. (7.3) and $\|.\|_R$ denotes RMS norm.

This inverse problem is computationally expensive as it requires multiple solutions of Eq. (7.3) for different parameter estimates Θ. Moreover, three-dimensional minimisation routines suffer from a number of problems, including convergence to local, rather than global, minima. However, through a suitable transformation, it may be reduced to a one-dimensional minimisation problem.

Suppose first that we fix θ_3. We may calculate the solution $h^\star$ to the equation

$$\bar{g} - h^\star \rfloor_{\Omega_V} + \theta_3 \nabla^2 h^\star = 0, \tag{7.6}$$

subject to the boundary condition $h^\star(\delta\Omega_R) = 0$, using the finite difference approximation outlined above. Then the solution to Eq. (7.3) is given by $h = \theta_1^{-1} h^\star + \theta_2$. Thus, for fixed θ_3, the problem reduces to finding θ_1 and θ_2 to minimise $\left\|\theta_1^{-1} h^\star + \theta_2 - \hbar\right\|_R$. This is now a simple linear least squares problem. Writing

$$\begin{aligned}
\sigma_{xx} &= \sum_{\bar{\xi} \in \Omega_R} \left(h^\star(\bar{\xi}) - h^\star_\mu\right)^2, \\
\sigma_{yy} &= \sum_{\bar{\xi} \in \Omega_R} \left(\hbar(\bar{\xi}) - \hbar_\mu\right)^2, \\
\sigma_{xy} &= \sum_{\bar{\xi} \in \Omega_R} \left(h^\star(\bar{\xi}) - h^\star_\mu\right)\left(\hbar(\bar{\xi}) - \hbar_\mu\right),
\end{aligned} \tag{7.7}$$

where $h^\star_\mu$ and $\hbar_\mu$ are the means of $h^\star$ and $\hbar$, respectively, the best fit solution is given by

$$\theta_1^{-1} = \frac{\sigma_{xy}}{\sigma_{xx}}, \; \theta_2 = \hbar_\mu - \theta_1^{-1} h^\star_\mu, \tag{7.8}$$

and the RMS fit by

$$\|\cdot\|_R = \sqrt{\frac{\sigma_{xx}\sigma_{yy} - \sigma_{xy}^2}{|\Omega_R|\,\sigma_{xx}}}. \tag{7.9}$$

Thus we reduce the parameter fitting routine to the one-dimensional problem of finding θ_3 to minimise the RMS difference defined in Eq. (7.9).

Unlike multi-dimensional problems, minimisation in one dimension is well understood and does not suffer to such an extent from convergence to local minima. The Golden Section search is one method for minimising functions on a bounded interval [36]. Note from Eq. (7.3) that θ_3 must be strictly positive, as if $\theta_3 = 0$, h is not defined outside of the vascular region Ω_V. Note also from Eq. (7.3) that $d = \ln 2\sqrt{\theta_3}$ represents the number of pixels away from the tumour edge at which the excess hydrogen ion concentration falls to half its level. We choose the bounded interval $d \in [0.1, 40]$ as, for $d < 0.1$ pixels, the spatial resolution of the images will not be able to detect the acid gradient; $d > 40 \equiv 1$ mm is beyond the expected diffusion distance for the acid gradient. Converting these bounds for d to θ_3, we perform the Golden Section search on the interval $\theta_3 \in [0.02, 3000]$. The results of the parameter estimation process are given in the next section.

7.4 Results

The parameter estimation algorithm was run for each of the 24 pH images. In Fig. 7.4 we present the predicted pH profiles for the tumour shown in Fig. 7.1, for each of the three levels of tumour vascularity: avascular ($\Omega_V = \Omega_R - \Omega_M$), partially vascularised ($\Omega_V = \Omega_R - \Omega_D$) and fully vascularised ($\Omega_V = \Omega_R$). Fig. 7.4 (a) shows the experimental pH image within the region of interest. Figs. 7.3 (b), (c) and (d) show the predicted pH profiles under the assumptions of an avascular (RMS $= 7.11 \times 10^{-2}$ pH units), partially vascular (RMS $= 7.06 \times 10^{-2}$ pH) and fully vascular tumour (RMS $= 8.56 \times 10^{-2}$ pH), respectively.

Comparing the experimental and predicted pH profiles, we see that the model is unable to

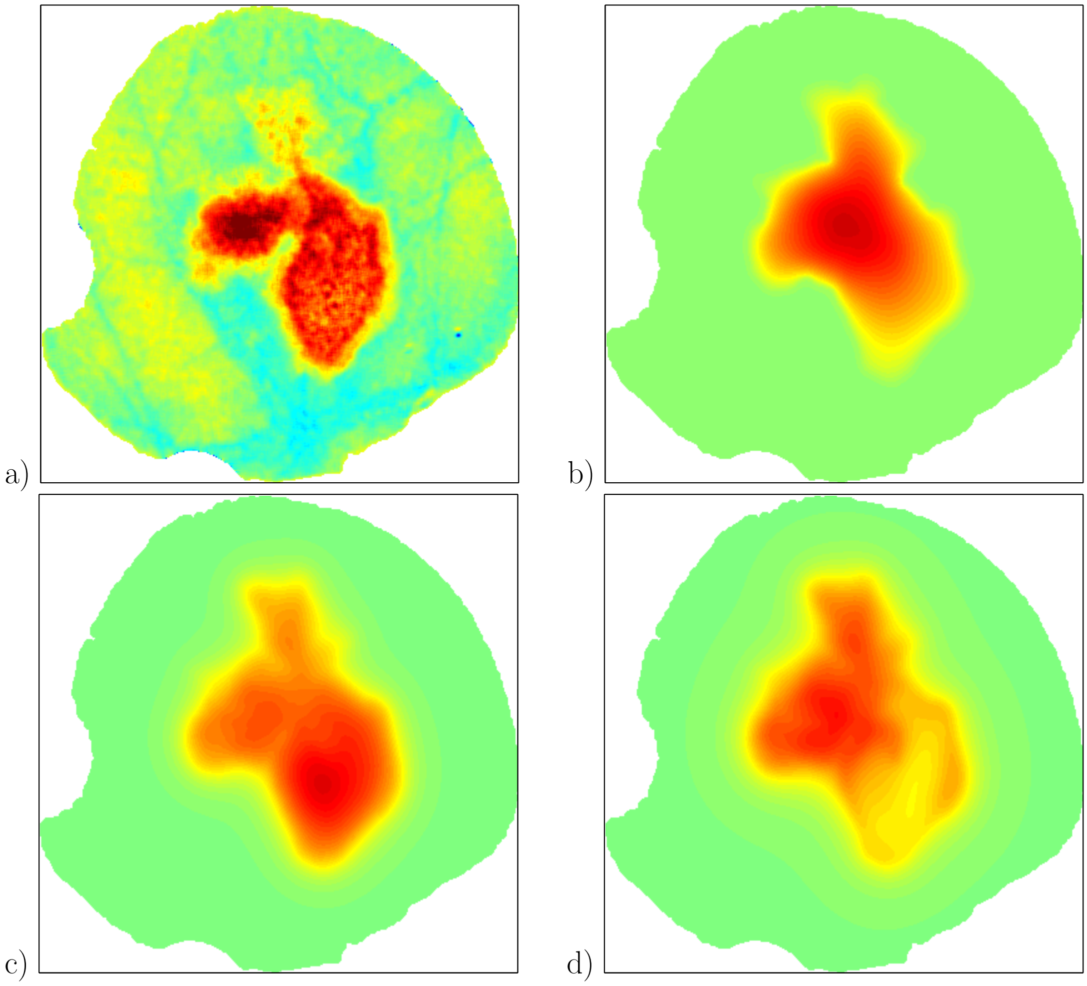

Figure 7.4: A comparison between (a) an experimental pH profile within the region of interest, and the model profiles under assumptions of (b) an avascular tumour, (c) a partially vascularised tumour and (d) a fully vascularised tumour. The best fit is given by the partially vascularised model, with an RMS difference of 7.06×10^{-2} pH units.

reproduce the spatial inhomogeneities both within and surrounding the tumour. Whilst the model assumes spatially homogeneous vasculature within the normal tissue, in reality the normal tissue contains both well perfused (blue) and poorly perfused (yellow) regions. Moreover, the model predicts acidity to be much higher in the top region of the tumour than is actually the case. Nonetheless, the best-fit RMS of 7.06×10^{-2} pH units in Fig. 7.4 (c) is excellent, when we consider that the pH resolution of the experimental image is 4.2×10^{-2} units [64]. This goodness-of-fit goes some way to validating the use of Eq. (7.3) as a model for the hydrogen ion distribution around a tumour.

In Tables 7.2 and 7.3 we present the results of the parameter estimation process for both the avascular and partially vascular cases. Over the 24 images, the fully vascular model ($\Omega_V = \Omega_R$) was never found to give the best fit, and thus cannot be considered the most appropriate model for tumour vasculature. The partially vascular model provided the best description of acidity around most of the tumours, though the avascular model was best in some cases.

From the tables we see that, for the avascular model, in 15 of the 24 images there was a RMS fit of less than 0.1 pH units. For the partially vascular model, this fit was observed in 13 of the 24 images. Given that five of the experimental images (marked with asterisks) were corrupted, displaying regions of physiologically unrealistic pH (less than pH 5 or greater than pH 8), we may conclude that the models are concurrent with the data in the vast majority of cases.

We calculate the means and standard deviations of θ_i from the estimates that produce a good fit (RMS < 0.1 pH units). At this point one problem with the parameter estimation process becomes clear. For parameter θ_1 in the avascular model, and parameter θ_3 in both models, we see a very large standard deviation relative to the mean. Even for individual tumours we see a large change in these predicted parameters over the course of the tumour's growth. This is because the landscape over which we are minimising is fairly shallow. In other words, large changes in θ_3 are compensated for by large changes in θ_1, as defined by Eq. (7.8), leading to only a small change in the RMS difference. The shallowness of the RMS landscape in response to changes in θ_3 is highlighted in Fig. 7.5.

Notwithstanding these problems with the fitting process, we look for a relationship between the cellular acid production rate θ_1 and the tumour growth rate. Assuming the tumour follows an exponential growth process, the growth rate between times t_0 and t_1 is defined as

$$\lambda = \frac{\ln A(t_1) - \ln A(t_0)}{t_1 - t_0}, \tag{7.10}$$

where $A(t)$ denotes the area of the tumour (in mm^2) at time t. The vascular model in Table 7.3 is used to investigate the relationship, as θ_1 is reasonably 'well behaved'. The results are presented in Fig. 7.6. We see that there may indeed be a relationship here between tumour acid production rates and growth rates, as has been shown previously [81]. The correlation coefficient between θ_1 and λ is $r = 0.587$; the probability of observing a correlation this large when the true correlation is zero is $p = 0.0576$. This is not quite sufficient evidence to reject the null hypothesis that there is no correlation between the two variables at the standard 0.05 level of significance. Nonetheless, given the small size of the available data set, it goes some way to confirming this relationship.

Mouse	Time (days)	θ_1	θ_2 (pH)	θ_3	RMS (pH)	Size (mm^2)
0208-r1	0	5.22×10^{4}	7.05	2.00×10^{-2}	6.86×10^{-2}	4.17
	10	6.15×10^{2}	7.03	4.45	6.86×10^{-2}	5.70
	15*	1.12×10^{4}	7.01	2.00×10^{-2}	5.77×10^{-1}	7.27
0208-r2	0	1.08×10^{5}	7.12	2.00×10^{-2}	9.29×10^{-2}	19.6
	9	7.80×10^{1}	6.91	3.03×10^{1}	1.19×10^{-1}	24.8
	12*	1.31×10^{2}	6.92	1.88×10^{1}	1.95×10^{-1}	26.6
0209-00	0	3.74×10^{1}	7.00	4.64×10^{1}	8.68×10^{-2}	9.85
	8	3.43×10^{1}	7.02	1.30×10^{2}	9.59×10^{-2}	8.84
	13	2.72	7.03	3.00×10^{3}	9.78×10^{-2}	9.14
0209-r1	0	4.56×10^{2}	6.99	4.22	7.11×10^{-2}	14.0
	8	1.83×10^{1}	7.03	8.08×10^{1}	9.99×10^{-2}	17.9
	11	7.37×10^{1}	7.12	7.48×10^{1}	9.34×10^{-2}	22.1
0406-00	0*	2.01×10^{-1}	6.96	2.01×10^{3}	2.09×10^{-1}	5.18
	6	0	6.22	–	7.67×10^{-1}	11.5
	13	2.06×10^{2}	7.02	4.55×10^{1}	1.24×10^{-1}	20.6
0407-00	0	3.44×10^{1}	7.01	5.28×10^{1}	5.99×10^{-2}	2.73
	6	3.46×10^{1}	6.94	8.11×10^{1}	6.74×10^{-2}	3.72
	13	6.59×10^{2}	7.06	3.54	5.95×10^{-2}	5.22
0407-r1	0	4.23×10^{3}	6.98	3.09×10^{-1}	7.94×10^{-2}	7.36
	6*	1.89×10^{1}	7.07	5.44×10^{1}	1.29×10^{-1}	10.7
	13*	8.03×10^{-1}	7.12	4.52×10^{1}	5.53×10^{-1}	21.9
0407-r2	0	7.86×10^{1}	7.00	4.44	7.77×10^{-2}	10.4
	6	1.64×10^{2}	6.96	7.43	9.70×10^{-2}	10.3
	13	1.36×10^{3}	6.98	2.29×10^{1}	1.12×10^{-1}	10.6
Mean		1.11×10^{4}	7.02	2.33×10^{2}		
Standard deviation		2.98×10^{4}	5.10×10^{-2}	7.67×10^{2}		

Table 7.2: Results of the avascular ($\Omega_V = \Omega_R - \Omega_M$) parameter estimation. Means and standard deviations are taken from all runs where the RMS fit < 0.1 pH units.

Mouse	Time (days)	θ_1	θ_2 (pH)	θ_3	RMS (pH)	Size (mm^2)
0208-r1	0	4.00	7.05	9.87×10^{1}	7.22×10^{-2}	4.17
	10	5.74	7.03	8.05×10^{1}	6.94×10^{-2}	5.70
	15*	4.34×10^{-1}	7.04	8.03×10^{1}	5.85×10^{-1}	7.27
0208-r2	0	1.03	7.20	3.00×10^{3}	1.46×10^{-1}	19.6
	9	6.70×10^{-1}	6.99	2.33×10^{3}	1.43×10^{-1}	24.8
	12*	1.10	6.98	1.04×10^{1}	2.04×10^{-1}	26.6
0209-00	0	2.29	7.01	1.20×10^{2}	8.81×10^{-2}	9.85
	8	5.75	7.01	7.95	9.49×10^{-2}	8.84
	13	1.81	7.03	3.00×10^{3}	9.78×10^{-2}	9.14
0209-r1	0	3.55	7.01	1.24×10^{2}	7.06×10^{-2}	14.0
	8	1.31	7.04	8.66×10^{1}	1.02×10^{-1}	17.9
	11	3.97	7.13	9.05×10^{1}	9.14×10^{-2}	22.1
0406-00	0*	1.39×10^{-1}	6.96	2.41×10^{3}	2.10×10^{-1}	5.18
	6	0	6.88	–	1.57×10^{-1}	11.5
	13	4.75	7.04	4.74	1.15×10^{-1}	20.6
0407-00	0	5.59	7.01	6.38×10^{1}	5.97×10^{-2}	2.73
	6	7.23	6.94	1.23×10^{1}	6.61×10^{-2}	3.72
	13	7.70	7.06	9.13	5.88×10^{-2}	5.22
0407-r1	0	3.93	6.98	1.28×10^{1}	7.94×10^{-2}	7.36
	6*	1.39	7.07	3.30×10^{1}	1.28×10^{-1}	10.7
	13*	0	5.34	–	1.23	21.9
0407-r2	0	8.74×10^{-1}	7.01	6.84×10^{1}	8.87×10^{-2}	10.4
	6	2.47	6.96	3.78×10^{1}	9.89×10^{-2}	10.3
	13	3.42×10^{1}	6.99	3.73×10^{1}	1.11×10^{-1}	10.6
Mean		4.22	7.02	2.87×10^{2}		
Standard deviation		2.08	4.75×10^{-2}	8.16×10^{2}		

Table 7.3: Results of the partially vascular bed ($\Omega_V = \Omega_R - \Omega_D$) parameter estimation. Means and standard deviations are taken from all runs where the RMS fit < 0.1 pH units.

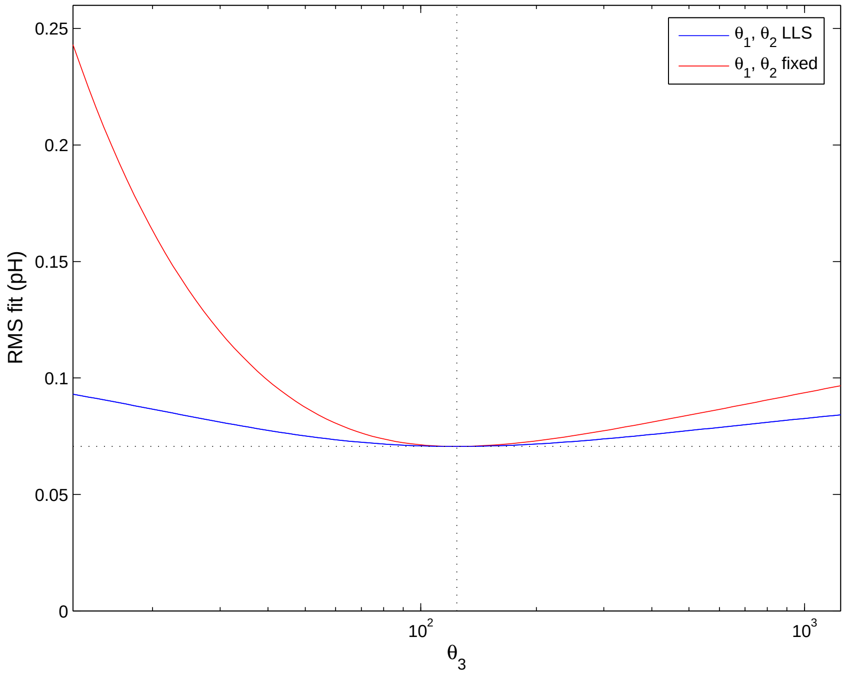

Figure 7.5: Variation in RMS fit with θ_3 for the partially vascular bed model (mouse 0209-r1, time 0 – see Table 7.3). θ_3 is varied by two orders of magnitude around its best-fit value of 1.24×10^2. Shown is linear least squares (LLS) best-fit (blue), whereby θ_1 and θ_2 respond to changes in θ_3 as per Eq. (7.8). Shown also is the fit obtained with θ_1 and θ_2 fixed (red) at the levels given in Table 7.3. The shallowness of the RMS landscape occurs because large changes in θ_3 are compensated by changes in θ_1 and θ_2, leading to a small change in RMS fit. However, even when θ_1 and θ_2 are fixed we see little change in fit as θ_3 is increased from its base value, demonstrating that the model is relatively insensitive to changes in θ_3.

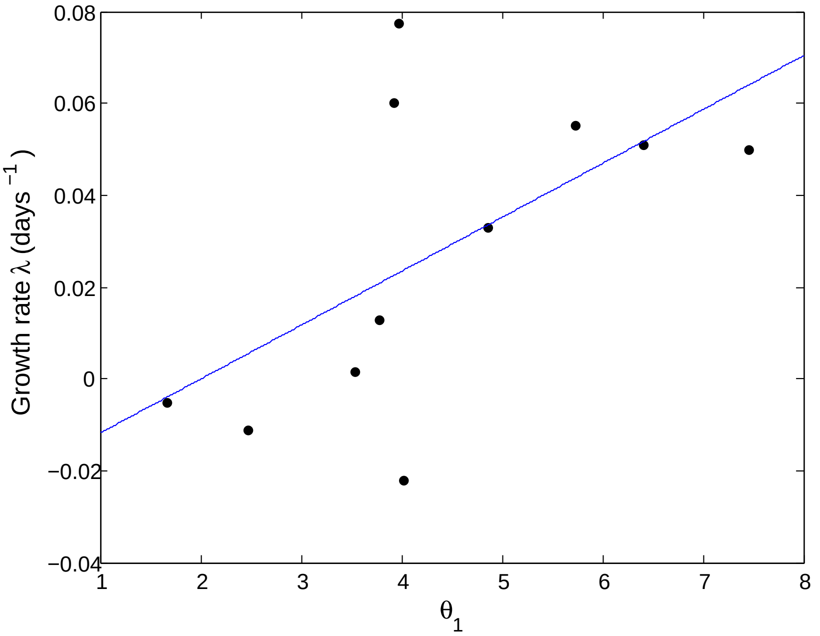

Figure 7.6: Relationship between the tumour acid production rate θ_1 and growth rate λ. Data points are taken from the model presented in Table 7.3. Also shown is the line of best fit. The correlation coefficient for the two variables is $r = 0.587$, with $p = 0.0576$.

7.5 Discussion

In this chapter, we have analysed a number of pH images obtained through fluorescence spectroscopy of tumours implanted in mice. The aims behind this chapter were twofold. Firstly, throughout this thesis, we have assumed that the hydrogen ion profile in and around a tumour evolves according to a simple reaction-diffusion equation. Comparing our model profile with the experimental image allows validation of the work we have carried out so far. Secondly, in recent years we have seen a move towards functional, rather than physical, imaging of tumours. Imaging pH with a spatial resolution comparable to that of standard MR imaging has emerged as a promising alternative to monitoring glucose uptake through FDG-PET. As imaging technology continues to advance, we see increased need for extracting key diagnostic parameters from such images.

The model equation (Eq. (7.3)) relies on three parameters. Through a suitable transformation, the parameter estimation process was reduced to minimising a function over one variable. The results from this process were very promising – in the majority of cases, the RMS distance between the experimental and model pH image was less than 0.1 pH units, which can be considered an excellent fit, given the pH resolution of the experimental images of around 0.04 pH units.

The background extracellular pH, θ_2, was found to be close to pH 7 for all of the images analysed here. This is somewhat less than the normal range of pH 7.2–7.4, but coincides with the experimentalists' belief that the installation of window chambers can cause slight tissue injury and acidification [64]. The other parameter estimates, θ_1 and θ_3, were found to have a very high standard deviation. This is an artefact of the shallowness of the RMS landscape – large changes in these parameters only lead to small changes in the RMS error. Unfortunately, this means that, as set out above, the method is unsuitable for use in a diagnostic setting, as the parameter estimates can not be considered very reliable. Nonetheless, as shown in Fig. 7.6, the estimation process goes some way to validating the relationship between tumour acid production rate and growth rate.

The primary aim of this chapter has been to provide a preliminary investigation into pH image analysis – acting as a proof-of-concept that critical biological parameters may be extracted from pH images through solution of an inverse problem. Clearly, pH images obtained in a clinical setting will not involve window chambers, and the precise methodology for parameter extraction will depend on the imaging modality used. Nonetheless, the initial results have been promising, and there is much scope for further work. The first step would be to create a sharper error landscape in order to more confidently estimate the parameters. Applying this to a larger data set than we have available here would allow verification of the correlation in Fig. 7.6, and thus could have immediate impact as a diagnostic tool. Returning to Fig. 7.4 (a), the model could be extended to incorporate a more realistic description of the vasculature surrounding the tumour, through extracting those areas of high pH. Finally, in the longer term, a greater understanding of the relationship between pH and cellular division could allow the image analysis to have predictive power – given a pH image, an experimentally-validated model could describe the state of the tumour at some point in the future, a tool that would be invaluable to the clinician.

Chapter 8

Summary and further work

8.1 Summary

Cancer is a major cause of sickness and death throughout the world. During the 1990s in the UK and Ireland, there were on average 270 000 new cases of cancer diagnosed and 165 000 deaths from cancer each year [94]. In England and Wales, cancer became the most common cause of death in females in the late 1960s, and in males in the mid-1990s [93].

In this post-genomic era, much of cancer research continues to focus on searching for the genetic abnormalities underlying cancer development. Each year a vast array of papers are published announcing the discovery of a new oncogene or tumour suppressor gene. However, we may question the validity of such an approach; at the genetic level, cancers are extremely heterogeneous, with no single set of genetic changes found in every cancer population [21]. It is likely that the common lethal phenotypic traits of cancer, such as invasion and metastasis, are not the direct result of genetic changes but rather may be mediated by other mechanisms.

One characteristic common to most tumours is an altered microenvironment. Due in part to poor vasculature, marked fluctuations may be seen in tumour metabolite concentrations, in particular displaying low oxygen and high acid levels. In this thesis, we investigate the effects this harsh microenvironment has during cancer development. In particular, we focus on understanding the evolutionary pressures leading to upregulation of aerobic glycolysis and the role this metabolic change will play during subsequent growth. Approaching this from a mathematical modelling perspective allows integration of existing experimental data and quantitative insights into the underlying processes. In this chapter, we draw together the important points of the thesis, comparing and contrasting current oncological belief with the results of our work. We also set out the key questions that remain unanswered and suggest experimental and mathematical approaches to tackling these problems.

The phenotypic traits of cancer arise early during carcinogenesis [10]. Thus, in Chapter 4, we investigate the evolutionary pressures acting during avascular, pre-malignant growth. A model for the key cell–environment interactions occurring during this phase of development was proposed by Gatenby and Gillies [45]. Their model is difficult to test experimentally, as measurement of the evolutionary pressures acting on cells is not possible. Instead, we employ a hybrid cellular automaton approach to test their hypotheses mathematically. We find, consistent with their hypotheses, that upregulation of glycolysis represents an adaptation to hypoxia that develops as tumour cells grow away from their blood supply. This new phenotype, in turn, causes environmental acidosis which promotes subsequent adaptation to prevent acid-induced cell death. The phenotype that emerges from this sequence has a substantial proliferative advantage because it creates an environment that is toxic to its competitors but not to itself.

The mathematical framework also provides some predictions beyond the previous theoretical model. We find that the key limiting factor in lesion expansion away from the surrounding basement membrane is not glucose levels. Over the length scale under consideration, a negligible drop in glucose concentration is observed; rather, necrosis of cells furthest from the basement membrane is due to acid-induced toxicity. Any therapeutic approach that blocks the function of the Na^+/H^+ antiport (such as amiloride) will inhibit the adoption of the invasive phenotype through increasing susceptibility to acid.

In Chapters 5 and 6 we move on to consider a different length scale. Using partial differential equations, we examine the role played by acidity in the growth of a mass of tumour cells displaying increased aerobic glycolysis and acid resistance. We amalgamate a previous model of tumour growth (Greenspan [51]) with a model of acid-mediated invasion (Gatenby and Gawlinski [41]). The work identifies a critical bifurcation parameter that determines the change from a benign to an invasive growth pattern. We predict that an acellular gap will separate the advancing tumour and receding normal tissue fronts, and that reducing the level of systemic acidity will reduce tumour invasiveness and slow growth. Each of these observations had been made previously in the model of Gatenby and Gawlinski. Unlike the previous model, our approach leads to a physiologically-accurate description of benign growth – exponential growth, followed by slow growth towards a equilibrium size. Moreover, we predict an unexpected and counter-intuitive therapeutic approach; we show that further increasing the acidity within a tumour beyond a critical threshold may induce auto-toxicity and cause widespread tumour regression.

Recent technological advances have led to the emergence of pH imaging as an alternative to existing techniques for functional tumour imaging. In Chapter 7 we develop a new technique for extracting key biological parameters from pH images. The work demonstrates an excellent agreement between the experimental pH profiles and the theoretical profiles derived in Chapter 5, which goes some way to justifying our previous modelling work. More importantly, we show a correlation between the estimated acid production rate and tumour growth rate, consistent with previous observations [81]. As such, this key parameter – tumour acid production rate – may be used as a quantitative diagnostic tool in a clinical setting. Validation of the technique on a larger data set, particularly one drawn from high-resolution magnetic resonance imaging, would be of considerable value.

8.2 Further work

8.2.1 Cellular metabolism

One major criticism that may be levelled at our work is that we have assumed that many processes follow simple zeroth or first order dynamics; in reality, these processes are likely governed by much more complex functional forms. In Chapters 5 and 6 we assume that acidity is the primary factor governing tumour growth; in reality growth will also be governed by oxygen and glucose concentrations, as well as levels of other critical metabolites. The advantage of our simplistic approach is two-fold. Firstly, the models remain tractable – determination of the bifurcation parameter in Chapter 5 would not have been possible with a more complex model. Secondly, the interdependence between the consumption and production of various metabolites is not known, hence use of more complex forms is not currently possible.

In the post-genomic era, we have a greatly increased understanding of the protein–protein and protein–metabolite interactions that regulate cellular glucose metabolism [69]. The metabolic pathway by which cells produce ATP from glucose involves a large number of intermediate reactions, transport processes and feedback mechanisms. Recent authors have produced a large-scale model of this pathway based on dynamic mass balances and mechanistic kinetics [8], capturing in detail each of these intermediate processes. The major problem with such an approach is that almost all of the parameter values are unknown and difficult to estimate accurately.

One technique for gaining insight into the dynamics of these complex networks involves breaking down the pathway into its constituent motifs [115]. Application to glucose metabolism will allow the key behaviours associated with each set of reactions to then be captured. Moreover, through recombination of these motifs, we will produce a full model of cellular metabolism reliant on significantly fewer parameters, verifiable through comparison with extant data (e.g. [20]).

This work would allow formulation of more accurate analogues of the models presented in this thesis. For example, normal tissue undergoes apoptosis in response to a drop in extracellular pH. Contrastingly, tumour tissue undergoes necrosis in response to a drop in *intra*cellular pH, occurring when cells can no longer maintain the gradient across the cell membrane. A model for both intracellular and extracellular pH would be a natural byproduct of this work on metabolism. The work would have further implications, providing a framework for understanding the regulation of glucose, oxygen, lactate and ATP flux through the interaction of physical and biochemical processes at the cellular, tissue/organ subsystem and whole body level. It would have a broad spectrum of applications, increasing our understanding of diseases where altered metabolism plays a key role, such as diabetes.

8.2.2 Early carcinogenesis

The cellular automaton model presented in Chapter 4 provides a novel framework for understanding the cell–cell and cell–microenvironment interactions driving evolutionary changes during early carcinogenesis. However, the model may benefit from certain adaptations. In addition to the accurate model of cellular respiration outlined above, it is possible to include necrotic debris within the model. Looking to the late stage ductal carcinoma *in situ* in Fig. 2.6, we see that the lumen (centre of the duct) is filled with cell debris. There are no macrophages within the duct, but the debris is naturally washed away with time. Within our current framework, the debris is removed from the system immediately. A lag time could be introduced through defining a stochastic removal of debris at each generation. The differing sizes of cells and necrotic debris could be accounted for by letting live cells occupy 3×3 automaton elements, say, whilst the debris would occupy a single element.

Within our model, we investigated the effects of three specific phenotypic changes: hyperplasia, glycolysis and acid-resistance. However, the same model framework could be used to investigate any phenotypic change that affects a cell's interactions with other cells or its microenvironment. The model could also be extended to incorporate any specific epithelial geometry, such as the crypts that develop into colorectal cancer.

One practical problem associated with this modelling approach can be seen in Fig. 4.5.

The stochastic nature of the system means that, in order to obtain a quantitative understanding of the role of a specific parameter in the system, a large number of simulations must be performed, and the average dynamics examined. Each of the panels in Fig. 4.5 is the result of 850 simulations, and hence requires a large amount of computational time. One method for overcoming this problem is to recast the model as a system of partial differential equations (PDEs). Returning to the Gatenby and Gawlinski model defined in Eqs.(3.6)–(3.8), we see that the system is defined as two competing populations that produce acid, respond to acid, proliferate and diffuse at different rates. Our recast model would simply be an extension of this to include eight competing populations, each responding to oxygen, glucose and hydrogen ions according to their specific phenotype. For example, only cells displaying the hyperplastic phenotype would be allowed to diffuse away from the basement membrane.

It is not clear how valid PDEs are at describing early carcinogenesis. Given the size of the system, it is important to consider the effects of individual cells. Moreover, adaptation between phenotypes happens at the individual cell level, not continuously throughout the whole population. Nonetheless, from a mathematical perspective, it would be interesting to compare the two approaches. Moreover, use of PDEs would allow insight into the roles of individual parameters on system dynamics without the necessity of running multiple simulations outlined above.

8.2.3 Experimental work

The modelling work within this thesis provides answers for some key questions – why tumours display aerobic glycolysis and what effect aerobic glycolysis has on tumour growth.

Experimental verification of some of the modelling predictions would be of interest:

- During early carcinogenesis, glucose supply is not limited (Chapter 4)
- During early carcinogenesis, cellular adaptation rates increase until cells reach the peak of the fitness landscape (Chapter 4)
- Cellular quiescence induces cycles of hypoxia and acidity (Chapter 6)

However, I feel the most important results of this thesis are the predicted therapeutic strategies, directed towards increasing tumour cells' susceptibility to acidity. Of considerable interest would be testing these predictions *in vitro* in multicellular spheroid models. Initial experimental work suggests that brief systemic acidosis may induce widespread tumour apoptosis and regression [65]. Subjecting spheroids to acidosis, combined with use of amiloride, could prove to be an even more effective therapeutic regime. Taking advantage of altered cellular metabolism may prove to be a new weapon in the ongoing battle against cancer.

Appendix A

Glossary

adenoma Benign epithelial tumour in which the cells form recognisable glandular structures.

angiogenesis The formation of new capillary blood vessels.

anthracycline Type of chemotherapy that acts to prevent cell division by disrupting the structure of the DNA.

apoptosis Programmed cell death, as signalled by the nuclei in normally functioning cells.

basement membrane Extracellular matrix characteristically found under epithelial cells. There are two distinct layers: the basal lamina, immediately adjacent to the cells, and the reticular lamina.

benign Not malignant. Benign tumours do not invade or metastasise, having lost growth control but not positional control. They are usually surrounded by a fibrous capsule of compressed tissue, and treatment or removal is curative.

carcinogen Chemical, virus or radiation that can induce cancer.

carcinoma Malignant epithelial tumour.

clastogenic Altering the structure of chromosomes.

differentiation Process undergone by cells as they mature into normal cells. Differentiated cells have distinctive characteristics, perform specific functions and are less likely to divide.

epigenetic Differentiation due to selective gene activation and expression. Not due to changes in the genome.

epithelium Covering of internal and external surfaces of the body, including the lining of vessels and other small cavities. It consists of cells joined by small amounts of 'cementing' substances. Epithelium is classified into types on the basis of its depth (in terms of cell number) and the shape of the superficial cells.

extracellular matrix (ECM) Any material produced by cells and secreted into the surrounding medium, usually applied to the noncellular portion of tissues. Although produced by cells, the ECM can influence the behaviour of cells quite markedly, an important factor to consider when growing cells *in vitro*.

heritable Capable of being transmitted from parent to child.

hyperplasia Abnormal increase in the number of normal cells in a tissue.

hypoxia Diminished oxygen supply.

in situ Localised. A carcinoma that has not breached the basement membrane.

invasion Movement of cells into adjacent tissue normally occupied by a different cell type.

in vitro Cell manipulation outside the body.

in vivo In the living body. An experimental procedure using an intact live animal.

malignant Tending to become progressively worse and to result in death. Malignant tumours are invasive and have the capacity to metastasise. Compare benign

metastasis Transfer of cells from one organ or part to another, not directly connected with it. This usually occurs through the blood vessels, lymph channels or spinal fluid.

oncogene Overexpressed version of a normal gene (the *proto-oncogene*) that promotes excessive growth. Compare *tumour suppressor gene.*

necrosis Cell death.

quiescence The state of not dividing.

somatic Characteristic of the body.

stroma (syn: **interstitium**) Connective tissue framework of an organ, gland or other structure, in contrast to the functional cells. Rich in extracellular matrix.

tumour (syn: **neoplasm**) Abnormal mass of tissue serving no useful function to the host, resulting from excessive cell division that is uncontrolled and progressive. May be either benign or malignant.

tumour suppressor gene (TSG) (syn: **anti-oncogene**) A gene negatively regulating cell division that, when inactivated (through mutation for example), allows escape from normal growth constraints. Compare *oncogene.*

References

[1] JA Adam. *A Survey of Models for Tumor-Immune System Dynamics*. Birkhäuser, 1997.

[2] T Alarcón, HM Byrne, and PK Maini. A cellular automaton model for tumour growth in inhomogeneous environment. *J. Theor. Biol.*, 225:257–274, 2003.

[3] B Alberts, A Johnson, J Lewis, M Raff, K Roberts, and P Walter. *Molecular Biology of the Cell*. Garland Science, 4th edition, 2002.

[4] MR Alison. Cancer. In *Encyclopedia of Life Sciences*. Nature Publishing Group, 2001. http://www.els.net.

[5] ARA Anderson. A hybrid mathematical model of solid tumour invasion: the importance of cell adhesion. *Math. Med. Biol.*, 22:163–186, 2005.

[6] ARA Anderson and MAJ Chaplain. Continuous and discrete mathematical models of tumor-induced angiogenesis. *Bull. Math. Biol.*, 60:857–899, 1998.

[7] RP Araujo and DLS McElwain. A history of the study of solid tumour growth: the contribution of mathematical modelling. *Bull. Math. Biol.*, 66:1039–1091, 2004.

[8] M Banaji, I Tachtsidis, D Delpy, and S Baigent. A physiological model of cerebral blood flow control. *Math. Biosci.*, 194:125–173, 2005.

[9] C Baudelet, R Ansiaux, BF Jordan, X Havaux, B Macq, and B Gallez. Physiological noise in murine solid tumours using $T2^\star$–weighted gradient-echo imaging: a marker of tumour acute hypoxia? *Phys. Med. Biol.*, 49:3389–3411, 2004.

[10] R Bernards and RA Weinberg. A progression puzzle. *Nature*, 418:823, 2002.

[11] B Beutler and A Cerami. Cachectin and tumor necrosis factor as two sides of the same biological coin. *Nature*, 320:584–588, 1986.

[12] CR Boland and A Goel. Somatic evolution of cancer cells. *Semin. Cancer Biol.*, 15:436–450, 2005.

[13] RD Braun, JL Lanzen, and MW Dewhirst. Fourier analysis of fluctuations of oxygen tension and blood flow in R3230Ac tumors and muscle in rats. *Am. J. Physiol.*, 277:H551–H568, 1999.

[14] AC Burton. Rate of growth of solid tumours as a problem of diffusion. *Growth*, 30:157–76, 1966.

[15] HM Byrne. A weakly nonlinear analysis of a model of avascular solid tumour growth. *J. Math. Biol.*, 39:59–89, 1999.

[16] HM Byrne and MAJ Chaplain. Free boundary value problems associated with the growth and development of multicellular spheroids. *Eur. J. Appl. Math.*, 8:639–658, 1997.

[17] J Cairns. *Cancer, Science and Society.* Freeman, 1978.

[18] KC Calman. Cachexia. In *Oxford Textbook of Pathology*, volume 1, pages 715–717. Oxford University Press, 1992.

[19] JJ Casciari, SV Sotirchos, and RM Sutherland. Mathematical modelling of microenvironment and growth in EMT6/Ro multicellular tumour spheroids. *Cell Prolif.*, 25:1–22, 1992.

[20] JJ Casciari, SV Sotirchos, and RM Sutherland. Variations in tumor cell growth rates and metabolism with oxygen concentration, glucose concentration, and extracellular pH. *J. Cell. Physiol.*, 151:386–94, 1992.

[21] KW Chang, S Laconi, KA Mangold, S Hubchak, and DG Scarpelli. Multiple genetic alterations in hamster pancreatic ductal adenocarcinomas. *Cancer Res.*, 55:2560–2568, 1995.

[22] RM Corless, GH Gonnet, DEG Hare, DJ Jeffrey, and DE Knuth. On the Lambert W function. *Adv. Comp. Math.*, 5:329–359, 1996.

[23] HG Crabtree. A metabolic effect typical of tumour tissue: inhibition of cellular respiration by high concentration of glucose. *Biochem. J.*, 23:536–545, 1929.

[24] SS Cross, JP Bury, PB Silcocks, TJ Stephenson, and DWK Cotton. Fractal geometic analysis of colorectal polyps. *J. Pathol.*, 172:317–323, 1994.

[25] S Crotty, CE Cameron, and R Audino. RNA virus error catastrophe: direct molecular test by using ribavirin. *Proc. Natl. Acad. Sci. USA*, 98:6895–6900, 2001.

[26] J Czernin and ME Phelps. Positron emission tomography scanning: current and future applications. *Annu. Rev. Med.*, 53:89–112, 2002.

[27] KM Dameron, OV Volpert, MA Tainsky, and N Bouck. Control of angiogenesis in fibroblasts by p53 regulation of thrombospondin-1. *Science*, 265:1582–1584, 1994.

[28] MW Dewhirst, H Kimura, SW Rehmus, RD Braun, D Papahadjopoulos, K Hong, and TW Secomb. Microvascular studies on the origins of perfusion-limited hypoxia. *Br. J. Cancer Suppl.*, 27:S247–S251, 1996.

[29] MW Dewhirst, TW Secomb, ET Ong, R Hsu, and JF Gross. Determination of local oxygen consumption rates in tumors. *Cancer Res.*, 54:3333–3336, 1994.

[30] G Di Chiro, J Hatazawa, DA Katz, HV Rizzoli, and DJ De Michele. Glucose utilization by intracranial meningiomas as an index of tumor aggressivity and probability of recurrence: a PET study. *Radiology*, 164:521–6, 1987.

[31] M Eigen. Self-organization of matter and the evolution of biological macromolecules. *Naturwissenschaften*, 58:465–523, 1971.

[32] N Fausto and EM Webber. Control of liver growth. *Crit. Rev. Eukaryot. Gene Expr.*, 3:316–373, 1993.

[33] ER Fearon and B Vogelstein. A genetic model for colorectal tumorigenesis. *Cell*, 61:759–767, 1990.

[34] IJ Fidler and IR Hart. Biological diversity in metastatic neoplasms: origins and implications. *Science*, 217:998–1003, 1982.

[35] J Folkman. The role of angiogenesis in tumor growth. *Semin. Cancer Biol.*, 3:65–71, 1992.

[36] GE Forsythe, MA Malcolm, and CB Moler. *Computer Methods for Mathematical Computations*. Prentice-Hall, 1976.

[37] SJ Franks, HM Byrne, JC Underwood, and CE Lewis. Biological inferences from a mathematical model of comedo ductal carcinoma *in situ* of the breast. *J. Theor. Biol.*, 232:523–543, 2005.

[38] SS Gambhir. Molecular imaging of cancer with positron emission tomography. *Nature Rev. Cancer*, 2:683–693, 2002.

[39] RA Gatenby. Models of tumor-host interaction as competing populations: implications for tumour biology and treatment. *J. Theor. Biol.*, 176:447–455, 1995.

[40] RA Gatenby. Application of competition theory to tumour growth: implications for tumour biology and treatment. *Eur. J. Cancer*, 32A:722–726, 1996.

[41] RA Gatenby and ET Gawlinski. A reaction-diffusion model of cancer invasion. *Cancer Res.*, 56:5745–53, 1996.

[42] RA Gatenby and ET Gawlinski. The glycolytic phenotype in carcinogenesis and tumor invasion: insights through mathematical models. *Cancer Res.*, 63:3847–54, 2003.

[43] RA Gatenby, ET Gawlinski, AF Gmitro, B Kaylor, and RJ Gillies. Acid-mediated tumor invasion: a multidisciplinary study. *Cancer Res.*, 66:5216–5223, 2006.

[44] RA Gatenby, ET Gawlinski, C Tangen, and RC Flanigan. The possible role of post operative azotemia in enhanced survival of patients with metastatic renal cancer following cytoreductive nephrectomy. *Cancer Res.*, 62:5218–5222, 2002.

[45] RA Gatenby and RJ Gillies. Why do cancers have high aerobic glycolysis? *Nature Rev. Cancer*, 4:891–899, 2004.

[46] RA Gatenby and PK Maini. Mathematical oncology: cancer summed up. *Nature*, 421:321, 2003.

[47] A Gilead and M Neeman. Dynamic remodeling of the vascular bed precedes tumor growth: MLS ovarian carcinoma spheroids implanted in nude mice. *Neoplasia*, 1:226–230, 1999.

[48] RJ Gillies, N Raghunand, ML Garcia-Martin, and RA Gatenby. pH imaging. *IEEE Eng. Med. Biol.*, 23:57–64, 2004.

[49] RJ Gillies, N Raghunand, GS Karczmar, and ZM Bhujwalla. MRI of the tumor microenvironment. *J. Magn. Reson. Imaging*, 16:430–450, 2002.

[50] BS Govindan, WB Spillman, Jr., JL Robertson, and WR Huckle. Acid-mediated tumor invasion: how does vasculature affect the growth characteristics? http://arXiv.org/q-bio/0401003.

[51] HP Greenspan. Models for the growth of a solid tumor by diffusion. *Stud. Appl. Math.*, 51:317–340, 1972.

[52] HP Greenspan. On the self-inhibited growth of cell-cultures. *Growth*, 38:81–95, 1974.

[53] HP Greenspan. On the growth and stability of cell cultures and solid tumors. *J. Theor. Biol.*, 56:229–242, 1976.

[54] K Groebe, S Erz, and W Mueller-Kleiser. Glucose diffusion coefficients determined from concentration profiles in EMT6 tumor spheroids incubated in radioactively labeled L-glucose. *Adv. Exp. Med. Biol.*, 361:619–625, 1994.

[55] D Hanahan and RA Weinberg. The hallmarks of cancer. *Cell*, 100:57–70, 2000.

[56] G Helmlinger, F Yuan, M Delian, and RK Jain. Interstitial pH and pO_2 gradients in solid tumors *in vivo*: high-resolution measurements reveal a lack of correlation. *Nature Med.*, 3:177–182, 1997.

[57] AV Hill. The diffusion of oxygen and lactic acid through tissues. *R. Soc. Proc. B*, 104:39–96, 1928.

[58] RP Hill, K De Jaeger, A Jang, and R Cairns. pH, hypoxia and metastasis. *Novart. Fnd. Symp.*, 240:154–165, 2001.

[59] AL Hodgkin and AF Huxley. A quantitative description of membrane current and its application to conduction and excitation in nerve. *J. Physiol.*, 117:500–544, 1952.

[60] MS Jafri, SJ Dudycha, and B O'Rourke. Cardiac energy metabolism: models of cellular respiration. *Annu. Rev. Biomed. Eng.*, 3:57–81, 2001.

[61] RK Jain. Delivery of molecular and cellular medicine to solid tumors. *Adv. Drug Delivery Rev.*, 46:149–168, 2001.

[62] M Johnsen, LR Lund, J Romer, K Almholt, and K Dano. Cancer invasion and tissue remodelling: common themes in proteolytic matrix degredation. *Curr. Opin. Cell Biol.*, 10:667–671, 1998.

[63] F Kallinowski, P Vaupel, S Runkel, G Berg, HP Fortmeyer, KH Baessler, and K Wagner. Glucose uptake, lactate release, ketone body turnover, metabolic milieu and pH distributions in human cancer xenograpts in nude rats. *Cancer Res.*, 48:7264–7272, 1988.

[64] BM Kaylor. *In vivo* measurement of pH in tumor and surrounding tissue using fluorescence ratio imaging. Master's thesis, University of Arizona, 2004.

[65] ST Kelley, C Manon, DG Buerk, TW Bauer, and DL Fraker. Acidosis plus melphalan induces nitric oxide-mediated tumor regression in an isolated limb perfusion human melanoma xenograft model. *Surgery*, 132:252–258, 2002.

[66] F Kerangueven, T Noguchi, RF Coulie, F Allione, V Wargniez, J Simony-Lafontaine, M Longy, J Jacquemier, H Sobol, F Eisinger, and D Birnbaum. Genome-wide search for loss of heterozygosity shows extensive genetic diversity of human breast carcinomas. *Cancer Res.*, 57:5469–5474, 1997.

[67] MF Kiani, AR Pries, LL Hsu, IH Sarelius, and GR Cokelet. Fluctuations in microvascular blood flow parameters caused by hemodynamic mechanisms. *Am. J. Physiol.*, 266:H1822–H1828, 1994.

[68] H Kimura, RD Braun, ET Ong, R Hsu, TW Secomb, D Papahadjopoulos, K Hong, and MW Dewhirst. Fluctuations in red cell flux in tumor microvessels can lead to transient hypoxia and reoxygenation in tumor parenchyma. *Cancer Res.*, 56:5522–5528, 1996.

[69] H Kitano, K Oda, T Kimura, Y Matsuoka, M Csete, J Doyle, and M Muramatsu. Metabolic syndrome and robustness tradeoffs. *Diabetes*, 53:S6–S15, 2004.

[70] NL Komarova. Mathematical modeling of tumorigenesis: mission possible. *Curr. Opin. Oncol.*, 17:39–43, 2005.

[71] B Korzeniewski. Theoretical studies on the regulation of oxidative phosphorylation in intact tissues. *Biochim. Biophys. Acta*, 1504:31–45, 2001.

[72] A Krogh. The number and distribution of capillaries in muscles with calculations of the oxygen pressure head necessary for supplying the tissue. *J. Physiol.*, 52:409–415, 1919.

[73] M Kunkel, TE Reichert, P Benz, H Lehr, J Jeong, S Wieand, P Bartenstein, W Wagner, and T Whiteside. Overexpression of Glut-1 and increased glucose metabolism in tumors are associated with a poor prognosis in patients with oral squamous cell carcinoma. *Cancer*, 97:1015–1024, 2003.

[74] AK Laird. Dynamics of tumour growth. *Br. J. Cancer*, 18:490–502, 1964.

[75] AD Lander. A calculus of purpose. *PLoS Biology*, 2:712–714, 2004.

[76] Y Lazebnik. Can a biologist fix a radio? – Or, what i learned while studying apoptosis. *Cancer Cell*, 2:179–182, 2002.

[77] CKN Li. The glucose distribution in 9L rat brain multicell tumor spheroids and its effect on cell necrosis. *Cancer*, 50:2066, 1982.

[78] MC Mackey and M Santillán. Mathematics, biology, and physics: interactions and interdependence. *Notices Amer. Math. Soc.*, 52:832–840, 2005.

[79] NV Mantzaris, S Webb, and HG Othmer. Mathematical modeling of tumor-induced angiogenesis. *J. Math. Biol.*, 49:111–187, 2004.

[80] GR Martin and RK Jain. Noninvasive measurement of interstitial pH profiles in normal and neoplastic tissue using fluorescence ratio imaging microscopy. *Cancer Res.*, 54:5670–4, 1994.

[81] R Martinez-Zaguilan, EA Seftor, RE Seftor, YW Chu, RJ Gillies, and MJ Hendrix. Acidic pH enhances the invasive behavior of human melanoma cells. *Clin. Exp. Metastasis*, 14:176–86, 1996.

[82] DLS McElwain and LE Morris. Apoptosis as a volume loss mechanism in mathematical models of solid tumor growth. *Math. Biosci.*, 39:147–157, 1978.

[83] DLS McElwain and PJ Ponzo. A model for the growth of a solid tumor with non-uniform oxygen consumption. *Math. Biosci.*, 35:267–279, 1977.

[84] RG McKinnell, RE Parchment, AO Perantoti, and GB Pierce. *The Biological Basis of Cancer.* Cambridge University Press, 1998.

[85] MM Melicow. The three-steps to cancer: a new concept of carcinogenesis. *J. Theor. Biol.*, 94:471–511, 1982.

[86] SG Mikhlin and KL Smolitsky. *Approximate Methods for the Solution of Differential and Integral Equations.* Elsevier, 1967.

[87] M Morange. History of cancer research. In *Encyclopedia of Life Sciences.* Macmillan Publishers Ltd., 2002. http://www.els.net.

[88] T Morita, T Nagaki, I Fukuda, and K Okumura. Clastogenicity of low pH to various cultured mammalian cells. *Mutat. Res.*, 268:297–305, 1992.

[89] JD Murray. *Mathematical Biology I. An Introduction.* Springer-Verlag, 3rd edition, 2002.

[90] MG Nichols and TH Foster. Oxygen diffusion and reaction kinetics in the photodynamic therapy of multicell tumour spheroids. *Phys. Med. Biol.*, 39:2161–2181, 1994.

[91] S Patan, S Tanda, S Roberge, RC Jones, RK Jain RK, and LL Munn. Vascular morphogenesis and remodeling in a human tumor xenograft: blood vessel formation and growth after ovariectomy and tumor implantation. *Circ. Res.*, 89:732–739, 2001.

[92] AA Patel, ET Gawlinski, SK Lemieux, and RA Gatenby. A cellular automaton model of early tumor growth and invasion. *J. Theor. Biol.*, 213:315–31, 2001.

[93] MJ Quinn, PJ Babb, A Brock, L Kirby, and J Jones, editors. *Cancer Trends in England and Wales 1950-1999. Studies on Medical and Population Subjects No. 66.* The Stationary Office, 2001.

[94] MJ Quinn, H Wood, N Cooper, and S Rowan, editors. *Cancer Atlas of the United Kingdom and Ireland 1991-2000. Studies on Medical and Population Subjects No. 68.* The Stationary Office, 2005.

[95] E Racker. History of the Pasteur effect and its pathobiology. *Mol. Cell. Biochem.*, 5:17–23, 1974.

[96] N Raghunand, RA Gatenby, and RJ Gillies. Microenvironmental and cellular consequences of altered blood flow in tumours. *Br. J. Radiol.*, 76:S11–S22, 2003.

[97] N Raghunand, C Howison, AD Sherry, S Zhang, and RJ Gillies. Renal and systemic pH imaging by contrast-enhanced MRI. *Magn. Reson. Med.*, 49:249–257, 2003.

[98] N Raghunand, B Mahoney, R van Sluis, B Baggett, and RJ Gillies. Acute metabolic alkalosis enhances response of C3H mouse mammary tumors to the weak base mitoxantrone. *Neoplasia*, 3:227–35, 2001.

[99] A Ramanathan, C Wang, and SL Schreiber. Perturbational profiling of a cell-line model of tumorigenesis by using metabolic measurements. *Proc. Natl. Acad. Sci. USA*, 102:5992–5997, 2005.

[100] S Ramanujan, GC Koenig, TP Padera, BR Stoll, and RK Jain. Local imbalance of proangiogenic and antiangiogenic factors: a potential mechanism of focal necrosis and dormancy in tumors. *Cancer Res.*, 60:1442–1448, 2000.

[101] MJ Renan. How many mutations are required for tumorigenesis? Implications from human cancer data. *Mol. Carcinogen.*, 7:139–146, 1993.

[102] J Rohzin, M Sameni, G Ziegler, and BF Sloane. Pericellular pH affects distribution and secretion of cathepsin B in malignant cells. *Cancer Res.*, 54:6517–6525, 1994.

[103] T Roose, SJ Chapman, and PK Maini. Mathematical models of avascular tumour growth. a review. *SIAM Rev.* In press.

[104] PA Schornack and RJ Gillies. Contributions of cell metabolism and H^+ diffusion to the acidic pH of tumors. *Neoplasia*, 5:135–145, 2003.

[105] P Schuster. How do RNA molecules and viruses explore their worlds? In *Complexity: metaphors, models and reality*, pages 383–418. Addison- Wesley, 1994.

[106] LF Shampine and S Thompson. Solving DDEs in MATLAB. *Appl. Numer. Math.*, 37:441–458, 2001.

[107] K Smallbone, DJ Gavaghan, RA Gatenby, and PK Maini. The role of acidity in solid tumour growth and invasion. *J. Theor. Biol.*, 235:476–484, 2005.

[108] KSM Smalley, PA Brafford, and M Herlyn. Selective evolutionary pressure from the tissue microenvironment drives tumor progression. *Semin. Cancer Biol.*, 15:451–459, 2005.

[109] P Sonveaux, C Dessy, P Martinive, X Havaux, BF Jordan, B Gallez, V Gregoire, JL Balligand, and O Feron. Endothelin-1 is a critical mediator of myogenic tone in tumor arterioles: implications for cancer treatment. *Cancer Res.*, 64:3209–3214, 2004.

[110] MB Sporn. The war on cancer. *Lancet*, 347:1377–1381, 1996.

[111] RM Sutherland. Cell and environment interactions in tumor microregions: the multicell spheroid model. *Science*, 240:177–184, 1988.

[112] RM Sutherland, JA McCredie, and WR Inch. Growth of multicell spheroids in tissue culture as a model of nodular carcinomas. *J. Natl. Cancer Inst.*, 46:113–120, 1971.

[113] RH Thomlinson and LH Gray. The histological structure of some human lung cancers and the possible implications for radiotherapy. *Br. J. Cancer*, 9:539–549, 1955.

[114] AM Turing. The chemical basis of morphogenesis. *Phil. Trans. R. Soc. Lond. B*, 237:37–72, 1952.

[115] JJ Tyson, KC Chen, and B Novak. Sniffers, buzzers, toggles and blinkers: dynamics of regulatory and signaling pathways in the cell. *Curr. Opin. Cell Biol.*, 15:221–231, 2003.

[116] IMM van Leeuwen, HM Byrne, OE Jensen, and JR King. Crypt dynamics and colorectal cancer: advances in mathematical modelling. *Cell Prolif.*, 39:157–181, 2006.

[117] P Vaupel, F Kallinowski, and P Okunieff. Blood flow, oxygen and nutrient supply, and metabolic microenvironment of human tumors: a review. *Cancer Res.*, 49:6449–65, 1989.

[118] T Volk, E Jahde, HP Fortmeyer, KH Glusenkamp, and MF Rajewsky. pH in human tumour xenografts: effect of intravenous administration of glucose. *Br. J. Cancer*, 68:492–500, 1993.

[119] O Warburg. *The Metabolism of Tumours.* Constable Press, London, 1930.

[120] O Warburg. On the origin of cancer cells. *Science*, 123:309–314, 1956.

[121] JP Ward and JR King. Mathematical modelling of avascular tumour growth. *IMA J. Math. Appl. Med. Biol.*, 14:36–69, 1997.

[122] SD Webb, JA Sherratt, and RG Fish. Alterations in proteolytic activity at low pH and its association with invasion: a theoretical model. *Clin. Exp. Metastasis*, 17:397–407, 1999.

[123] SD Webb, JA Sherratt, and RG Fish. Mathematical modelling of tumour acidity: regulation of intracellular pH. *J. Theor. Biol.*, 196:237–250, 1999.

[124] S Weinhouse, O Warburg, D Burk, and AL Schade. On respiratory impairment in cancer cells. *Science*, 124:267–272, 1956.

[125] Z Werb. ECM and cell surface proteolysis: regulating cellular ecology. *Cell*, 91:439–442, 1997.

[126] S Wolfram. *Theory and Application of Cellular Automata.* World Scientfic, 1986.

[127] CC Wykoff, N Beasley, PH Watson, L Campo, SK Chia, R English, J Pastorek, WS Sly, P Ratcliffe, and AL Harris. Expression of the hypoxia-inducible and tumor-associated carbonic anhydrases in ductal carcinoma *in situ* of the breast. *Am. J. Pathol.*, 158:1011–1019, 2001.